Organic Thin-Film Electronics of Thiocirculene and Porphyrazine with Ionic Liquids

（イオン液体を用いた環状チオフェン及びポルフィラジンの有機薄膜エレクトロニクス）

Takuya Fujimoto

藤本　卓也

Department of Chemistry,

Graduate School of Science

Nagoya University

2012

Table of Contents

Chapter 3

Chapter 4

Chapter 5

Appendix

Nomenclature

AFM	Atomic Force Microscopy
CV	Cyclic Voltammetry
EDL	Electric Double Layer
FET	Field-Effect Transistor
ITO	Indium Tin Oxide
OFET	Organic Field Effect Transistor
OTFT	Organic Thin Film Transistor
SEM	Scanning Electron Microscopy
TCNQ	7,7,8,8-Tetracyanoquinodimethane
TFT	Thin Film Transistor
TTF	1,4,5,8-Tetrathiafulvalene
XRD	X-ray Diffraction

Abbreviations

1: Octathio[8]circulene (sulflower)

1,12:3,4:6,7:9,10-tetraepithiocycloocta[1,2-c:3,4-c′:5,6-c″:7,8-c‴]tetrathiophene

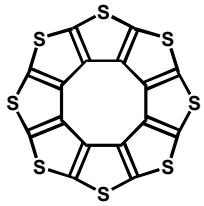

2: Tetrathiophene

cycloocta[1,2-c:3,4-c′:5,6-c″:7,8-c‴]tetrathiophene

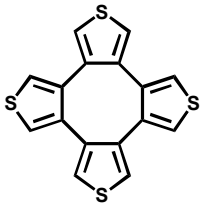

3: H_2Pc

metal-free phthalocyanine

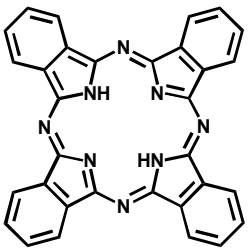

4: H_2TTDPz

metal-free tetrakis(thiadiazole)porphyrazine

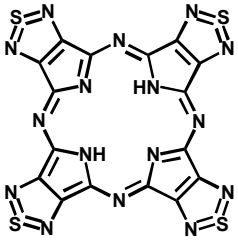

5: VOPc

vanadyl phthalocyanine

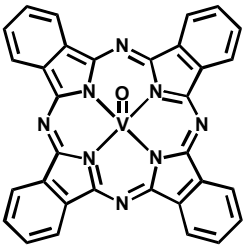

6: VOTTDPz

vanadyl tetrakis(thiadiazole)porphyrazine

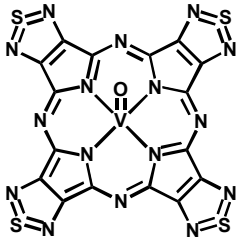

7: PbPc

lead phthalocyanine

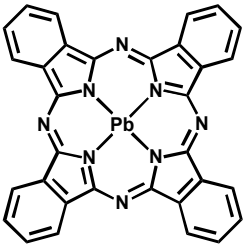

8: TiOPc

titanyl phthalocyanine

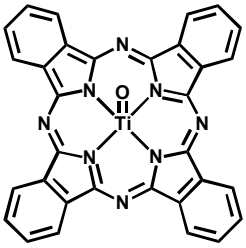

IL1: DEME-TFSI

N,*N*-diethyl-*N*-methyl(2-methoxyethyl)ammonium bis(trifluoromethylsulfonyl)imide

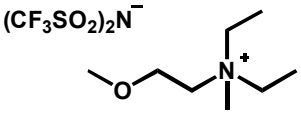

IL2: DEME-BF_4

N,*N*-diethyl-*N*-methyl(2-methoxyethyl)ammonium tetrafluoroborate

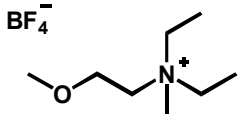

IL3: BMIM-TFSI

1-butyl-3-methylimidozolium bis(trifluoromethylsulfonyl)imide

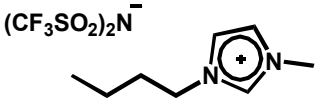

IL4: BMIM-BF_4

1-butyl-3-methylimidozolium tetrafluoroborate

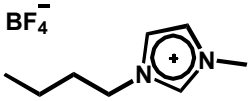

IL5: BMIM-OTf

1-butyl-3-methylimidozolium trifluoromethane sulfonate

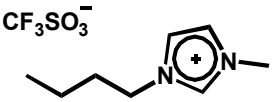

IL6: BMIM-PF_6

1-butyl-3-methylimidozolium hexafluorophosphate

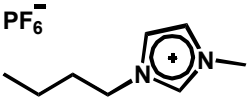

IL7: EMIM-BF_4

1-ethyl-3-methylimidazolium tetrafluoroborate

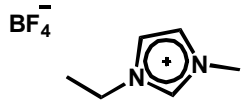

IL8: TMPA-TFSI

N,*N*,*N*-trimethyl-*N*-propylammonium bis(trifluoromethylsulfonyl)imide

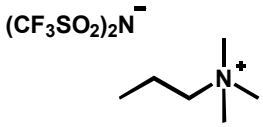

IL9: PP13-TFSI

N-methyl-*N*-propylpiperidinium bis(trifluoromethylsulfonyl)imide

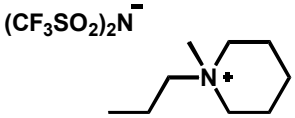

IL10: P13-TFSI

N-methyl-*N*-propylpyrrolidinium bis(trifluoromethylsulfonyl)imide

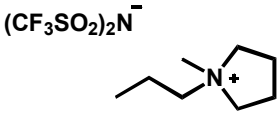

Chapter 1
General Introduction

1-1. Organic Semiconductors

Studies on organic semiconductors have been widely expanded after the report that a charge transfer complex of perylene and bromine exhibited high conductivity.[1] In 1973, TTF-TCNQ was reported as the first metallic charge transfer complex.[2] TTF-TCNQ was shown to be a one-dimensional conductor with a strong anisotropy, its conductivity changing by two or three orders of magnitude along and perpendicular to the 1D direction.[3] After this discovery, various organic materials such as charge transfer complexes formed by interactions between acceptors and donors, and cation and anion radical salts, were reported.[4–6] As these studies showed, in order to realize the high electrical conductivity of these materials, it is necessary to establish a mixed valence state in which the state of donor and/or acceptor which is partially ionized. From the point of view of conserving energy, it is more advantageous for electrons to move in mixed valence states.

The TTF-TCNQ complex converts into an insulator below 55 K by Peierls transition.[7,8] This transition is a phenomenon peculiar to the one-dimensional electronic structure, and it is important to suppress this transition in order to maintain metallic conductivity. Therefore, various molecular designs to strengthen intermolecular interactions and to improve dimensionality have been proposed. After intensive material research, TMTSF (tetramethyltetraselenafulvalene) and BEDT-TTF

(bis(ethylenedithio)tetrathiafulvalene) salts were found to exhibit superconductivity.[9,10] Since chalcogen atoms (S, Se, Te, etc.) can improve electrical conductivity by enhancing intermolecular interactions and dimensionality, they have been playing an important role in the research into organic conductors and organic superconductors.

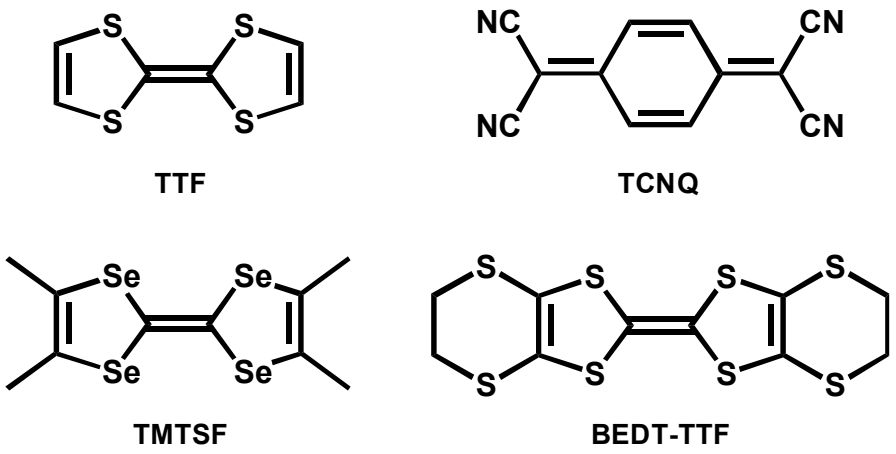

Figure 1-1. Molecular structures of TTF, TCNQ, TMTSF and BEDT-TTF.

Among them, sulfur-containing organic materials have been studied extensively in organic/molecular electronics. A variety of poly- and oligothiophenes[11–23] were synthesized by organic synthesis and electrochemistry, and their electronic properties were elucidated. In these materials, intermolecular S···S contacts play a crucial role in forming multi-dimensional electronic structures that are advantageous for electrical conduction. Cyclic oligothiophenes and thiocirculenes possess promising molecular structures from this perspective; the sulfur atoms are exposed to the outside of the molecular rings, so that intermolecular S···S contacts would naturally be expected in

their crystals. In addition, some of them are of considerable interest because they involve the radialene framework, which has been a theoretical and experimental matter of concern with regard to exocyclic double bonds, aromaticity, and π-conjugation.

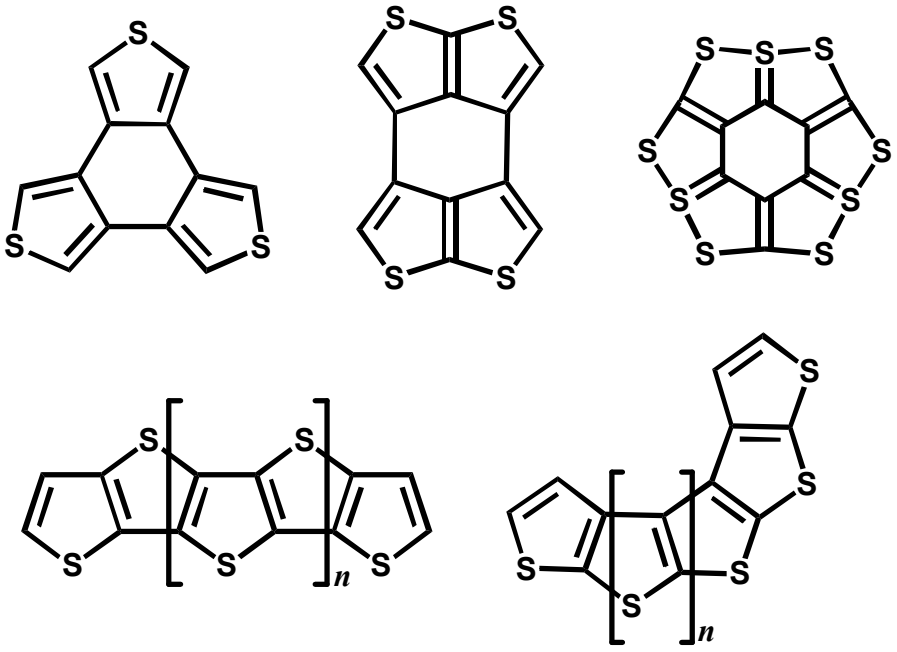

Figure 1-2. Molecular structures of thiophene compounds.

1-2. Octathio[8]circulene

For decades, highly annulated oligothiophenes remained practically unexplored because of the lack of a suitable synthetic methodology. In 2006, the synthesis of octathio[8]circulene, also known as "sulflower" (**1**, see Figure 1-3), was achieved by Nenajdenko and colleagues.[24] This molecule is attracting much attention for several reasons: its molecular symmetry, which arises from the antiaromaticity with the 8π electrons on the inner ring and orbital degeneracy; its intermolecular packing, which is characterized by sulfur atoms exposed to the outside of the molecular rings; and its potential applications in organic electronics. According to the quantum chemical calculations of Nenajdenko *et al.*, the strain is minimized in the flat, fully thiophenyl circulenes that contain eight or nine thiophene rings. To cope with the strain, lower members distort into crown-shaped structures, and contain larger number of units, create corrugated structures.

In the study of Nenajdenko *et al.*, the compound **1** was obtained from vacuum pyrolysis treatment of the parent compound, tetrathiophene (**2**), in the form of a red powder. The molecular and crystal structures were estimated from powder X-ray diffraction, and it was concluded that **1** consisted of a closed packing structure with short intermolecular S···S contacts. Although the synthesis of **1** has attracted much attention, there has been no single-crystal X-ray analysis; the molecular structure of **1** has been open to debate on bond lengths and anti-aromaticity.

This compound is a promising material in organic electronics, due to a characteristic electronic structure caused by its high symmetry, the close packing in the 3D crystal structure, and its chemical stability. Perepichka *et al.* fabricated organic thin film

transistors (OTFTs) of **1** with Au electrodes and SiO_2 gate-dielectrics, and demonstrated a hole mobility of 9×10^{-3} cm^2 V^{-1} s^{-1}, with a threshold gate voltage of −45 V.[25] These results indicate the high potential of **1** for applicability to organic electronics, though the relatively high threshold gate voltage is a weak point in terms of practical use. It is also necessary to carry out a detailed analysis of the solid-state electrical-transport of **1**, such as the temperature-dependent behavior, and to examine the chemical-doping effects to the thin films of **1**.

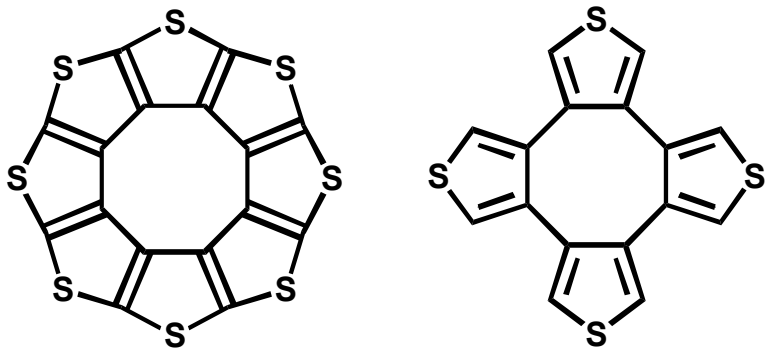

Figure 1-3. Molecular structures of octathio[8]circulene (**1**) and tetrathiophene (**2**).

1-3. Organic Field-Effect Transistors

Organic compounds have attracted much attention in organic electronics because of their various advantages, such as flexibility, light weight, low-cost fabrication and easy modification. The chemical variety of organic compounds enables systematic screening to determine which compound will perform best in a given device. The recent progress in the development of organic electronic devices such as field effect transistors, light emitting diodes and solar cells is of considerable interest due to their practical advantages.[26–30]

The field effect transistor (FET) technique is useful to tune the electric states of organic compounds, in addition to chemical doping. The FET and related field-gated structure are suitable for electric-field tuning of the surface carrier density, which has played a dominant role in recent electronic and optical technologies. The FET mechanism has the advantages of controlling the number of injection charges from gate-dielectrics, while chemical doping has many problems that must be overcome before achieving a high charge accumulation, being demanded specific and toxic treatments, and its irreversibility, in addition to hardness of controlling the charge carrier density.

Figure 1-4 shows a standard organic field effect transistor (OFET) structure. For the active semiconductor layer, aromatic hydrocarbons such as pentacene and rubrene have been extensively studied because of their high hole mobilities.[31–35] While most of the organic compounds show *p*-type behavior, fullerene and its derivatives exhibit *n*-type transport.[36–38] Although these materials have various advantages and potential for organic electronics, there are several drawbacks in their practical use, such as their

unsuitableness in air and water, and the chemical variety is very limited. To solve these problems, heteroatoms are utilized to form an organic skeleton in which strong intra- and/or intermolecular interactions can be induced, leading to molecular framework stabilization.

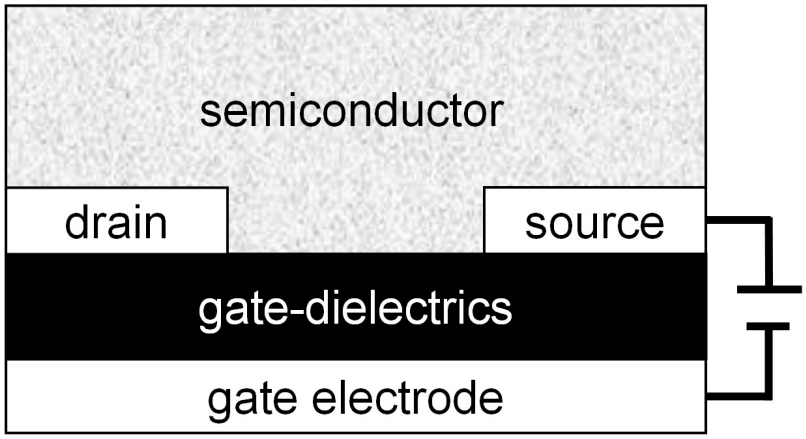

Figure 1-4. Schematic illustration of bottom gate bottom contact type field effect transistor (FET).

While various organic components have been adopted for the semiconductor layer, the variation of the gate-insulator is very limited. For decades, the semiconductor silicon and its native oxide have been used for the gate-dielectrics of FETs. There are, however, important niche applications in which it is desirable to use field-gate organics, polymers, nanocomposites, complex oxides, and/or low carrier density metals for a multiplicity of applications.[39–41] In response to these challenges, one promising and well studied area of investigation is the use of electrochemical techniques to study

surface resistance changes at the interface between a semiconductive layer and an electrolyte.[42–44] The advantages of such a gate dielectric material are low power operation, flexibility, easy device fabrication, transparency, and thermal and chemical stability.

Depending on the application, the choice of components for a field-gated device can depend critically on cost, durability, speed of operation, impedance, transconductance, and extent of modulation of the semiconductor between the source and drain. An important figure of merit for prospective gate-dielectrics is the specific capacitance, which determines how much charge can be induced in the semiconductor channel of FETs for a given applied gate voltage. The accumulated charge of parallel-plate capacitor Q has the relationship of

$$Q = CV, \tag{1-1}$$

where, C and V are the applied voltage and capacitance, respectively. The source-drain current at saturated region I_D^{sat} of the FET structure can be expressed by the following equation:[26,45]

$$I_D^{sat} = \frac{\mu WC}{2L}(V_G - V_T)^2, \tag{1-2}$$

where, L and W are the channel length and width, μ is the mobility, and V_G and V_T are the gate voltage and threshold voltage, respectively. From these equations, the higher capacitance translates into higher induced charge densities and therefore both higher currents and lower switching voltages.

1-4. Electric Double Layer Transistors with Ionic-Liquid

A major goal of organic electronics is the development of compatible materials sets, including conductors, semiconductors and insulators, that enable the fabrication of electronic circuitry on flexible substrates at low cost. In this regard, there has been significant interest in developing new kinds of solution processible dielectric materials that can serve as gate insulators in OFETs. Ionic liquids are good candidates in this field. They have various advantages such as high thermal and chemical stability, nonvolatility, nontoxicity, imperviousness to water, and compatibility with most materials systems.[46–49] They can be exposed to moderate potential differences without undergoing redox reactions, and they are fluid over a wide temperature range.

Ionic liquids are highly-polar low-melting-temperature binary salts composed purely of ions typically comprising nitrogen containing organic cations and inorganic anions in the liquid state.[50,51] In recent decades, interest in room-temperature ionic liquids has been growing due to their potential use as nonvolatile “green solvents”.[52–54] Since they do not contain actual solvents, ionic liquids are distinctly different from aqueous, organic, gel, or polymer electrolytes. They have attracted much attention for their potential use in electrical and electrochemical devices such as capacitors,[55,56] batteries,[57–59] solar cells,[60–62] fuel cells,[59,63,64] actuators,[59,65,66] electrochromic windows,[65,67] and numeric displays,[65] in addition to their applicability to FETs,[68–80] which have seen much progress in recent years.

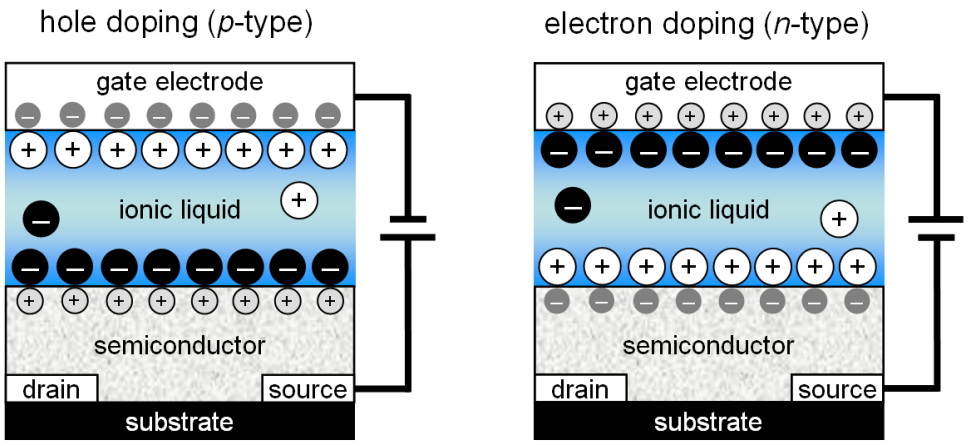

Figure 1-5. Schematic diagram of EDL-FETs with hole (left) and electron (right) injection.

FETs require high charge carrier injection at the semiconductor/insulator interface. The capacitance of the parallel-plate capacitor is represented by

$$C = \frac{\varepsilon_0 \varepsilon_r A}{d}, \tag{1-3}$$

where ε_0 and ε_r are the vacuum and relative permittivity, and A and d are the area of the plate and distance between two plates. Although the relative permittivity of ionic liquids is about 1–20,[81–84] ionic liquids are considered to form electric double layers (EDLs) on the surfaces of semiconductors by composed ions with one molecular layer (see Figure 1-5), and will lead to a high capacitance of ~10 μF cm^{-2}, which realizes high-density carrier injections that are higher by orders of magnitude than those of the SiO_2 gate-dielectrics.[85] For example, a 300 nm thick layer of SiO_2 has a capacitance of 10 nF cm^{-2}. The typical sheet carrier density attainable in conventional inorganic-dielectric FET structures is only ~10^{13} cm^{-2}, which is still unsatisfactory for

inducing a change in the electric and/or structure transition, such as the induction of superconductivity or ferroelectricity. However, such experiments have so far been limited to modulation of the critical temperature in originally conducting samples because of the dielectric breakdown. The EDL-FETs structure could solve these problems, because it can achieve extremely high carrier densities up to 10^{15} cm^{-2}.[69,86–88]

While the electrolyte solution with organic and/or water solvent is volatile and unstable in air, and it is hard to maintain the concentration of solution at a constant level, the ionic liquids can solve these problems because of their nonvolatility and air stability. In addition, low molecular weight and high polarizability make ionic liquids much more conductive than an electrolyte, and this increased conductivity is responsible for the rapid switching behavior of ionic-liquid gate-dielectric EDL-FETs.[69,77,89] This switching behavior is also in contrast to polymer electrolyte dielectrics, since the polarization relaxation time is strongly related to the conductivity of the polymers electrolyte.[90]

It is also expected that ionic liquids would produce additional benefits for OFETs, such as low power operation, flexibility, easy device fabrication, transparency, and thermal and chemical stability, in addition to the fact that ionic liquids exhibit no crack and localized dielectric breakdown, which often spoil the performance of conventional solid-state transistors.[91,92]

1-5. Summary

The organic compounds containing sulfur atoms have great potential due to their metallic conductivity, superconductivity, and applicability to organic electronics. Compound **1**, which is a newcomer in this materials family, has an interesting framework and crystal structure. The analysis of the fundamental properties of this compound, including the molecular and crystal structure, electronic state, conductivity behavior and chemical doping effect will be important to reveal the physical characteristics. In addition to these basic researches, studies on the suitability of compound **1** to organic applications would make a great contribution to the development of the organic electronics field.

For FET application, the EDL-OFET structure is attractive because it can achieve a high charge carrier injection. Ionic liquid is a good candidate in this field, and it would be a worthwhile pursuit to combine organic semiconductors and ionic liquids to realize flexible electronics. The choice of organic semiconductors for EDL-OTFTs has been limited, due to their high solubility in ionic liquids. Nevertheless, compound **1** is a promising material since it can form a robust thin film due to the strong intermolecular interactions through the sulfur atoms exposed at the outside of the molecular ring.

This thesis is composed of five chapters: Chapter 2 presents the crystal structure and electronic properties of octathio[8]circulene. In addition, ionic liquid EDL-OTFTs of octathio[8]circulene were fabricated and the controlling factors of the EDL-OTFT operation were investigated in Chapter 3. In Chapter 4, the EDL-FETs with other robust organic materials were fabricated and complementary inverters by combination with *p*- and *n*-type semiconductors were demonstrated.

Chapter 2

Crystal Structure and Electronic Properties of Octathio[8]circulene

2-1. Introduction

Carbon-sulfur compounds have been studied extensively as key materials in organic/molecular electronics due to the strong inter- and intra-molecular interactions occurring from the widespread atomic orbitals of the sulfur atom. As is mentioned in the previous chapter, octathio[8]circulene (**1**) is a newcomer in this materials family.

In the present work, the single-crystals and thin films of **1** were prepared. The molecular, crystal, and thin-film structures of **1** are described in detail, based on the results of X-ray single-crystal analysis, in comparison with those of **2**. Further, the highly oriented thin films of **1** were fabricated by vacuum evaporation and the electronic structure was examined by thin-film electrochemistry in ionic liquids. The solid-state electric-transport properties were evaluated by means of temperature-dependent conductivity and thin-film transistor (TFT) measurements. The chemical doping effect with acceptor molecule, 7,7,8,8-Tetracyanoquinodimethane (TCNQ) and iodine (I_2) were also performed to the thin film of **1**.

2-2. Experimental

Compounds **1** and **2** were prepared by the methods given in references [24] and [93], respectively. Single crystals of the parent compound **2** were grown by slow evaporation of the Et_2O solution at room temperature, and single crystals of **1** were obtained as red needles by vacuum sublimation.

Single-crystal X-ray diffraction data were collected on a Rigaku RA-Micro007 CCD diffractometer with graphite-monochromated Mo$K\alpha$ radiation (λ = 0.710690 Å). The measurements were carried out at 173 K. The structures were solved by direct methods and refined by the full-matrix least squares method on F^2 using SHELXL97. All hydrogen atoms were placed at calculated positions.

The thin films of **1** with a thickness of 500 nm were prepared by vacuum vapor-deposition at 400°C under 3×10^{-4} Pa at a rate of 2–6 nm min^{-1}, using a ULVAC VPC-260FN vacuum coater. The film thickness was monitored during deposition by a quartz crystal microbalance located adjacent to the sample position within the bell jar.

Dynamic AFM and SEM measurements for the thin films (500 nm) of **1** on ITO substrate were carried out on SII SPI3800 and Hitachi S-4300, respectively. Out-of-plane and in-plane X-ray diffractions of the thin films were recorded on a Rigaku SmartLab X-ray diffractometer.

The CV measurements were examined for the thin films (500 nm) of **1** on ITO substrate in DEME-TFSI (**IL1**), in the potential range 0.6–1.5 V *vs.* Ag/AgCl with a slow scanning rate of 1 mV s^{-1} (see Figure 2-1). The upper limit of the potential is caused by the oxidation of **IL1**.

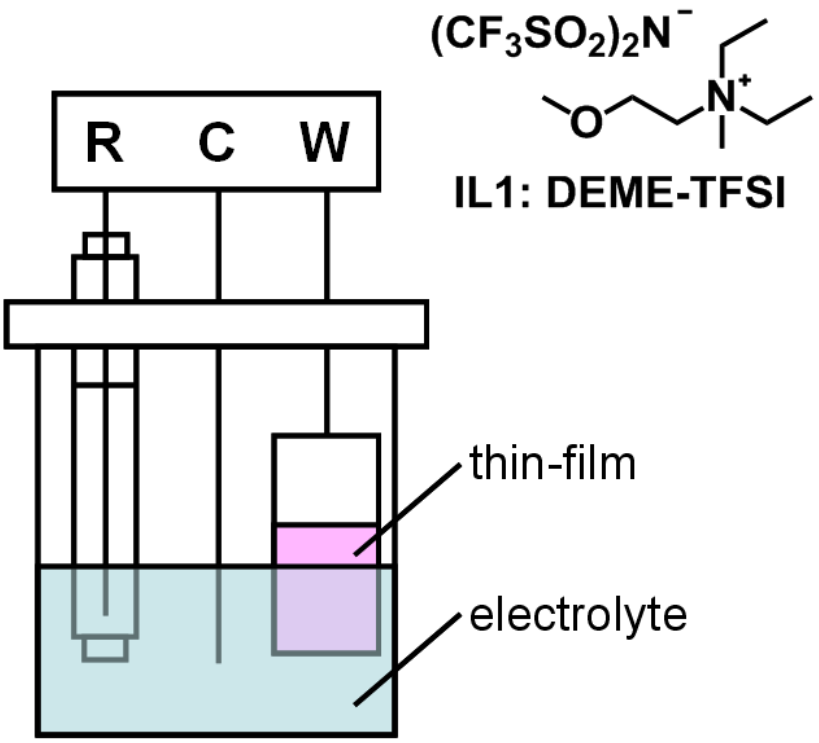

Figure 2-1. Measurement set-up for the thin-film electrochemistry. The inset shows molecular structure of ionic liquid DEME-TFSI (**IL1**) for electrolyte.

Conductivity, TFT and acceptor doping effect measurements for the thin films of **1** were carried out for the vacuum vapor-deposited thin film, prepared on Pt interdigitated array electrodes. The electrodes were prepared by photolithography on surface-oxidized *n*-doped Si substrates (SiO_2: 300 nm), for which the channel dimensions correspond to w = 100 cm width and L = 2 μm length. The conductivity and TFT performances were examined under dark condition.

2-3. Results and Discussion

2-3-1. Molecular and Crystal Structure

2-3-1-1. Tetrathiophene (Compound 2) -Precursor of Octathio[8]circulene-

While the X-ray structure of **2** has been reported previously,[94] a new polymorph belonging to the monoclinic $P2_1/c$ space group was obtained (see Table 2-1). In this polymorph, there are two crystallographically independent molecules, whereas their molecular structures are nearly the same. Figure 2-2 shows top and side views of one of the two molecules. The bond lengths of **2** are shown in Table 2-2, where the *endo* bond is the one shared by the eight- and five-membered rings, the *exo* bond is connecting two thiophene rings, and the *exocylic* C=C bond is *exocyclic* to the eight-membered ring. The eight-membered inner ring of **2** exhibits a tub conformation, in contrast to the planar molecular structure of a six-membered-ring derivative, benzo[1,2-c:3,4-c′:5,6-c″]trithiophene.[15] The C−C bond lengths in the central eight-membered ring are between the typical ones of C−C (1.54 Å) and C=C (1.34 Å), and exhibit a clear bond alternation; the *endo* bonds are shorter than the *exo* bonds by 0.04 Å, reflecting the anti-aromaticity of 8π-electron systems.

Table 2-1. Single-crystal XRD results for compound **1** and **2**.

	Compound **1**	Compound **2**
Chemical formula	$C_{16}S_8$	$C_{16}H_8S_4$
Formula Mass	448.66	328.48
Crystal color, shape	red, needle	colorless, block
Space group	$P2_1/n$	$P2_1/c$
a / Å	3.869(2)	7.3506(8)
b / Å	16.529(9)	19.502(2)
c / Å	11.146(6)	19.558(2)
β / º	94.023(10)	90.5427(15)
V / Å^3	711.0(7)	2803.6(6)
Z	2	8
T / K	173	173
μ(MoKα) / cm^{-1}	12.484	6.609
ρ / g cm^{-3}	2.096	1.556
Total Reflections	5559	22234
Independent Reflections	1604	6397
R_{int}	0.071	0.054
R ($I > 2.00\sigma(I)$)	0.0565	0.0416
R (All reflections)	0.0842	0.0496
wR (All reflections)	0.1681	0.1362
Goodness of fit	1.069	0.986

Table 2-2. Averaged values of the bond lengths for **1** and **2** [Å].

	***endo* shorter**	***exo* longer**	**cyclic *exo***	C−S
1	1.436(4)	1.477(4)	1.369(4)	1.708(2)
2	1.412(1)	1.430(4)	1.372(7)	1.753(6)

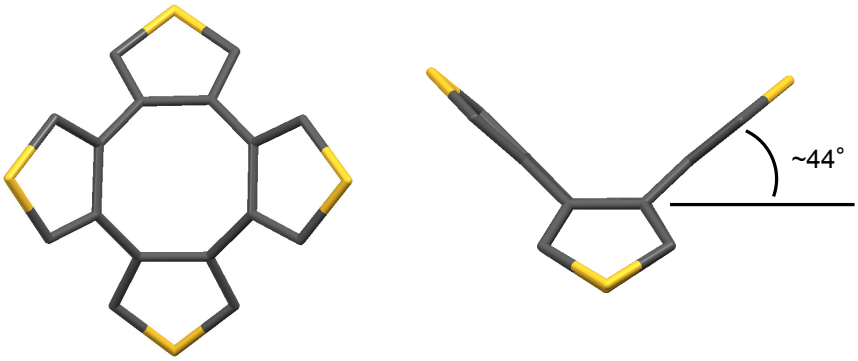

Figure 2-2. Top and side views of the molecular structures of **2**.

Figure 2-3 shows the third HOMO of **2**, which was obtained by means of the DFT B3LYP[95] method with a 6-311+G(d,p) basis set. This orbital clearly indicates a bonding character between the facing thiophene rings on opposite sides of the eight-membered ring. This must be the reason for the tub formation in **2**, in addition to the intramolecular steric effect between the hydrogen atoms on the neighboring thiophene rings.

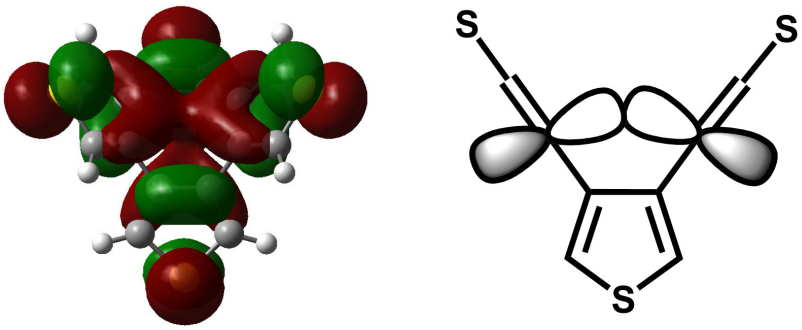

Figure 2-3. Third HOMO of **2**.

Figure 2-4 depicts a view of the unit cell of **2**. The molecules, denoted as **A** and **B**, are crystallographically independent. Their intermolecular arrangement includes short distances between the thiophene rings with C···C distances of 3.50–3.74 Å, where the thiophene rings are arranged to be nearly perpendicular with each other. This arrangement is indicative of the C−H···π interactions. Other than these contacts, there is no significant π–π overlaps or short S···S contacts in **2**.

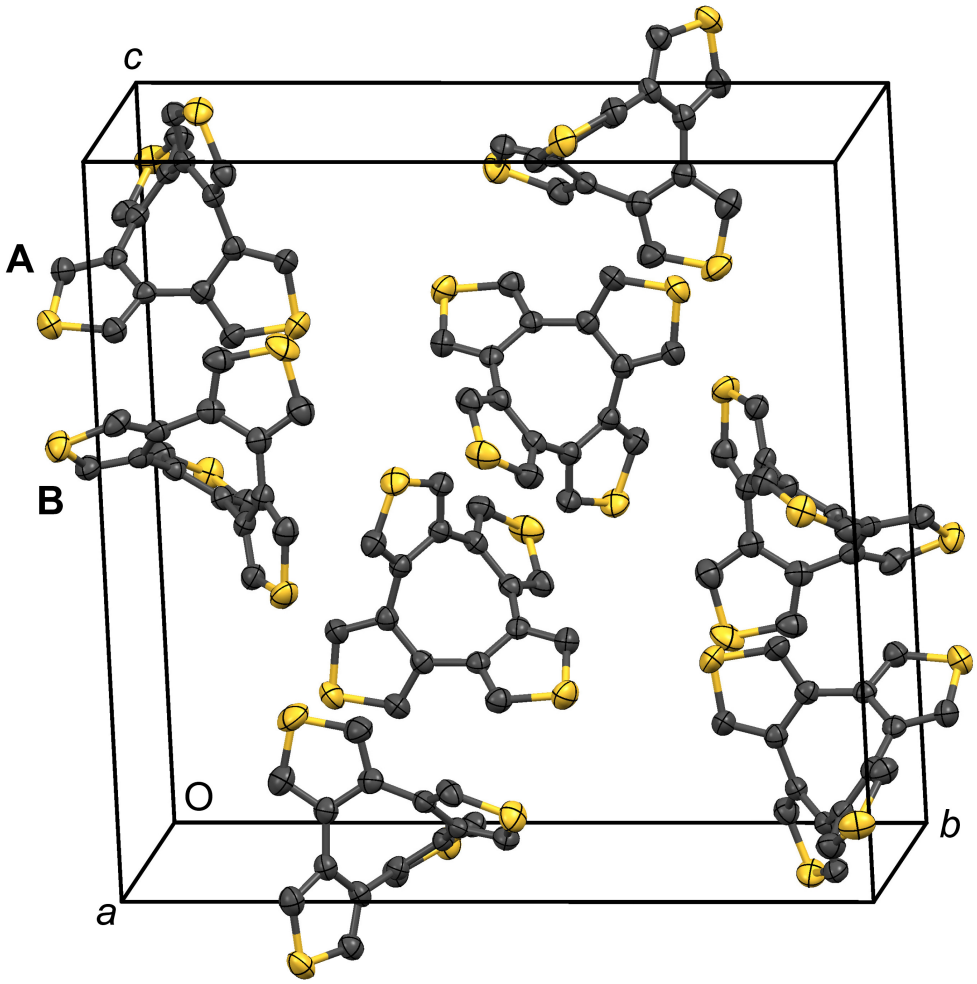

Figure 2-4. A view of the unit cell of **2**.

2-3-1-2. Octathio[8]circulene (Compound 1)

X-ray analysis was carried for the single crystal of compound **1**. The space group was found to be the monoclinic $P2_1/n$ (see Table 2-1), while it was assigned to the non-centrosymmetric $P2_1$ in the previous Rietveld analysis.[24] The symmetry, obtained in the present re-determination of the crystal structure of **1**, reduced the size of the asymmetric unit to one-half molecule. Regarding the molecular packing, that obtained in the present work was essentially the same as that in the powder X-ray study.[24]

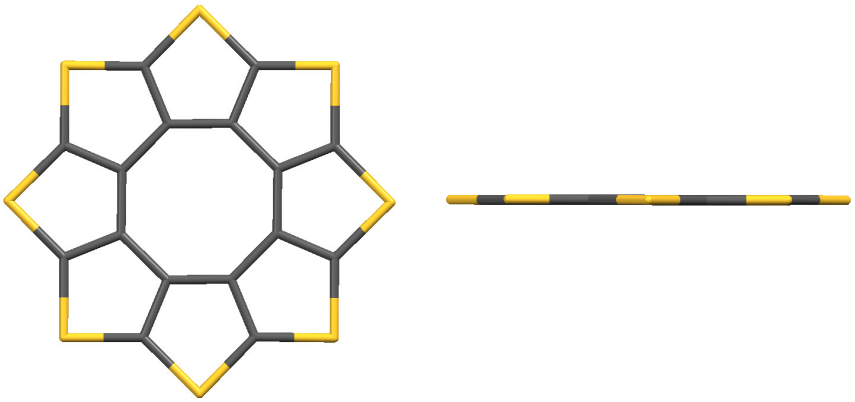

Figure 2-5. Top and side views of the molecular structures of **1**.

Figure 2-5 shows top and side views of the molecular structure of **1**. In contrast to the tub formation in **2**, the molecule **1** has a very planar structure, as theoretically predicted previously.[24] The inner eight-membered ring exhibits an obvious bond alternation, but it is much less significant than that in **2**. Although the *endo* and *exo* bonds cannot be defined in the molecular skeleton of **1**, the values of the shorter and

longer bond lengths are listed in the columns of the *endo* and *exo* bonds, respectively, in Table 2-2. The C−C bond lengths on the inner ring of **1** are found to be shorter than those of **2**, suggesting an enhancement of the double-bond character, but still longer than those in benzene (1.399 Å). The distances of the *exocyclic* C=C bonds in **1** are similar to those in **2**, while those of the C−S bond are longer in **1**. It is notable that there is no bond alternation on the outer C−S sixteen-membered ring in **1**.

Figure 2-6 shows the nearly degenerated third and fourth HOMOs of **1**, which were calculated with the same method used for compound **2**. One can be superimposed on the other by the rotation of 45° around the molecular axis. Each orbital alternately provides π-bonding character to the C−C bonds on the inner eight-membered ring. It is considered that the presence of these two molecular orbitals makes the bond alternation on the inner ring less significant; the structural distortion caused by the 8π-electron antiaromaticity of **1** is released by the pseudo-C_8 symmetry in the outer ring.

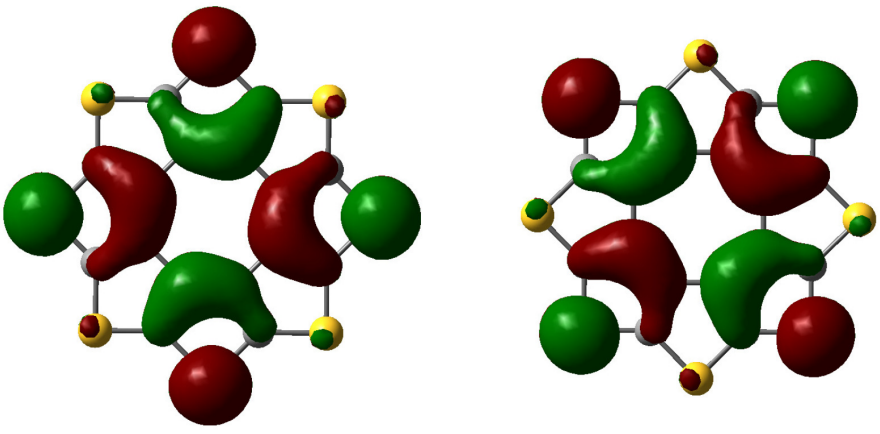

Figure 2-6. Nearly degenerated third and fourth HOMOs of **1**.

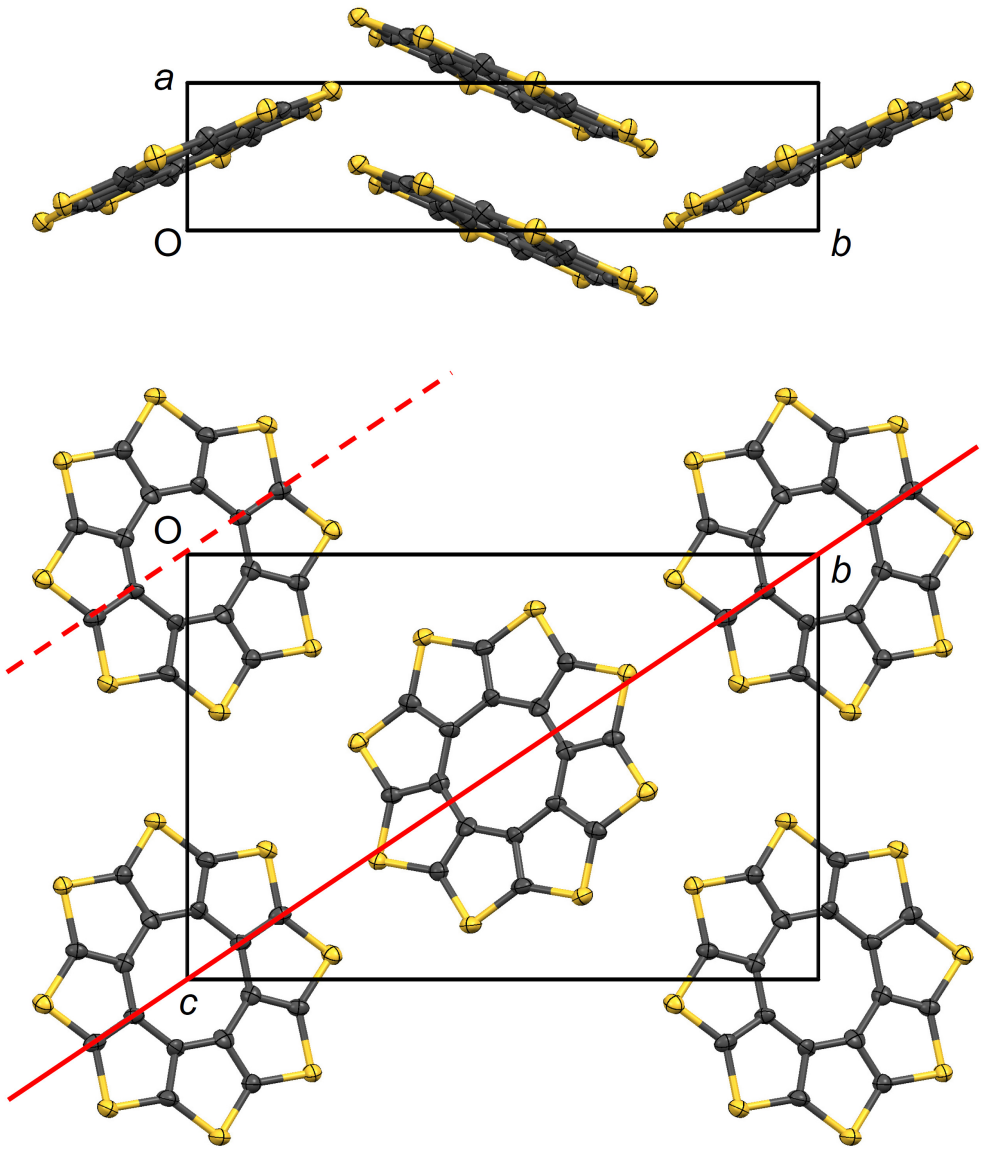

Figure 2-7. Projections of the crystal structure of **1** along the *c* and *a* axes. The red line shows the (011) plane.

Figure 2-7 shows projections of the unit cell of **1** along the *a* and *c* axes. There is a one-dimensional π-stacking column along the *a* axis, which is surrounded by six neighbors with short S···S contacts. These features were reported in ref. [24]. Figure

2-8(a) depicts the intermolecular overlap of the two neighboring molecules in the π-stacking column. This figure indicates a shifted overlap so as to release electrostatic repulsions between the sulfur atoms. Figure 2-8(b) shows a space-filling view of the intercolumnar arrangement. The shifted π-stacking makes small cavities into which the sulfur atoms in the neighboring columns are inserted, creating an interdigitated structure.

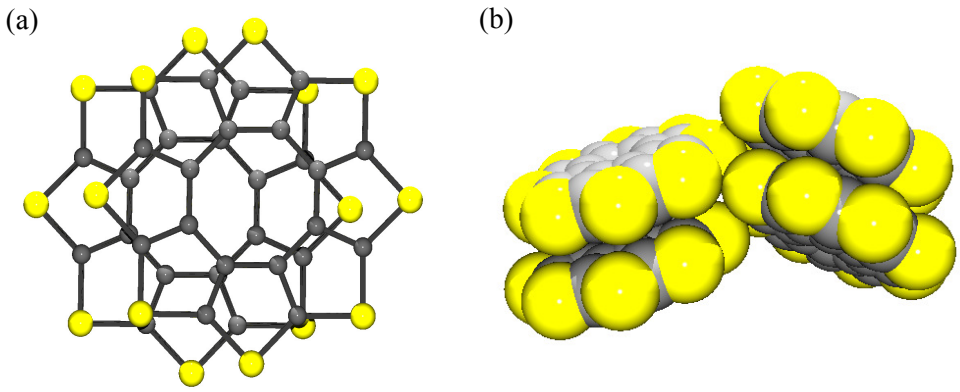

Figure 2-8. (a) Intermolecular overlap between two neighboring molecules in the stacking column of **1** and (b) space-filling view of the intercolumn arrangement in **1**.

To discuss the aromatic character of compounds **1** and **2**, the values of the nucleus-independent chemical shift (NICS) and the harmonic oscillator model of aromaticity (HOMA) were calculated. NICS values are computed at selected points inside or around molecules, typically at ring centers and above.[96,97] NICS(1) values is recommended, i.e., 1 Å above the ring centers, where the local contributions are diminished relative to the ring current effects, be employed as an aromaticity index,

rather than NICS(0) (computed in the ring centers).[98–100] When NICS is less than zero, the compound is aromatic while compound is anti-aromatic if NICS is greater than zero. Another method is HOMA, which was put forward by Kruszewski and Krygowski with the formula of

$$\mathrm{HOMA} = 1 - \frac{\alpha}{n}\sum_{i=1}^{n}\left(R_{\mathrm{opt}} - R_i\right)^2 , \qquad (2\text{-}1)$$

where n is the number of bonds considered, and α is a fixed empirical constant (for C−C bonds, α = 257.7), R_{opt} is 1.388 Å and R_i are the calculated bond lengths from experimental results.[101,102] An aromatic ring has a HOMA value of 1, whereas a nonaromatic compound has the zero value.

Table 2-3 lists the NICS(0), NICS(1) and HOMA values calculated by the B3LYP/6-311+G(d,p) level. The compounds **1** and **2** have positive NICS values in the central 8-membered ring; accordingly, the inner rings of these compounds are anti-aromatic, while the heterocyclic rings have a negative value due to their aromatic character. However, the HOMA value of compound **1** is 0.672, and thus **1** has an aromatic character. This is somewhat contradicted by the findings from these calculations. Therefore, more precise calculations should be performed to clarify the aromaticity of **1**.

It is noteworthy that the values of NICS(0) and NICS(1) of the heterocyclic ring for compound **1** are smaller than those of compound **2**, which indicates that this conjugated structure decreased the native thiophene aromatic character of **1**. On the other hand, the molecular structure of compound **2** tended to remain unconstrained.

Table 2-3. NICS and HOMA values of compound **1** and **2**.

	Central 8-membered ring			Heterocyclic rings	
	NICS(0) / ppm	NICS(1) / ppm	HOMA	NICS(0) / ppm	NICS(1) / ppm
1	5.629	2.810	0.672	−9.712	−6.649
2	2.965	1.265	−0.428	−11.686	−9.152[a]/−8.854[b]

*NICS(1) values for compound **2** are calculated both two sides of the thiophene ring located at inner (a) and outer (b) side of tub conformation.

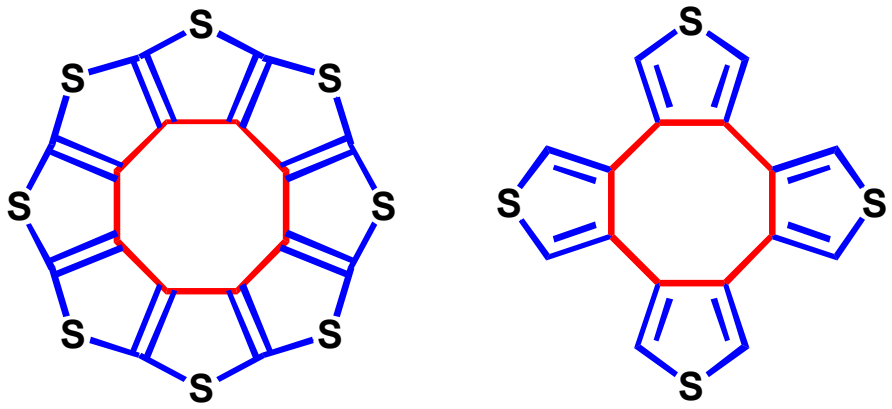

Figure 2-9. Definition of central 8-membered ring (red line) and heterocyclic rings (blue line) for compounds **1** and **2**.

2-3-2. Thin-Film Structure

Thin films of **1** were prepared on Si(100), SiO_2 and ITO substrates. Figure 2-10(b) shows the AFM image of the thin film on a ITO substrate, with a thickness of 500 nm. From this image, the thin film possesses a smooth surface and the grain size can be estimated as ~100 nm. SEM images also indicate that the flat surface structure is maintained (see Figures 2-10(c) and (d)). The thin film of **1** (500 nm) looks faint red (see Figure 2-10(a)), but this color is probably caused by an interference effect due to the film thickness and/or intermolecular S···S interactions.

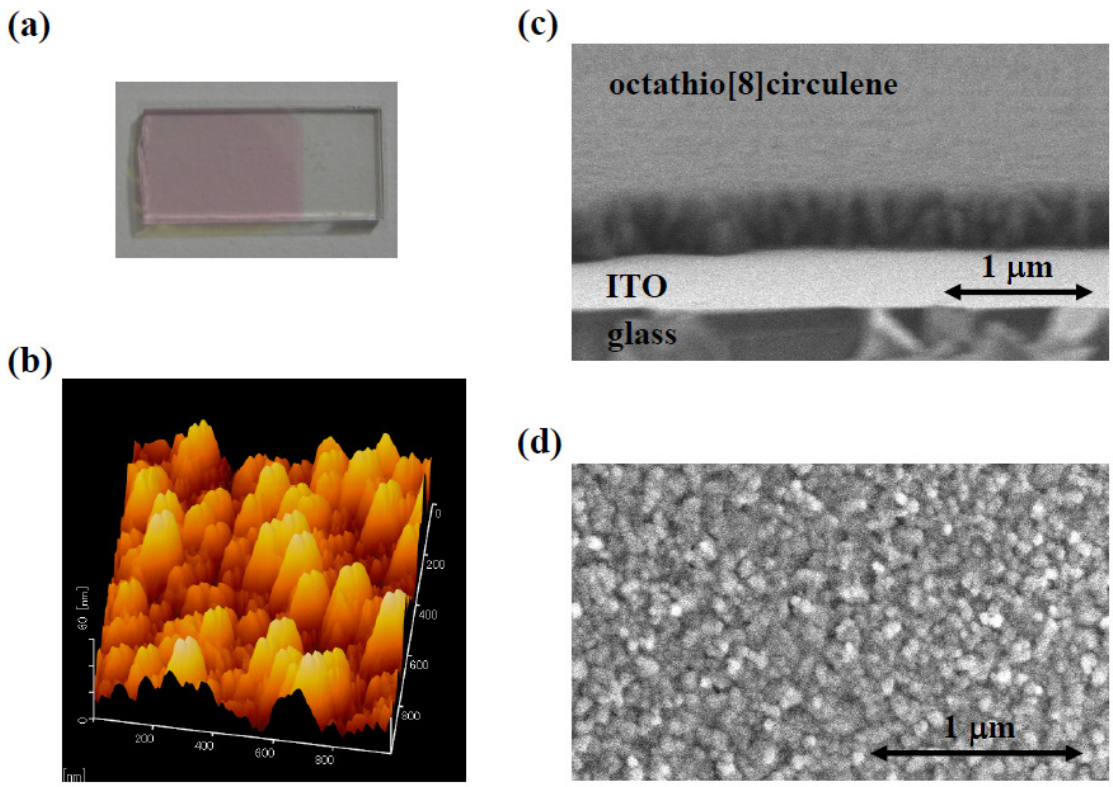

Figure 2-10. A photograph (a), AFM image (b), and SEM images of a cross-section (c) and the surface (d) of a thin film of **1** (500 nm) on ITO substrate, respectively.

Figure 2-11 shows the UV/vis/NIR absorption spectrum for the thin film (10 nm) of **1** on SiO_2 substrate. It exhibits a strong absorption at 4.7 eV in the UV range, but there is no significant absorption peak in the visible range, namely, below 3 eV.

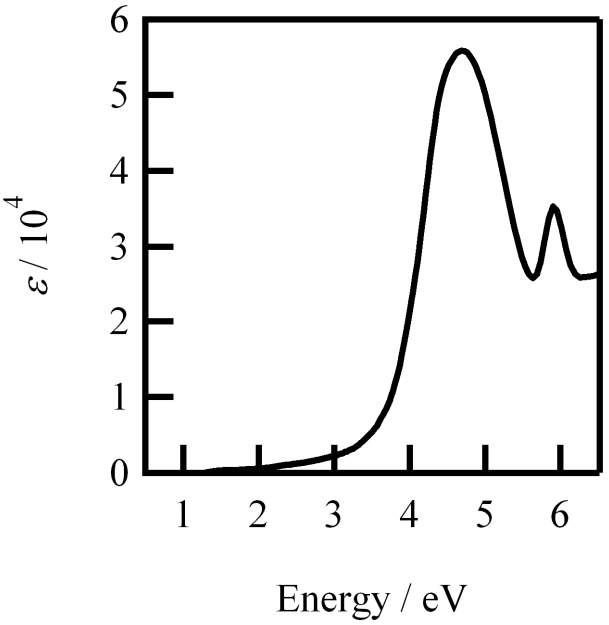

Figure 2-11. UV/vis/NIR absorption spectrum for the thin film of **1** (10 nm) on quartz.

Figure 2-12 shows the X-ray diffractions (XRD) for this thin film of **1** on Si(100). The out-of-plane measurements (red line) indicate several diffraction peaks, whose assignments are shown in this figure. Since the diffraction from the (011) plane (d = 0.929 nm) at 2θ = 9.5° (d = 0.913 nm) is much stronger than those of the others, the thin film is considered to have a lamellar structure, in which the (011) plane is parallel to the substrate. The red line in Figure 2-8 shows the (011) plane. It is reasonable to conclude that the molecular planes of **1** are all perpendicular to the substrate in this

thin film. This type of perpendicular molecular plane alignment is typical for the thin films of organic π molecules because it is advantageous for gaining both π–π stacking stabilization and a high density on a unit area of the substrates.[103,104] The in-plane XRD pattern (blue line) shows very weak diffractions; there is no characteristic diffraction. This suggests little long-range periodicity in the in-plane structure. The XRD patterns of the thin films of **1** on ITO are essentially the same as those on Si(100).

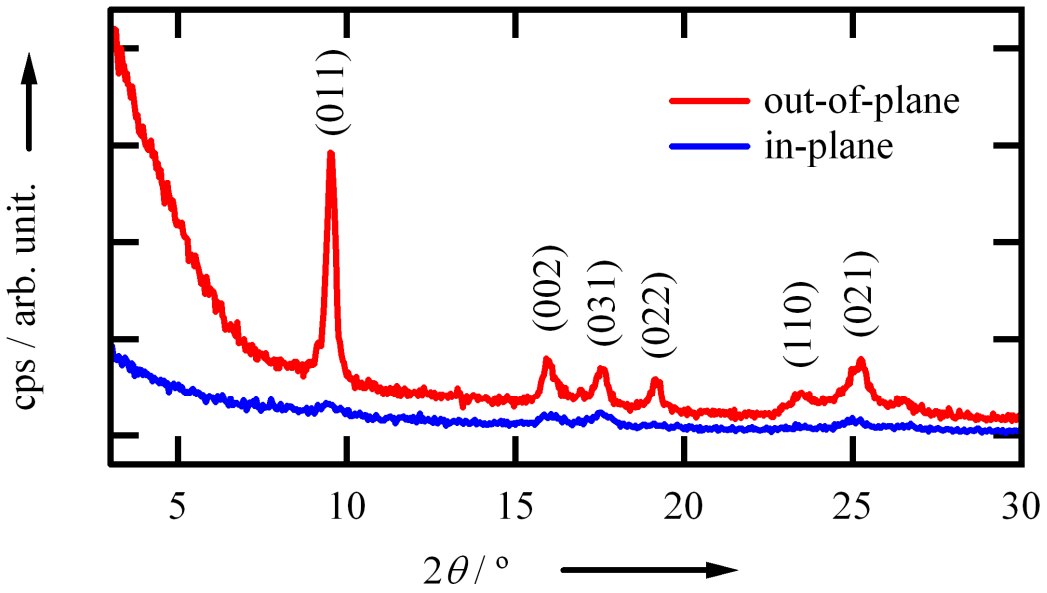

Figure 2-12. Thin-film XRD patterns of **1** on Si(100). The red and blue lines show the results of the out-of-plane and in-plane scans, respectively.

2-3-3. Thin-Film Electrochemistry

Since compound **1** is insoluble in aqueous and organic solvents, it is difficult to apply conventional methods of solution electrochemistry. Therefore the electrochemistry of the thin films of **1** was examined using the same method as that applied to insoluble organic polymers[105,106] and phthalocyanine derivatives.[107–115] Although the thin films of **1** easily peeled off during electrochemical reactions in organic solvents, they were stable enough to exhibit a repeatable redox process in ionic liquids such as DEME-TFSI (**IL1**), with wide electrochemical windows.[56,116]

The broken curve in Figure 2-13 shows the results of the first run; the oxidation curve shows a gradual increase above E = 1.1 V, suggesting the oxidation of **1**, but does not make a peak in the window range, probably due to the so-called over potential effect.[117–119] It is recognized that the first redox process needs an extra potential for an irreversible penetration of counter ions into films. The first reduction scan clearly exhibits two peaks at 0.95 and 0.75 V. The solid curve in Figure 2-13 shows the results in the second run. This curve clearly exhibits a large oxidation peak at 1.11 V and two reduction peaks at the same potentials as those in the first scan. The sum of the intensities of the two reduction peaks is nearly the same as that of the oxidation peak. In the third cycle and after, the peak positions are the same as those of the second run, but the peak intensities are slightly increased. This suggests that the redox reactions do not completely occur in the thin film and the redox active part in it is gradually increased in this repetition. Compound **1** is concluded to be a donor.

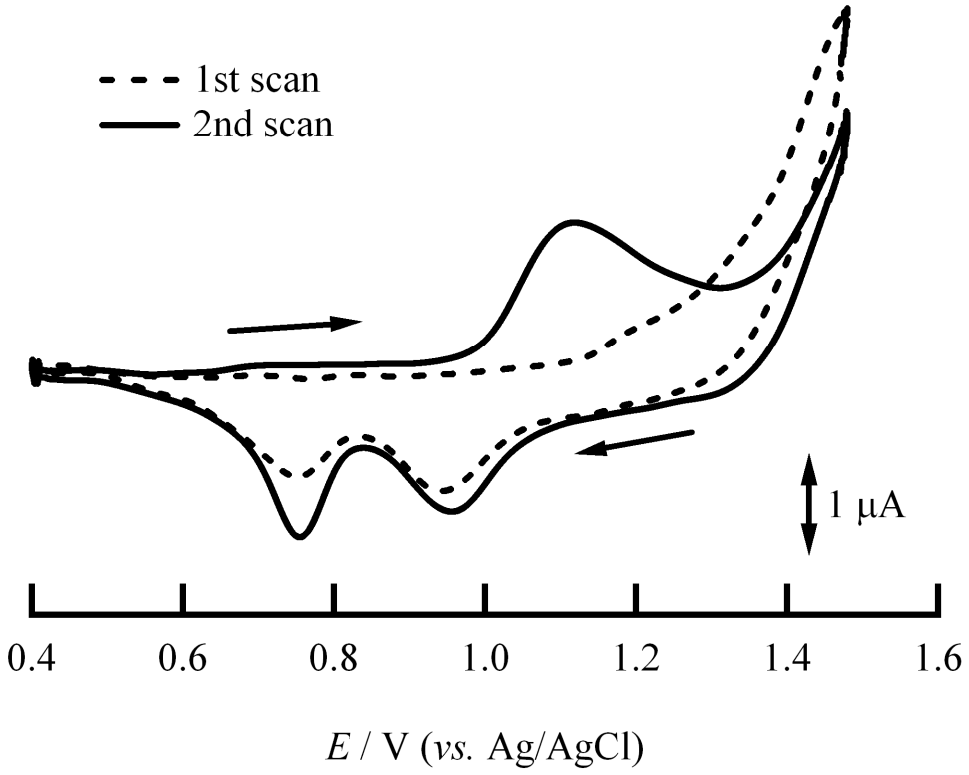

Figure 2-13. CV curve of a thin film of **1** on ITO in **IL1** with a scanning rate of 1 mV s^{-1}.

During the CV measurements, the thin films of **1** undergo a significant color change, as indicated in the inset of Figure 2-14. The thin film at 0.0 V looks faint red, discussed in section 2-3-2. After the oxidation, the color turns to blue at 1.5 V. In the reduction process from this potential, the color becomes dark red at 0.8 V and then colorless (faint red) at 0.0 V.

In-situ UV/vis/NIR absorption measurements were carried out in the photon energy 1.4–4.0 eV for the thin film (500 nm) of **1** in the reduction scan at E = 1.5, 0.8 and 0.0 V. Due to the strong absorptions of ITO and **IL1**, reliable data above 4.0 eV and below

1.4 eV were not obtained. The results for the ranges 1.4–4.0 and 1.7–2.6 eV are shown in Figures 2-14 (a) and (b), respectively, while the absorptions of ITO and **IL1** are not compensated in them. The black curve at E = 0.0 V corresponds to the absorption of the neutral species $\mathbf{1}^0$; there is no absorption peak in this range. The blue curve at E = 1.6 V and the red curve at 0.8 V exhibit absorption peaks at 2.07 and 2.21 eV, respectively, while the intensity of the former is much larger than that of the latter.

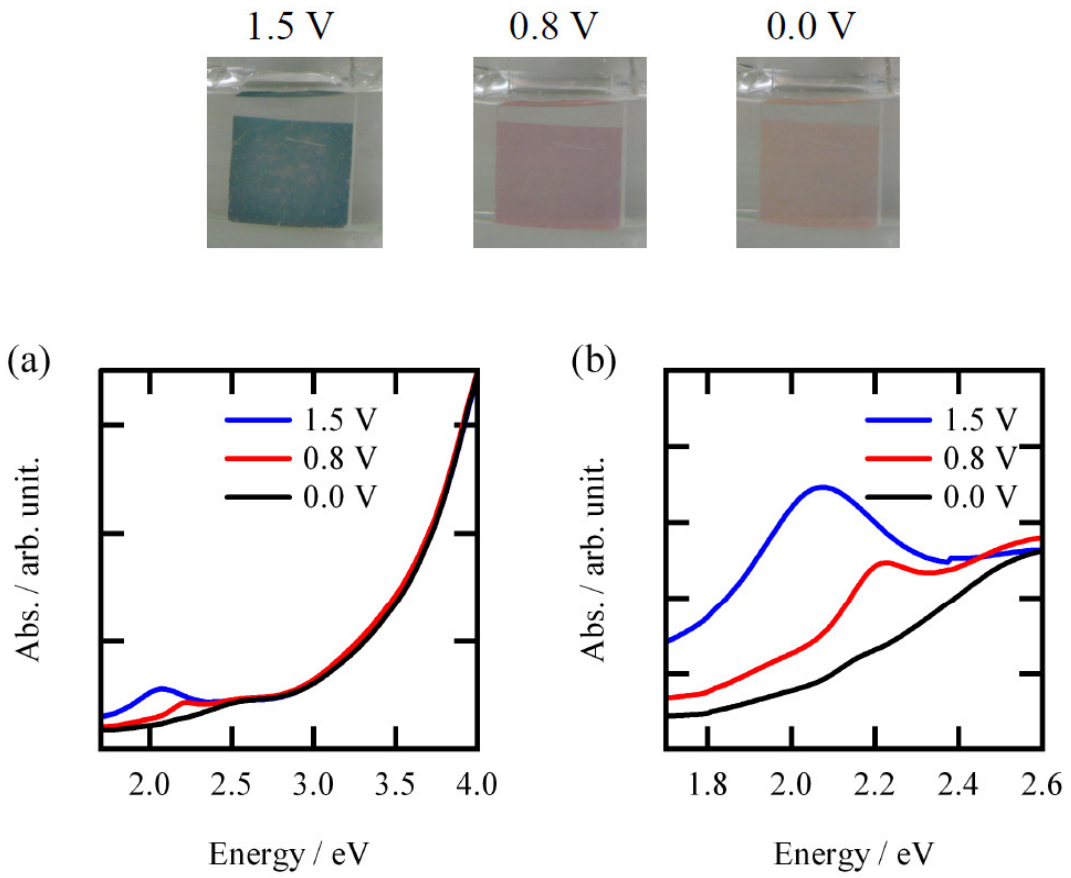

Figure 2-14. In-situ absorption spectra for the thin film of **1** (500 nm) on ITO in **IL1** in the reduction scan at E = 1.5, 0.8, and 0.0 V, for the photon energy ranges 1.7–4.0 (a) and 1.7–2.6 eV (b), respectively. The inset shows the photographs at three potentials.

To interpret the electrochromism of **1**, the molecular orbital calculations (TD-DFT B3LYP method with a 6-311+G(d,p) basis set) were carried out for $\mathbf{1}^{0}$, $\mathbf{1}^{+}$, and $\mathbf{1}^{2+}$. Figure 2-15 shows the theoretically expected absorption spectra for the three species. The figure shows that the neutral molecule $\mathbf{1}^{0}$ exhibits no absorption in the range 1.7–4.0 eV, which agrees well with the experimental results (Figure 2-11). In contrast, the monocation species $\mathbf{1}^{+}$ is suggested to exhibit a weak absorption at 2.22 eV (f = 0.119) in this energy range. The dication species $\mathbf{1}^{2+}$ is theoretically predicted to possess a triplet ground state and to exhibit two nearly superimposed weak absorptions at 2.07 eV (f = 0.157).

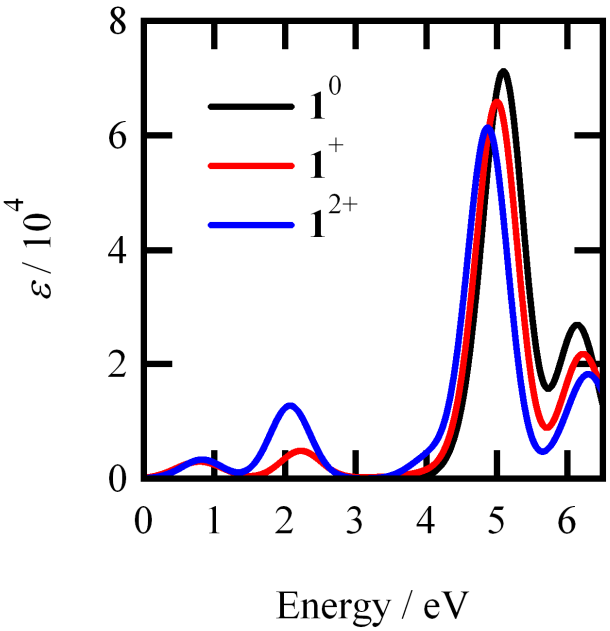

Figure 2-15. Theoretically-expected absorption spectra for $\mathbf{1}^{0}$, $\mathbf{1}^{+}$, and $\mathbf{1}^{2+}$, obtained from the molecular orbital calculations (TD-DFT B3LYP method with a 6-311+G(d,p) basis set).

These weak absorptions of $\mathbf{1}^{+}$ and $\mathbf{1}^{2+}$ have the same origin; they are mainly caused by the transition from the molecular orbital #107 to the nearly degenerated orbitals #111 and #112, as shown in Figure 2-16. Orbital #107 is a nonbonding orbital, localized on the sulfur atoms, while #111 and #112 are the nearly degenerated HOMOs of the neutral species $\mathbf{1}^{0}$. The transition from #107 to #111 or #112 is forbidden in $\mathbf{1}^{0}$ because there is no vacancy in #111 and #112. In contrast, since there are one and two vacancies in #111 and #112 for $\mathbf{1}^{+}$ and $\mathbf{1}^{2+}$, respectively, this transition is allowed in them and the absorption in $\mathbf{1}^{2+}$ is twice as strong as that in $\mathbf{1}^{+}$ (see Figure 2-15). The theoretically expected optical absorptions of $\mathbf{1}^{+}$ and $\mathbf{1}^{2+}$ can well reproduce the absorptions at E = 0.8 V (red curve) and 1.5 V (blue curve) in Figure 2-14 (b), respectively, with regard to both peak position and relative intensity. It is concluded that the CV curves in Figure 2-13 include two-electron oxidation at E = 1.11 V ($\mathbf{1}^{0} \rightarrow \mathbf{1}^{2+}$) and stepwise reductions at E = 0.95 ($\mathbf{1}^{2+} \rightarrow \mathbf{1}^{+}$) and 0.75 V ($\mathbf{1}^{+} \rightarrow \mathbf{1}^{0}$). Such a one-step two-electron oxidation/reduction is occasionally found in some specific molecules with degenerated HOMOs/LUMOs.[120,121] It is hard to clearly rationalize the stepwise reductions of $\mathbf{1}^{2+}$, but one possible reason is different geometries of the two counter anions around $\mathbf{1}^{2+}$ in the thin film.

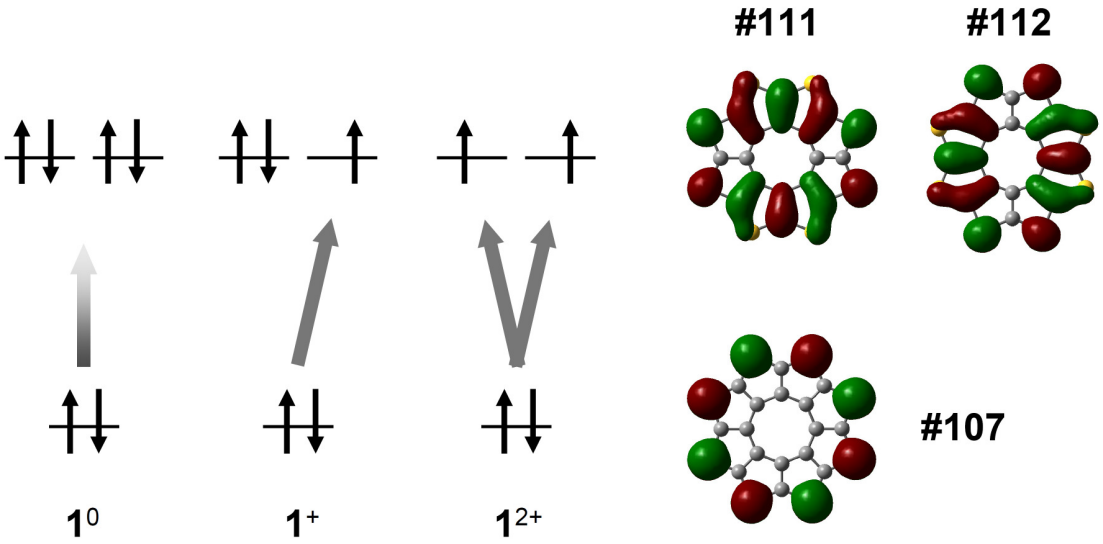

Figure 2-16. Molecular orbitals corresponding to the absorption bands in Figure 2-14(b). Molecular orbitals, #111 and #112, are the nearly degenerated HOMOs of the neutral molecule, while #107 is a nonbonding orbital localized on the sulfur atoms.

2-3-4. Solid-State Conductivity and Thin-Film Transistors

2-3-4-1. Temperature-dependant conductivity

Figure 2-17(a) shows the *J*-*V* characteristics of the thin film of **1** (20 nm) on an interdigitated array electrode under a vacuum in dark. Ohmic and space charge limited current (SCLC) transport properties are apparent at the low and high applied electric-field with slopes of 1.2 and 4.6 in the log-log plot, respectively. The conductivity calculated in the ohmic range is 2×10^{-9} S m^{-1}, which is comparable to the conductivity of the hydrocarbon circulene "coronene" ($\sigma \sim 2 \times 10^{-10}$ S m^{-1}).[122] The slope of 4.6 in the SCLC region indicates the existence of trapping states.[123] The conductivity of the thin film of **1** increases in air by the order of $10^1 \sim 10^2$ due to its air sensitivity.

Next, the temperature-dependent conductivity measurements were carried out. Figure 2-17 (b) shows the results using three applied voltages (5, 8, and 10 V). The conductivity is decreased along with the reduction in temperature in the manner of a general semiconductor. The activation energy E_a is calculated by

$$\sigma = \sigma_0 \exp\left(\frac{-E_a}{k_B T}\right), \tag{2-2}$$

where σ, σ_0, k_B and T are the conductivity, coefficient, Boltzmann constant and temperature, respectively. The activation energy E_a in the ohmic region (V = 5 V) is 0.31 eV, while the SCLC region (V = 10 V) has a lower value of 0.25 eV. These values are comparable to the well-known phthalocyanine (Pc) derivatives, such as H_2Pc[124,125] and ZnPc.[126–129] Note that the activation energy is lower than the HOMO-LUMO gap of compound **1**, which means the presence of impurities and/or a tail state of energy

band dispersion.

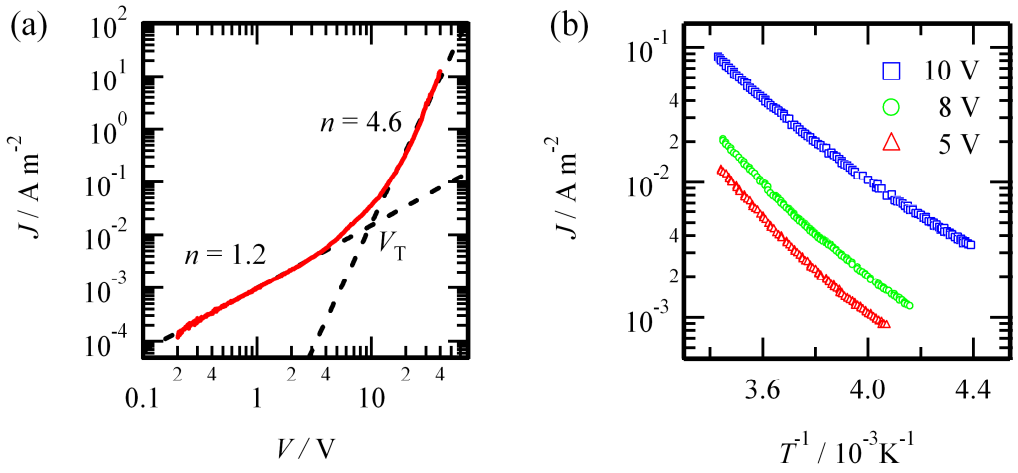

Figure 2-17. (a) *J-V* curve at room temperature, and (b) temperature dependence of the conductivity for a thin film of **1** under a vacuum in dark.

2-3-4-2. Thin-Film Transistor with SiO_2 gate-dielectrics

Figure 2-18(a) shows the transfer characteristics of OTFT of **1** (20 nm) under a vacuum in dark at room temperature. The OTFT operates as a normal off transistor with an on-off current ratio of 10^4, reflecting the low conductivity and wide band gap. The threshold voltages are obtained as V_T = −21 V, and are dramatically improved compared to those of the devices reported by Perepichka *et al.* (V_T = −45 V).[25] Although Pt-electrodes have a large work function (~ 5 eV), the short length between the source and drain electrode (2 μm) would enhance the carrier injection from gate-dielectrics to the organic semiconductive layer.

The field-effect mobility μ is estimated from the transfer characteristics by employing the standard formula for the linear regime,[26,45]

$$\mu = \left(\frac{\partial I_D}{\partial V_G} \right) \frac{L}{wCV_D}, \tag{2-3}$$

where L and w are the size parameters of the electrodes, and C is the capacitance of the gate-dielectrics (~10^{-8} F cm^{-2}). The obtained hole mobility is about 2 × 10^{-5} cm^2 V^{-1} s^{-1}, which is lower than the value of Perepichkas' devices (9 × 10^{-3} cm^2 V^{-1} s^{-1}).[25] The lower mobility should originate from the low applied source-drain voltage V_D of −10 V and source-gate voltage of V_G = −60 V, while Perepichkas' devices have a applied high voltage of V_D = −70 V and V_G = −70 V. It is generally interpreted that the shallow impurity level would be filled by a high applied electric-field, and a high mobility can be obtained.[130–133] Figure 2-18(b) shows the output characteristics of OTFT of **1**, which indicates that the carrier injection is done effectively.

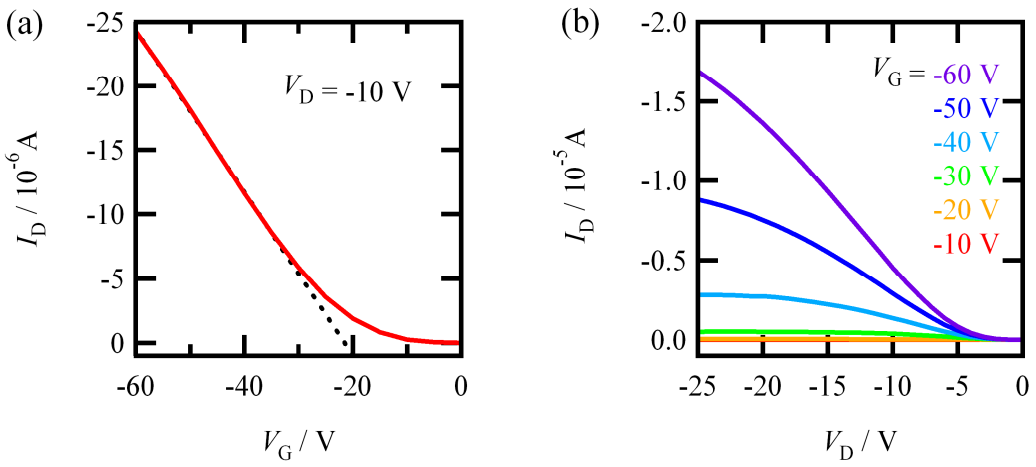

Figure 2-18. Transfer (a) and output (b) characteristics of TFTs of **1** with SiO_2 gate-dielectrics.

Figure 2-19(a) shows the temperature-dependent hole mobility μ calculated from transfer characteristics at various temperatures. The mobilities are decreased with decreasing temperature, suggesting the trapping transport mechanism.[134–136] Figure 2-19(b) shows the gate-dependent activation-energy with the drain voltage of −5 V and −10 V. The activation energy of OTFT mobility E_{FE} is calculated by

$$\mu = \mu_0 \exp\left(\frac{-E_{FE}}{k_B T}\right), \tag{2-4}$$

where μ_0 is a coefficient. The hole doping from gate-dielectrics could moderate the activation energy of thin film, which indicates that the effective carrier concentration and energy level alignment can be achieved by the TFTs structure.

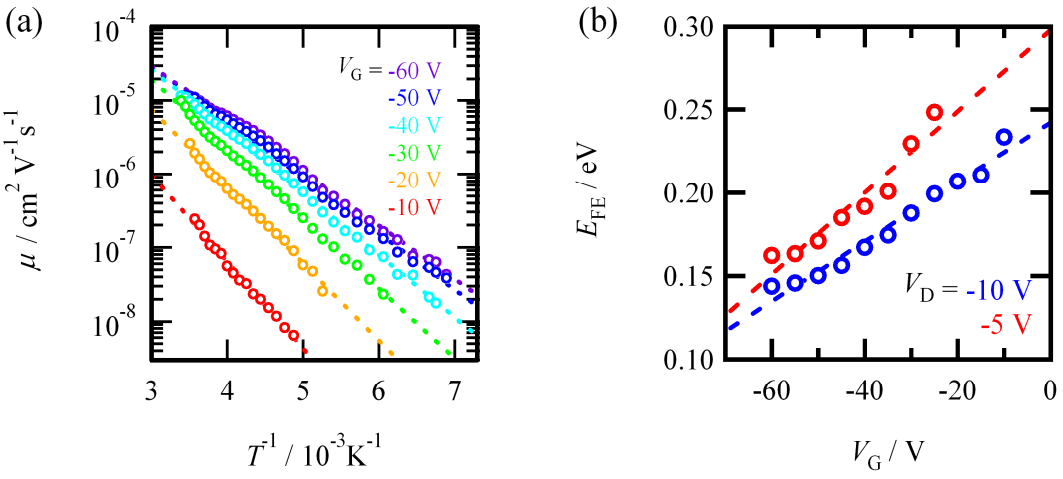

Figure 2-19. (a) Temperature dependence of the field-effect mobility of **1**. (b) The activation energies *vs.* the gate voltage calculated from Figure 2-19(a).

2-3-5. Iodine and TCNQ Doping to the Thin Film

In the previous section, the solid-state electric properties for the neutral state of a thin film of **1** were revealed. To reveal the electronic structure at the charged state and the potential for electronic application, carrier doping is an effective method. The acceptor doping is effective for the compound **1** because of its donor nature. Although the compound **1** is insoluble in various organic solvents, the closed packing with strong sulfur-sulfur contacts allowed vapor doping to the thin films.

2-3-5-1. Iodine doping

The iodine doping to the thin film of **1** was carried out under iodine vapor by the two-probe method. Figure 2-20 depicts the time dependence of the conductivity. The conductivity is quickly enhanced by four orders of magnitude after doping, and shows saturation around 2000 s. This conductivity change is comparable to the on/off current ratio of OTFTs of **1**, which is described in section 2-3-4-2. It is clearly demonstrated that hole doping of **1** brought about significant enhancement of the conductivity. Note that the thin film of **1** is stable during the doping process.

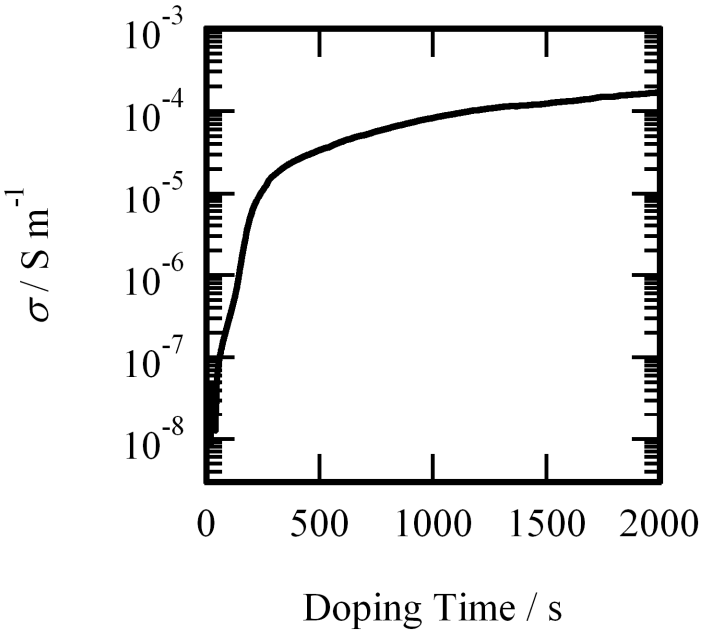

Figure 2-20. Time dependence of the conductivity during iodine doping for a thin film of **1**.

2-3-5-2. TCNQ doping and ambipolar TFTs operation

The strong acceptor molecule TCNQ was doped on the thin film of **1** (20 nm) by vacuum thermal evaporation. The film thickness of TCNQ is 50 nm. Figure 2-21 shows the *J-V* curve of this double-layer thin film. The conductivity calculated from the ohmic region is ~10^{-6} S m^{-1}. This result indicates that the effective carrier doping is achieved by the TCNQ molecule, though the degree of conductivity enhancement is lower then the field effect and iodine vapor doping.

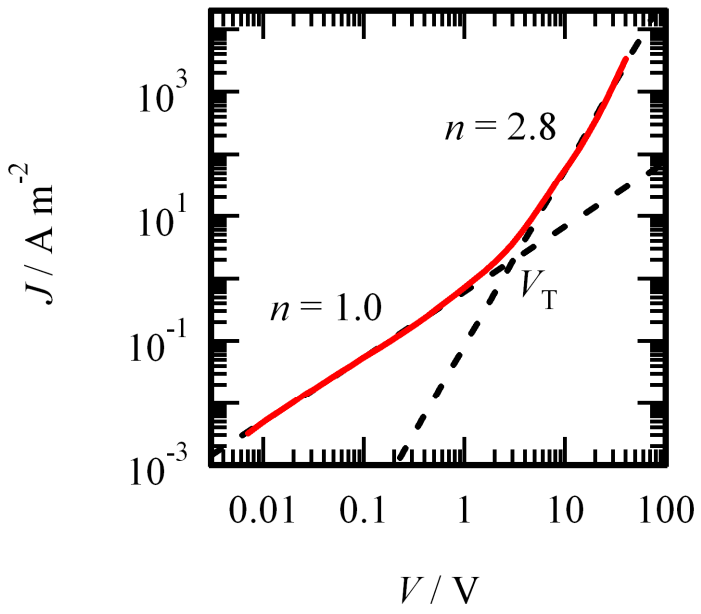

Figure 2-21. *J-V* curve at room temperature for the double-layer TFTs of **1** and TCNQ under a vacuum in dark.

The charge carrier injection by the field effect was demonstrated by means of double-layer thin films composed of **1** and TCNQ molecules with SiO_2 gate-dielectrics. The device configuration is shown in Figure 2-22. Figures 2-23(a) and 2-23(c) show the transfer characteristics of the double-layer OTFTs in the *p*- and *n*-type operation regions, respectively. Interestingly, these double-layer OTFTs show an ambipolar transport. The calculated field effect mobilities are about 10^{-5} cm^2 V^{-1} s^{-1} for the hole region, and 10^{-4} cm^2 V^{-1} s^{-1} for the electron region, respectively, while the on/off current ratios are less than 10^2 for both regions.

Figure 2-23 (b) and (d) show the output characteristic, namely, the source-drain current I_D versus voltage V_D plots, measured in the dark under a vacuum. There is little deviation from zero current with an increase in V_G, indicating that the current leakage through the dielectric is negligibly small.

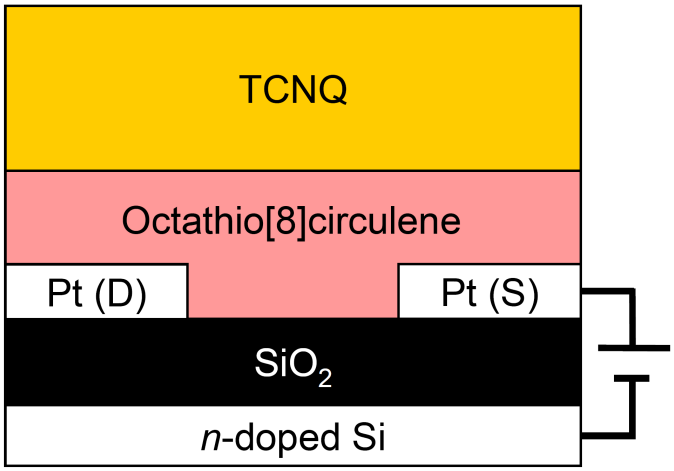

Figure 2-22. Device configuration of double-layer thin films composed of **1** and TCNQ molecules.

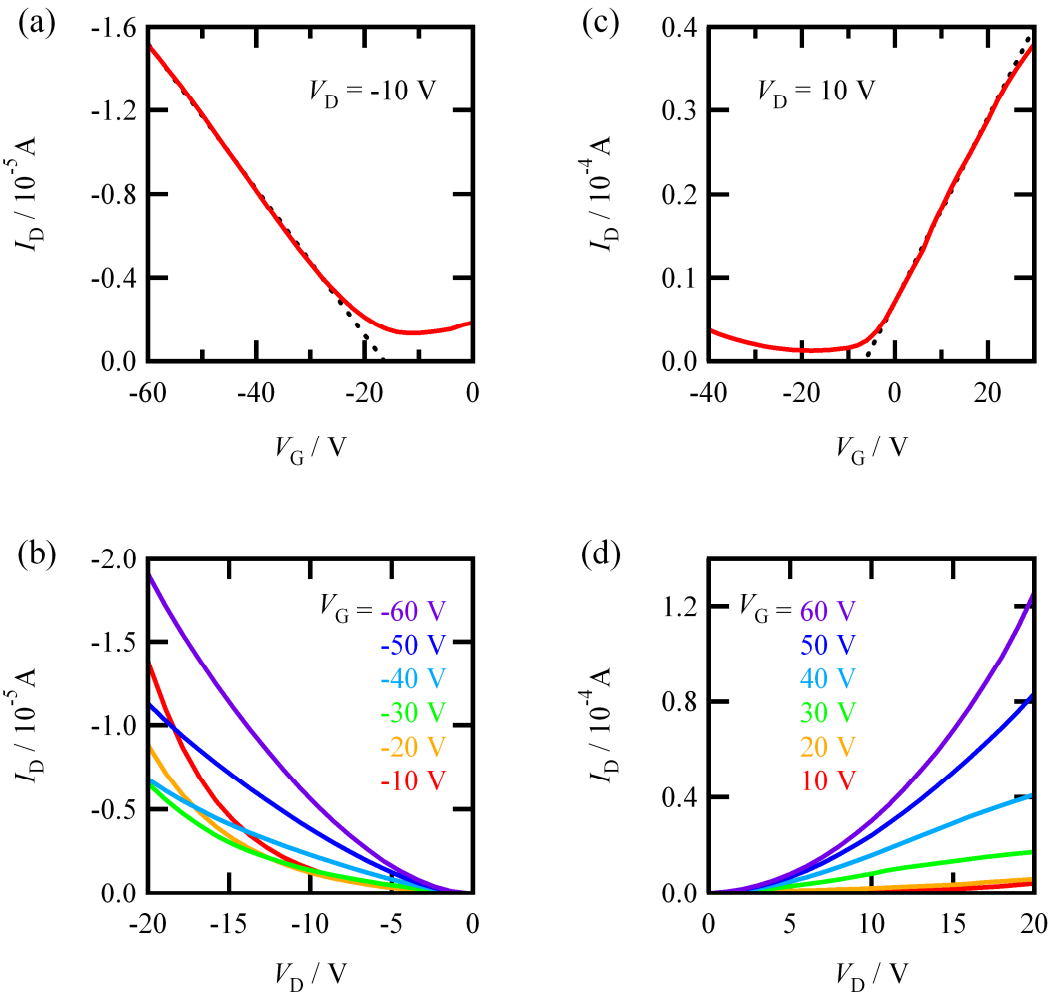

Figure 2-23. Transfer (panels (a) and (c)) and output (panels (b) and (d)) characteristics of the *p*- and *n*-type regions for the double-layer TFTs of **1** and TCNQ, respectively.

2-4. Conclusion

The molecular and crystal structures of **1** and **2** were accurately determined by X-ray single-crystal analysis. In contrast to the significant tub-shape distortion in **2**, the molecule **1** has a very planar structure, in which the structural distortion caused by the 8π antiaromaticity is released.

Crystalline thin films of **1** were obtained by vacuum vapor deposition, and thin-film XRD indicated a lamellar structure in which the molecular planes were nearly perpendicular to the substrates. The redox process of **1** with significant electrochromism was revealed by the electrochemistry of the thin films of **1** in an ionic liquid. This color change, well-interpreted in terms of the allowed n-π transition by electrochemical oxidation, was good experimental evidence for the nearly degenerated HOMOs in **1**. This method would be applicable to various insoluble materials with strong self-assembling forces.

The temperature-dependent conductivity measurement for the thin films of **1** revealed a large activation energy which reflected the semiconductive character of **1**. This activation energy was modulated by the FET structure. A chemical doping effect on the thin film of **1** was also demonstrated, and the significant conductivity change was confirmed. Interestingly, the TCNQ doped thin film exhibited an ambipolar OTFT performance.

Compound **1** with orbital degeneracy and a 3D crystal structure has a high potential to yield unusual electronic and/or magnetic properties, and a great capacity for application to organic electronic devices.

Chapter 3

Electric-Double-Layer Transistors of Octathio[8]circulene with Ionic Liquids

3-1. Introduction

The EDL-OTFT techniques have been widely applied to various materials, such as metal,[137,138] inorganic[68–73] and polymer compounds,[74,139–141] since high-density carrier accumulation can be realized through the EDLs formed at the interface between the active layer and the gate electrolytes. While this technique has not yet been applied to organic thin films, due to their solubility in ionic liquids, the persistence of the thin films of **1** allowed performance of the present experiments.

In addition to the demonstration of EDL-OTFTs below oxidation potential, the crossover between EDL-formation (electrostatic) and the electrochemical oxidation process has remained to be clarified. Figure 3-1 schematically shows the electrostatic and electrochemical carrier injection into a thin film of planar organic molecules in an ionic-liquid electrolyte. In this figure, the molecular planes are assumed to be nearly perpendicular to the substrate, as can be seen in the thin-film structures for most aromatic organic molecules.[103,104] At zero bias voltage (V = 0 V), there is no interaction between the counter ions and the thin film. When a voltage of V_1 (>0 V) is applied, the anions concentrate at the surface of the thin film and effectively induce an electrostatic carrier injection at the interface through the formation of an EDL. Once a higher voltage of V_2 ($V_1 < V_2$) is applied, however, electrochemical doping takes place; the

anions penetrate into the thin film and produce carriers in the whole thin film. This process is associated with irreversible penetration of the counter anions, and spoils the transistor performance.

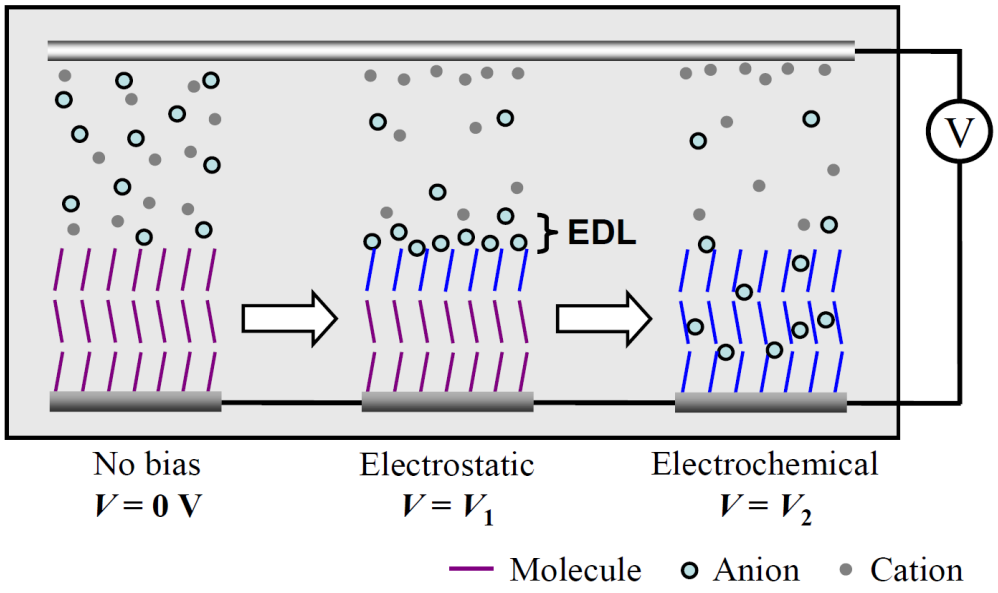

Figure 3-1. Electrostatic and electrochemical carrier injection into a thin film of organic molecules.

Generally, organic compounds have been thought to exhibit unipolar transport properties, while some organic materials having a small HOMO-LUMO gap show ambipolar behavior in OTFTs without specific treatment. The EDL-OTFT technique is convenient for charge carrier injection from gate-dielectrics to a semiconductive layer by lower applied voltage, while solid gate-dielectric OTFTs require a higher voltage than EDL-OTFTs due to their low carrier accumulation. This electrochemical method

of EDL-OTFTs is suitable for ambipolar operation for organic compounds including wide HOMO-LUMO gap materials.

In section 2-3-2, it was confirmed that the thin film of **1** is stable in ionic liquids during the oxidation/rereduction process. In this chapter, the technique of ionic liquid EDL-OTFTs was applied to the thin films of **1**. The relation between the OTFT gate voltage and the electrochemical oxidation/reduction potential of **1** was discussed; this relation has never been discussed for any previous EDL-OTFTs. The crossover between electrostatic and electrochemical doping and to what extent the nature of the ionic liquid governs the transistor performance and the carrier injection were also elucidated using six kinds of ionic liquids.

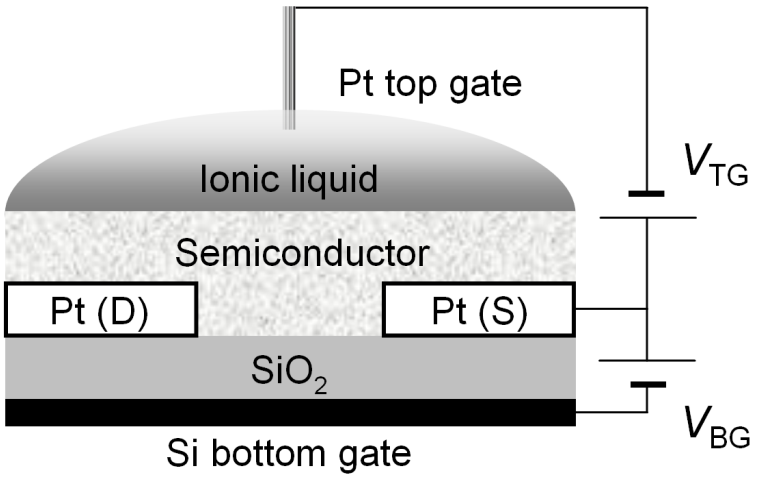

Figure 3-2. Dual-gate EDL-OTFT, consisting of the thin film of **1** and an ionic liquid **IL1**.

Dual-gate OTFT with SiO_2 and ionic liquid gate-dielectrics were also demonstrated, as shown in Figure 3-2. These transistors have been developed in addition to the

conventional single-gate structure. There are advantageous, as independent control of the two gate biases can optimize the device performance, and each bias voltage can be very low.[142] While this operation mechanism is promising for improving the performance of OTFTs and for elucidating the charge accumulation and the carrier transport within them, its application to organic transistors has been very limited.[143,144] Although dual-gate OTFTs with solid-state gate-dielectrics have been reported previously, the combination of the ionic liquid- and SiO_2-gate dielectrics will result in very good transistor performance, because the SiO_2-gate voltage can maintain the operation voltage at the ionic liquid gate at a sufficiently low level to avoid surface damage.

Ambipolar EDL-OTFTs of **1** thin film were demonstrated by using BMIM-BF_4 (**IL4**), which is an ionic-liquid that has a large electrochemical window and is electrochemically stable. While the compound **1** has a large HOMO-LUMO gap (~5 eV, see section 2-3-2), so that it cannot easily achieve ambipolar operation with solid gate-dielectrics, the reversible ambipolar EDL-OTFT behavior was observed without decomposition of **1**.

3-2. Experimental

The ionic liquids, DEME-TFSI (**IL1**), DEME-BF_4, (**IL2**), BMIM-TFSI (**IL3**), BMIM-BF_4 (**IL4**), BMIM-OTf (**IL5**), and BMIM-PF_6 (**IL6**), were purchased from Kanto Reagents and used without further purification.

The capacitances C_{IL} of these ionic liquids were measured using a sandwich structure, consisting of two Al films and a layer of ionic liquid in between. The frequency dependence of the capacitance was measured using an NF ZM2371 LCR meter in the range of 0.1 Hz–100 kHz with AC voltage amplitude of 50 mV.

The coupled electrochemical measurements, which include cyclic voltammetry (CV) and in-situ EDL-OTFT performance testing, were carried out at room temperature in ionic-liquid electrolytes. Thin-films of **1** with a thickness of 50 nm were prepared by vacuum vapor-deposition on interdigitated array electrodes (Pt), in which the channel dimensions correspond to w = 100 cm width and L = 2 μm length. The measurements were done using a three-electrode system, consisting of the working, counter, and reference electrodes. A platinum wire was used as a counter electrode and an Ag/AgCl electrode as a reference electrode, which were immersed in the ionic-liquid electrolyte (see Figure 3-3). Electrochemical measurements were performed on a Hokuto HAB-151 electrochemical analyzer and NF Li-5640 digital lock-in amplifier. The EDL-OTFT performance was examined by the alternating current method for the source-drain current measurements to avoid a capacitance effect induced by a direct current voltage between the source and the drain electrodes.

In-situ UV/vis/NIR absorption measurements were carried out using an ALS420 electrochemical analyzer and an Ocean Optics HR4000CG-UV-NIR spectrometer, in

the photon energy range 1.6–2.6 eV for the thin films (500 nm) of **1** on the ITO substrates.

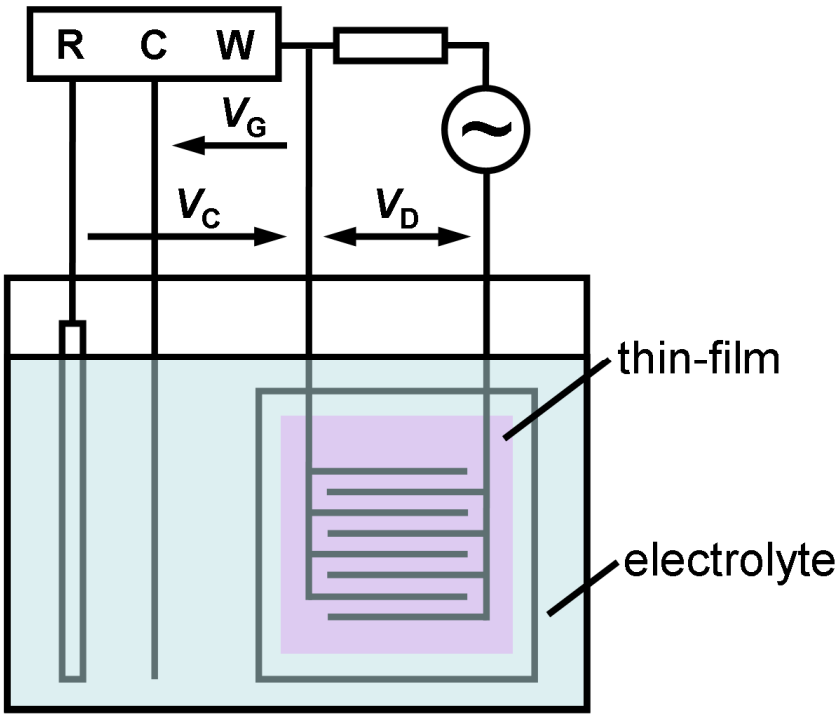

Figure 3-3. (a) A schematic illustration of the EDL-OTFT, consisting of a thin film deposited on interdigitated array electrodes (Pt) and an electrolyte of ionic liquid.

Figure 3-2 illustrates the structure of the dual-gate EDL-OTFT of **1**. The thin films of **1** with a thickness of 30 nm were prepared by vacuum vapor-deposition on the interdigitated array electrodes (Pt), in which the channel dimensions were w = 100 cm in width and L = 2 μm in length, and which were separated from the bottom-gate electrode (n-doped Si) by a SiO_2 layer of 300 nm. The top-gate was prepared with a

droplet of **IL1** that covered the whole area of the thin film, and a Pt wire that was inserted into the ionic liquid. Dual-gate OTFT performance tests were carried out by using an ADVANTEST R6246 dual-channel source meter at room temperature under dark and vacuum conditions in **IL1** electrolytes.

The ambipolar EDL-OTFTs measurements were carried out the same configuration with dual-gate EDL-OTFT as shown in Figure 3-2 with the bottom-gate circuit being open. The thin films of **1** with a thickness of 30 nm were prepared by vacuum vapor-deposition on the interdigitated array electrodes (Pt), in which the channel dimensions were w = 100 cm in width and L = 2 μm in length. The top-gate was prepared with a droplet of **IL4** that covered the whole area of the thin film, and a Pt coil that was inserted into the ionic liquid. EDL-OTFT performance tests were carried out by using Keithley 2636 system at room temperature under dark and vacuum conditions.

3-3. Results and Discussion

3-3-1. Electric-Double-Layer Formation

To confirm the formation of EDLs at the interface between the ionic liquids and the electrodes, the frequency dependence of the capacitance C_{IL} was examined for **IL1**–**IL6**, in the range from 10^{-1} to 10^{5} Hz. The results are shown in Figure 3-4(a), where the frequency is plotted in a logarithmic scale. In the low frequency range, below 10^{2} Hz, the C_{IL} values are very large, being of the order of 10^{-6} F cm^{-2}, and differ from each other, suggesting significant ionic liquid dependence. The values of C_{IL} at 10^{-1} Hz are compared in Table 3-1. However, C_{IL} values of **IL1**–**IL6** commonly show a quick decrease above 10^{2} Hz, with much less significant ionic liquid dependence. Figure 3-4(b) shows the loss coefficient (tan δ) for **IL1**–**IL6**. The values of tan δ are consistently small below 10^{2} Hz, but they show a quick increase above this frequency. The values of tan δ can be expressed by the following equation,

$$\tan\delta = \frac{I_R}{I_C} = \frac{1}{\omega C_{IL} R_P}, \qquad (3\text{-}1)$$

where I_C and I_R are the currents of C_{IL} and the parasitic resistance (R_P), respectively, and ω is the angular frequency. Since the values of R_P exhibit a linear dependence on frequency (see Figure 3-4(c)), the significant increase in tan δ above 10^{2} Hz should be caused by the decrease in C_{IL} shown in Figure 3-4(a).

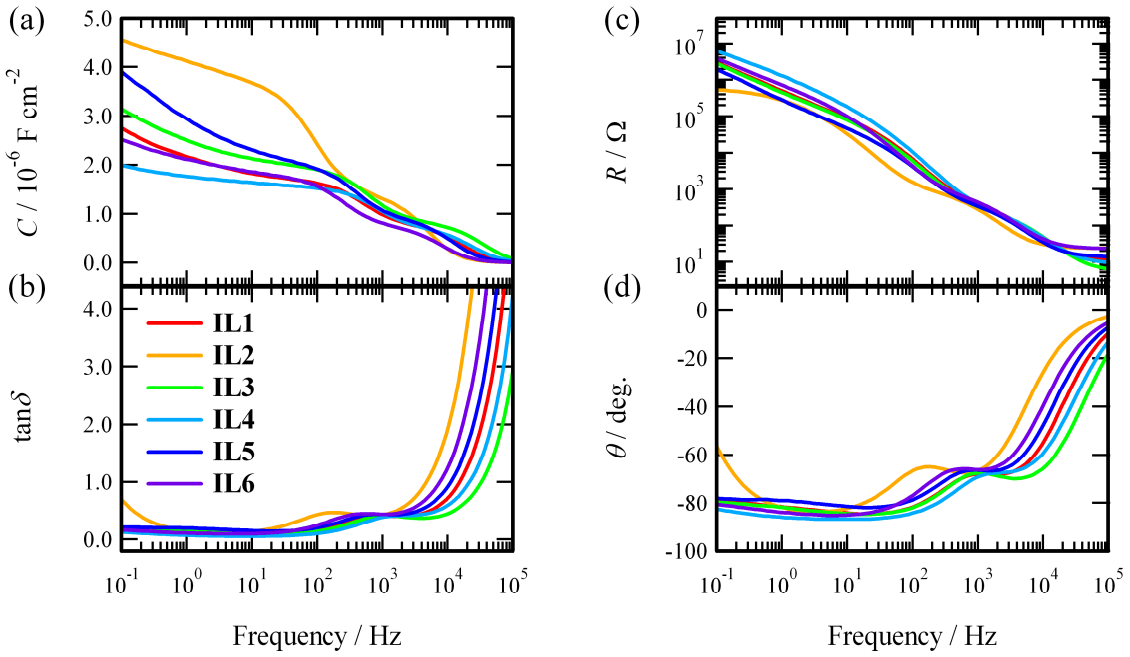

Figure 3-4. Capacitance (a), tan δ (b), resistance (c), and θ (d) of the ionic liquids **IL1-IL6** as a function of frequency.

The dependence of C_{IL} and tan δ on the ionic liquid clearly indicates the formation of effective EDLs in **IL1–IL6** at the low frequencies. In addition, the decrease in C_{IL} and increase in tan δ at high frequencies suggests that the EDLs are formed by a spatial arrangement of the component cations and anions in the ionic liquids at the electrode interfaces, and the deformation cannot follow high-frequency field alternation. In the frequency range where the EDL formation is expected, the capacitances are of the order of 10^{-6} F cm^{-2}, which can lead to a high carrier density of ~10^{15} cm^{-2}. This is much larger than those of usual solid-state gate-dielectrics; their typical capacitances are of the order of ~10^{-7} F cm^{-2}, and the induced carrier density is ~10^{13} cm^{-2}.

It is worth noting the material dependence of C_{IL} for the ionic liquids, **IL1**–**IL6**, which have been confirmed with good reproducibility. It is clear that they are not governed by the constituent components, namely, cation or anion. For example, the ionic liquids, **IL1** and **IL2**, commonly include the DEME cation, but their C_{IL} values are significantly different. It is hard to rationalize this material dependence because the capacitance of an ionic liquid is probably governed by various factors, such as volume, shape, and polarizability of the component ions and the interactions between them.

3-3-2. Electric-Double-Layer Transistor

Figure 3-5(a) shows the CV curves of a thin film (500 nm) of **1** in **IL1** discussed in section 2-3-3, where V_C is the electrode potential versus the reference electrode (see also Figure 3-3). The difference between V_G and $-V_C$ should be smaller than the width of the electrochemical window of **IL1** (~4 V). The first cycle (red curve) shows an oxidation peak above V_C = 1.2 V, while the second cycle (black curve) and later cycles show a two-electron oxidation peak at 1.12 V (*vs.* Ag/AgCl) and step-wise re-reduction peaks at 0.90 and 0.75 V with good reproducibility. It is notable that the thin films of **1** often exhibit exfoliation in the range of V_C >1.2 V, probably due to penetration of the thin films by counter cations.

The *n* value was calculated to be 0.015, using the oxidation peak in the second cycle. This small value means that the electrochemical redox process occurs only at the surface of the thin film; the thickness of the redox layer is estimated to be ~10 nm.

The OTFT performance was examined in the V_C range between 0.0 and 1.1 V on the samples that had not experienced the over-potential effects. Therefore, the gate leakage current through the electrolytes is very small (<0.2 μA) and agrees well with the CV current of the first cycle (red curve in Figure 3-3(a)). This current is much smaller than the source-drain current I_D, as long as V_C is maintained as V_C <1.1 V.

Figure 3-5(b) shows the transfer characteristics of the EDL-OTFT of **1** with a scanning rate of 10 mV s^{-1} at various source-drain voltages V_D. The I_D curves show significant increases below the threshold V_C of 0.5 V, indicating an OTFT performance. This threshold value of $-V_C$ is much lower than the threshold V_G of the SiO_2-gate OTFT of **1** and is nearly half of the onset potential of the oxidation peak on the

repeatable CV curve (black curve in Fig. Figure 3-5(a)). Since the penetration of the counter cations into the thin films is believed to start at the electrochemical onset potential, the difference between the threshold V_C and the onset potential represents an effective carrier generation by the formation of EDLs on the surfaces of the thin films.

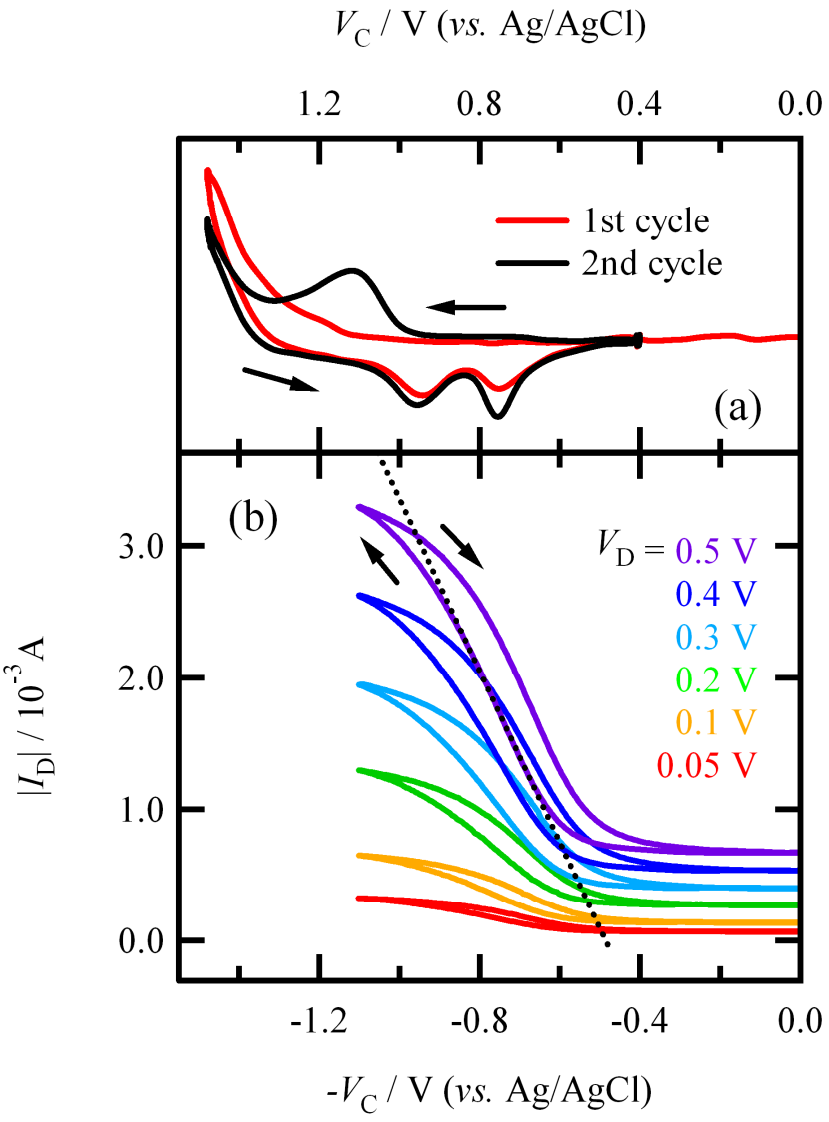

Figure 3-5. (a) CV curve of a thin film of **1** with **IL1** (from section 2-3-3). (b) Transfer characteristics of the thin-film EDL-OTFT of **1** with **IL1**. The dotted line represent the theoretical line of Eq. (3-2), fitted to the forward scan of V_D = 0.5 V.

There are noticeable hystereses between the forward and reverse scans in Figure 3-5(b). In addition to the possible causes of the hysteresis loops in solid-state gate-dielectrics transistors, such as charge trapping in the dielectrics and defects in the semiconductors,[145–149] the loops in the present OTFTs are probably due to a slow polarization change of the ionic liquid that is limited by the diffusion time of the ionic molecules in the liquid. The I_D values at V_C = 0.0 V after the cycles agree well with the initial ones, suggesting stableness of the thin films in the V_C range between 0.0 and 1.1 V.

The hole mobility μ in the linear region is evaluated by,

$$\mu = \left(\frac{\partial I_D}{\partial V_C} \right) \frac{L}{w C_{IL} V_D}, \tag{3-2}$$

where L and w are the size parameters of the electrodes, and C_{IL} is the capacitance of the ionic liquid (2.7 μF cm^{-2}, see section 3-3-1). The dotted line in Figure 3-5(b) represents the theoretical characteristics of Eq. (3-2) fitted to the forward scan of V_D = 0.5 V. The value of μ is calculated as $\mu \approx 1.0 \times 10^{-2}$ cm^2 V^{-1} s^{-1}. Since these values are comparable to those of the SiO_2-gate OFET of **1**, it is concluded that the ionic liquid can provide efficient coupling to the thin films of **1** without sacrificing carrier mobility at the solid/liquid interface.

Figure 3-6 shows the resistance R of the EDL-OTFT of **1** against V_C, which is obtained from the data of V_D = 0.5 in Figure 3-5(b). The dependence of R from the other V_D values are nearly the same as that in Figure 3-6. The values of R show a decrease by one order of magnitude below V_C = 0.5 V. In this measurement, alternate current on protective resistance were recorded and translated into I_D values, which is limited to gain the large on/off current ratio because of their balanced relation between

resistance and thin film.

The carrier density N at V_C = 1.1 V is roughly estimated to be 1.3 × 10^{13} cm^{-2}, using,

$$N = \frac{1}{e\mu\rho}, \tag{3-3}$$

where ρ is the resistivity. This value is much higher than that of the SiO_2-gate OTFT of **1** (1.5 × 10^{12} cm^{-2} at V_G = −60 V, see section 2-3-4-2). It is thus concluded that EDL-OTFTs can produce much higher carrier densities than solid state OTFTs.

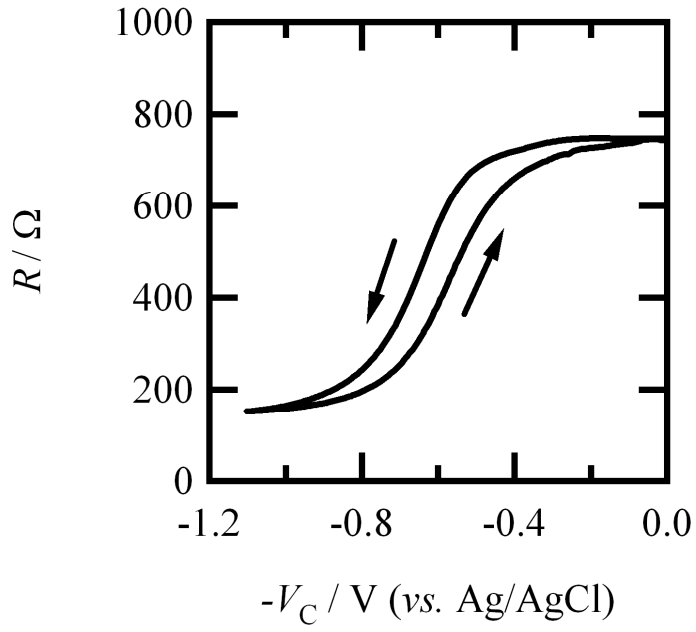

Figure 3-6. Resistance R of the EDL-OTFT of **1** with **IL1** against V_C. Arrows indicate the scan directions.

Figure 3-7 depicts the output characteristics at V_C = 0.4–1.0 V, showing a linear relation between I_D and V_D. It is clear that a large current of mA range can be generated with small V_C and V_D (<1 V), indicating a very low-power operation of OTFT caused by the high-density carrier accumulation at the ionic-liquid/thin-film interface.

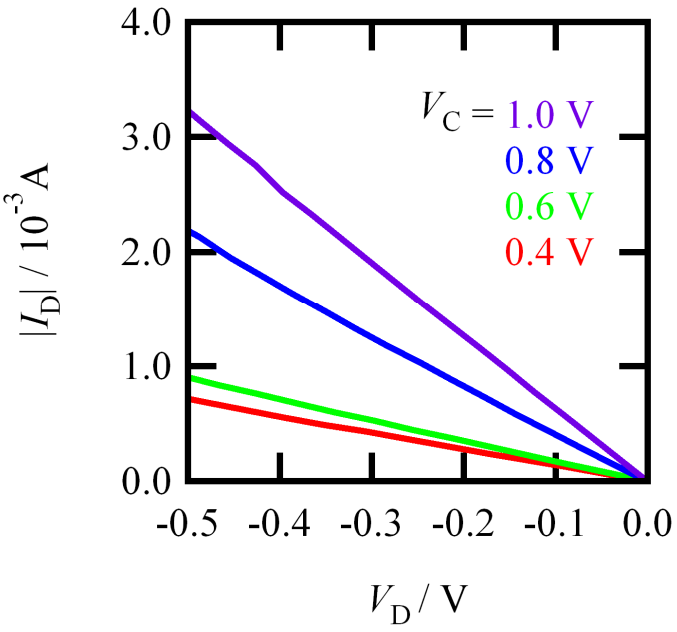

Figure 3-7. Output characteristics of the EDL-OTFT of **1** with **IL1** at V_C = 0.4–1.0 V.

3-3-3. Component Dependence of Carrier Injection and Mobility

In the previous section, electrochemistry and the EDL-OTFT performance of **1** thin film in an ionic liquid **IL1**, was studied. In this section, these processes were reexamined, using six kinds of ionic liquids, and elucidated the crossover between electrostatic and electrochemical doping and to what extent the nature of the ionic liquid governs the transistor performance and the carrier injection.

The measurements shown in the previous sections were carried out under air condition, because **IL1** was hydrophobic. In this section, however, the electrochemical measurements, namely the cyclic voltammetry (CV) and the in-situ EDL-OTFT performance test, were carried out under vacuum, since three ionic liquids, **IL2**, **IL4**, and **IL5,** have a hydrophilic character and they are air sensitive.

Table 3-1. Comparison of the ionic liquids, **IL1**–**IL6**; components, capacitance C_{IL} at 0.1 Hz, mobility μ, transistor threshold voltage V_T, and oxidation peak voltage V_{OX} for the EDL-OTFTs of **1**.

Ionic liquid	Components		EDL-OTFT performance			CV
	Cation	Anion	C_{IL} at 0.1 Hz	μ / cm^2 V^{-1} s^{-1}	V_T / V	V_{OX} / V
IL1	DEME	TFSI	2.7×10^{-6}	6.3×10^{-3}	0.89	1.42
IL2	DEME	BF_4	4.6×10^{-6}	1.7×10^{-3}	1.01	1.54
IL3	BMIM	TFSI	3.1×10^{-6}	6.6×10^{-3}	0.85	1.46
IL4	BMIM	BF_4	2.0×10^{-6}	1.9×10^{-2}	1.04	1.50
IL5	BMIM	OTf	3.9×10^{-6}	2.9×10^{-3}	0.79	1.32
IL6	BMIM	PF_6	2.5×10^{-6}	7.8×10^{-3}	1.11	1.64

3-3-3-1. Electrostatic Carrier Injection

The EDL-OTFT performance of the thin films of **1** was examined in a vacuum condition, using the ionic liquids, **IL1–IL6**, as gate-dielectric materials. Figures 3-8(a)-(f) show the transfer characteristics of the EDL-OTFTs at a source-drain voltage V_D of 0.5 V and at a scanning rate of 0.01 V s^{-1}. The gate leakage current through the electrolyte was much smaller than the source-drain current $|I_D|$. The EDL-OTFTs' behavior are essentially the same, but the values of V_T depend on the ionic liquids significantly, as is listed in Table 3-1.

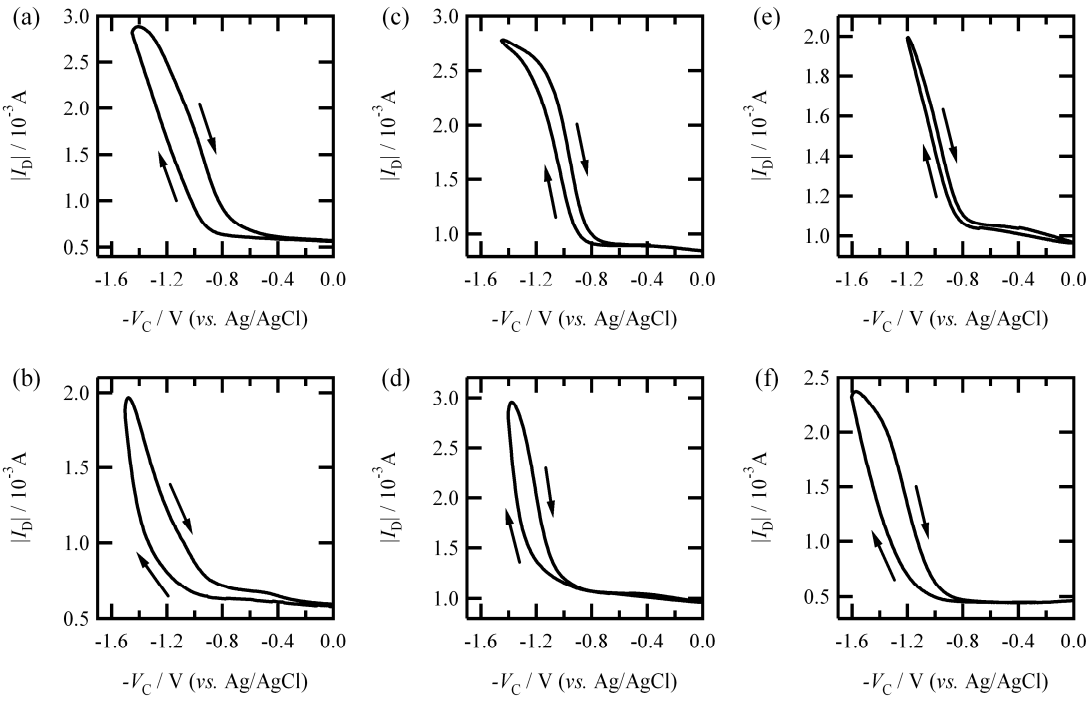

Figure 3-8. Transfer characteristics of the EDL-OTFTs of **1** with the ionic liquids **IL1** (a), **IL2** (b), **IL3** (c), **IL4** (d), **IL5** (e), and **IL6** (f). The source-drain voltage V_D is 0.5 V.

The EDL-OTFTs performance, which is stable over many cycles, clearly indicates that compound **1** operates as a *p*-type semiconductor. The resistance at V_C = 0.0 V is R_0 = 950 Ω for EDL-OTFTs in **IL1** (see Figure 3-8(a)), and there is no change, even after 30 cycles. This indicates a high stability of the thin films of **1** in the V_C range for EDL-OTFT operation. As described later, however, once the thin films experience a voltage greater than about 1.5 V, electrochemical oxidation takes place, with an irreversible penetration of the counterions.[150–154]

The hole mobilities μ for the EDL-OTFTs of **IL1**–**IL6** were calculated from the transfer characteristics in Figures 3-8(a)–3-8(f) for the linear regime of the forward scan. The results are listed in Table 3-1. Figure 3-9 shows the log-log plots between μ and C_{IL} at 0.1 Hz. There is a characteristic negative linear relationship between them, with a gradient of −2.7 (dotted line in Figure 3-9). Such behavior has been reported in refs. [155–157] and has been interpreted as being due to a dipolar disorder in the gate-dielectrics, which induces a broadening of the density of states (DOS) at the semiconductor/dielectric interface, and a decrease in the DOS at the Fermi energy. This was considered to reduce hopping probability and thus to suppress the carrier mobility.[155] Another possibility is that high-capacitance dielectric materials would reduce the effective electric field between the source and drain electrodes and would reduce the charge carrier mobility. In any case, Figure 3-9 indicates that the transistor mobility of EDL-OTFTs is regulated by the total capacitance of the ionic liquids.

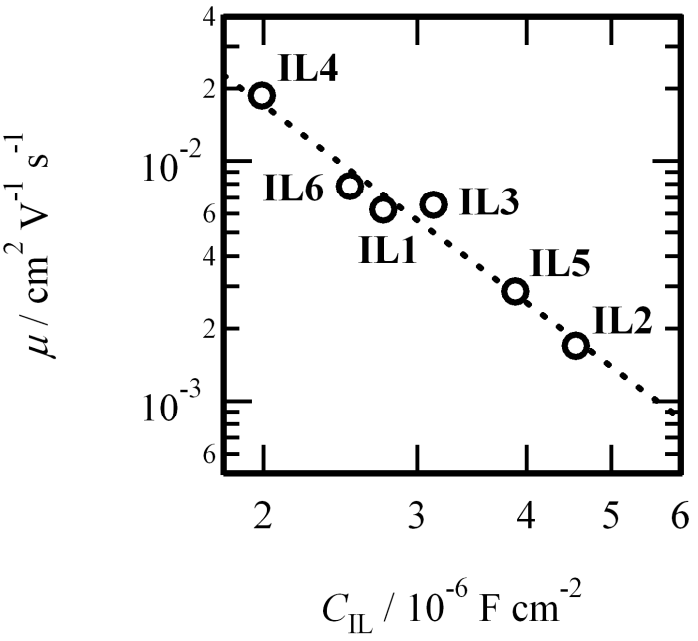

Figure 3-9. Log–log plots between μ and C_{IL} at 0.1 Hz for the EDL-OTFTs of **1** with the ionic-liquid gate-dielectrics, **IL1**–**IL6**.

3-3-3-2. Electrochemical Doping

As shown in the section 3-3-3-1, the EDL-OTFT performance with **IL1** is reproducible, and the R_0 value exhibits no change, against a gate voltage V_C scan in the range below 1.5 V. This indicates that the carrier accumulation occurs at the ionic liquid/semiconductor interface, without bulk oxidation of the thin films. In this section, in-situ electrochemical measurements by applying a voltage greater than 1.5 V were carried out. Figures 3-10(a) and 3-10(b) show the CV curve and the transfer characteristics, respectively, for the thin films of **1**, examined with **IL1** in the range of $0< V_C <1.7$ V. The CV curves show an oxidation peak at 1.4 V (*vs.* Ag/AgCl) in the forward scan and stepwise re-reduction peaks at 1.25 and 1.10 V in the backward scan, especially in the second cycle and beyond. It is clearly seen that $|I_G|$ values show a gradual increase with the cycles. This means that the redox active range (depth) in the thin film is increased in a stepwise manner by repeating the cycles.

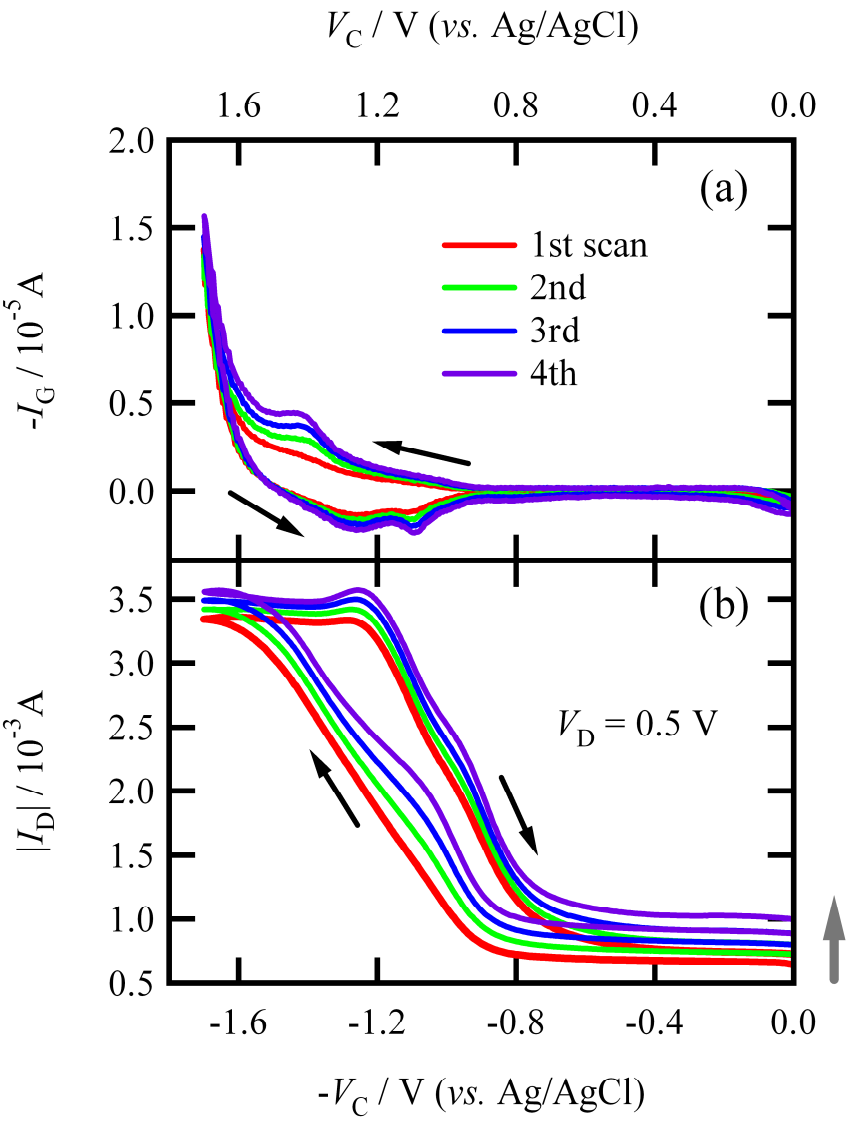

Figure 3-10. CV curve (a) and transfer characteristics (b) of a thin film of **1** with **IL1** gate-dielectrics, respectively. The outline arrow indicates the oxidation peak voltage (V_{OX}). Gray arrow indicates the change of $|I_D|$ at V_C = 0 V.

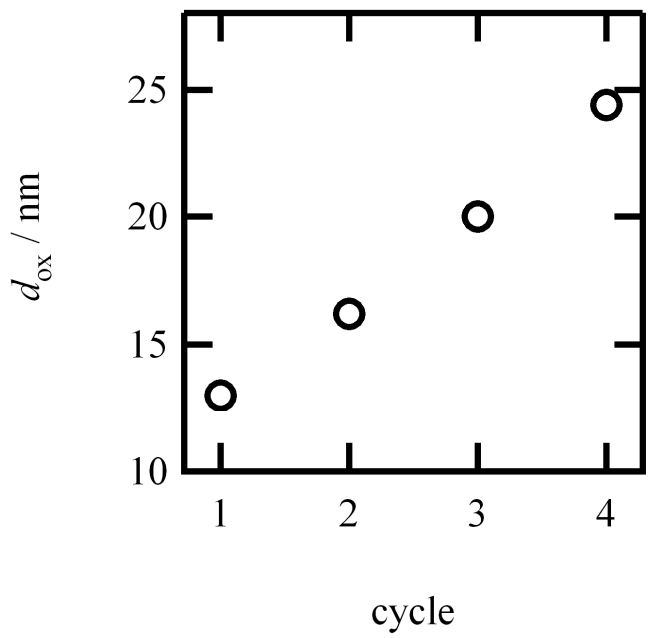

Figure 3-11. Cycle dependence of the thickness (d_{OX}) of the oxidized layer for the thin film of **1** in **IL1**.

The thickness (d_{OX}) of the oxidized layer was estimated from the CV curves, using

$$d_{OX} = \frac{QV_U}{nn'eA}, \tag{3-4}$$

where Q is the amount of charge calculated from the CV curve; V_U is the unit cell volume; n is the number of molecules in the unit cell; n' is the number of the reaction electrons per one molecule; e is the elementary charge; and A is the area of the thin film. The structure analysis and electrochemical study on **1** indicates that $n = 2$ and $n' = 2$, respectively, and the values of V_U and A are 711 Å^3 and 4 mm^2, respectively. Assuming that V_U was constant, the scan number dependence of d_{OX} was calculated.

The results are shown in Figure 3-11. The values of d_{OX} would approximately correspond to the penetration depth of the counter anion, namely, TFSI, because the molecular volume of the anion is much smaller than V_U. It is found that d_{OX} in the first scan is rather large (13 nm), but this is followed by a gradual, linear increase by 3–5 nm/scan after the second scan.

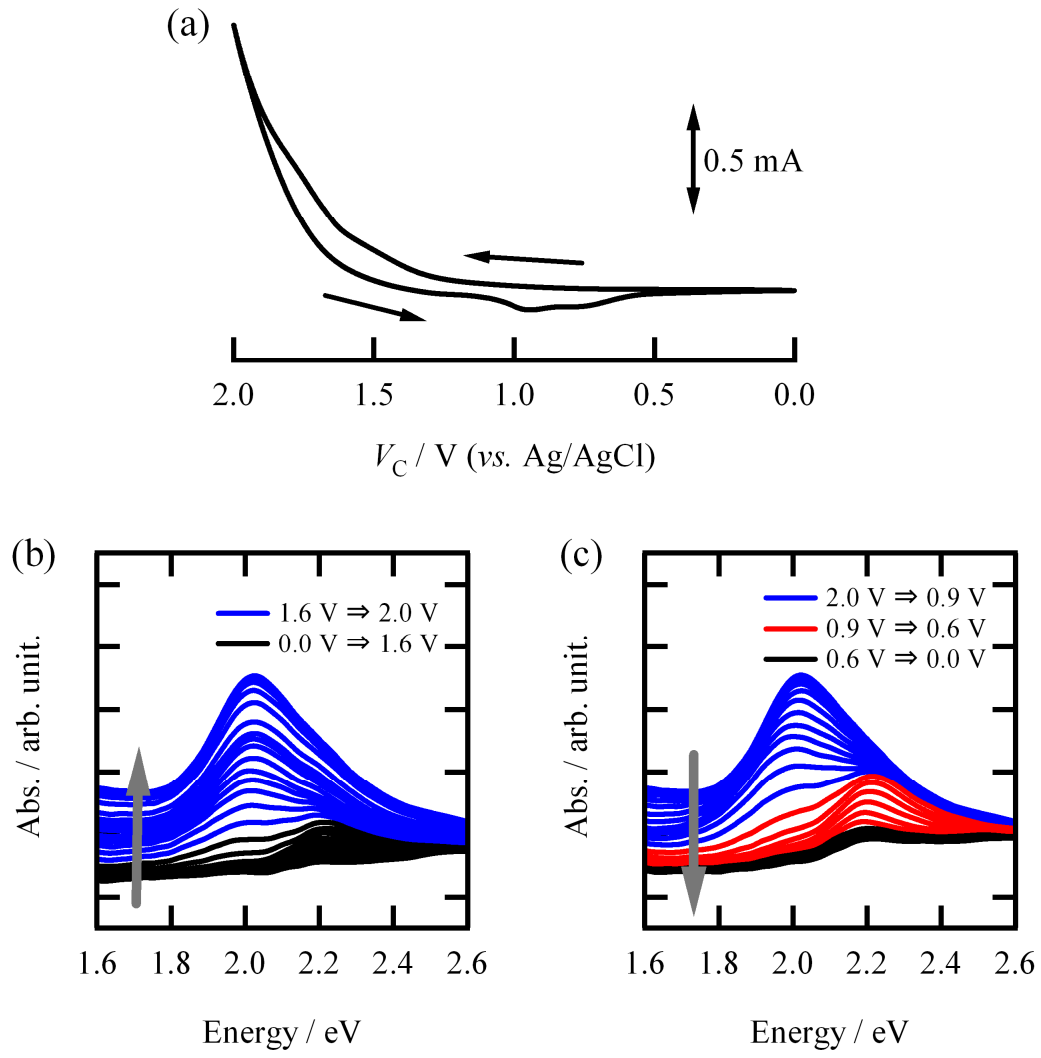

Figure 3-12. (a) CV curve of a thin film of **1** (500 nm) on ITO substrate in **IL1**, with a scanning rate of 10 mV s^{-1}. In-situ absorption spectra for the thin film of **1** in the oxidation (a) and the reduction (b) scans in the range of 0.0–2.0 V.

Figure 3-10(b) shows a gradual increase in $|I_D|$ at V_C = 0.0 V with the cycles, as indicated by the gray arrow. This is probably caused by trapped counter anions in the thin film, even at V_C = 0.0 V. To confirm the doping effects, in-situ UV/vis absorption measurements were carried out in the photon energy range 1.6–2.6 eV for a thin film (500 nm) of **1** on an ITO substrate. The results are shown in Figure 3-12. The absorption spectra indicate two peaks at hv = 2.07 and 2.21 eV in the oxidation process, which correspond to the triplet biradical and doublet monoradical species, respectively. The peak intensity at hv = 2.21 eV shows an increase even after dedoping (V_C = 0 V), with an increase upon cycling (see Figure 3-13). This is consistent with the presence of the residual anions in the thin films.

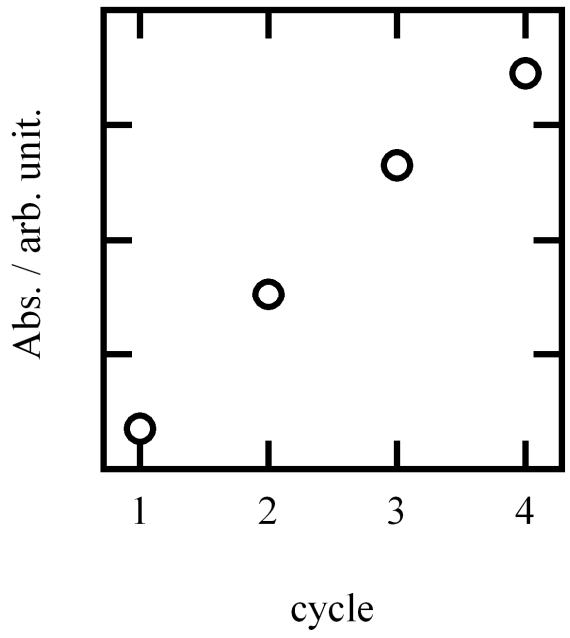

Figure 3-13. Absorbance intensity with hv = 2.21 eV at V_C = 0 V after cycling of thin film of **1** (500 nm) on ITO substrate in **IL1**.

The electrochemical oxidation processes of the thin films of **1** in the other ionic liquids, **IL2**–**IL6**, were also studied (see Figure 3-14). They are essentially the same as that in **IL1**, but interestingly, the oxidation potentials depend on the ionic liquids significantly. Table 3-1 shows a comparison of the oxidation potentials (V_{OX}) of **IL1**–**IL6**, that is defined as a CV-curve peak voltage in the forward scan.

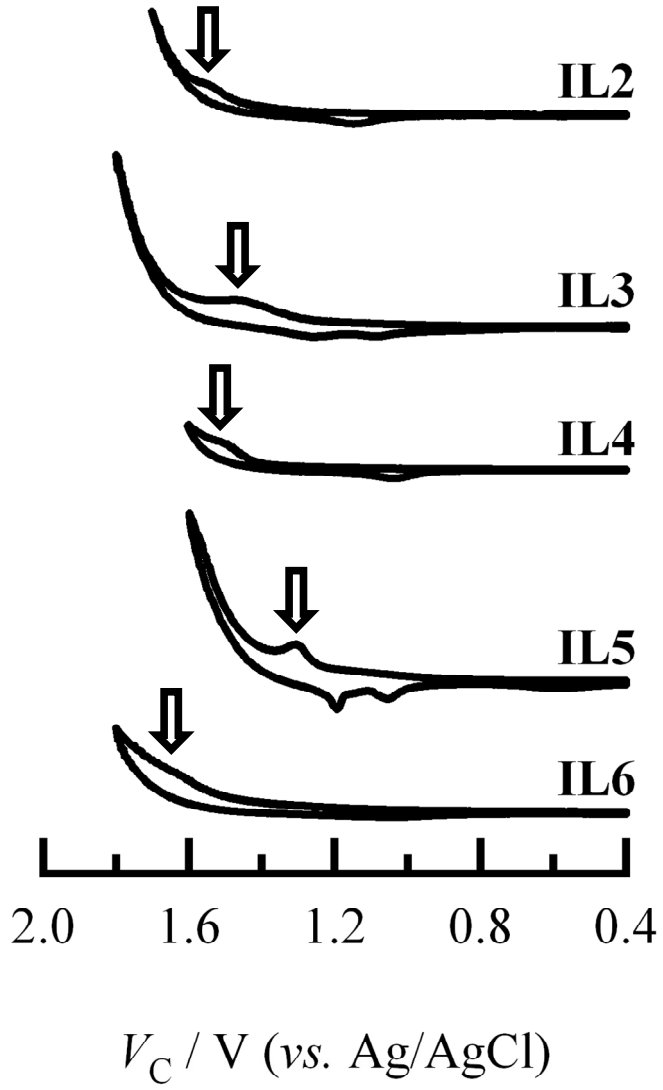

Figure 3-14. Electrochemical oxidation process of the thin films of **1** in ionic liquids, **IL2**–**IL6**. Outline arrows indicate the oxidation voltage (V_{OX}).

3-3-3-3. Anion Control of Carrier Injection

In the previous sections, it was revealed that the mobility of the EDL-OTFTs of the ionic liquids, **IL1**–**IL6**, was governed by their capacitance, and the values of V_T and V_{OX} depend on the ionic liquids. In this section, the controlling elements of the ionic liquids for V_T and V_{OX} will be discussed.

Figure 3-15 shows the relation between V_T and V_{OX} for **IL1**–**IL6**. There is approximately a linear relation between them; the dotted line, which serves as a guide, has a slope of 1. This indicates a strong correlation between the electrostatic and electrochemical hole injections in the thin films of **1**. Furthermore, it is recognized that the values of V_T and V_{OX} for the ionic-liquid **IL1** are close to the corresponding ones of **IL3**, and the values for **IL2** are very similar to those of **IL4**. Note that **IL1** and **IL3** have a common anion (TFSI) and **IL2** and **IL4** commonly include BF_4. This strongly suggests that the hole-doping carrier injection is governed only by the anions of the ionic liquids. Figure 3-1 justifies this assumption; namely, it is only anions that form an EDL with holes in the thin films in the electrostatic process and only anions that penetrate into the thin films in the electrochemical process.

It is experimentally demonstrated that the order of carrier injection efficiency is **IL5** > **IL1** ≈ **IL3** > **IL2** ≈ **IL4** > **IL6**, namely, OTf > TFSI > BF_4 > PF_6. It can reasonably be thought that the polarizabilities of the former two are larger than the latter two, so that the former two anions would be adsorbed in greater number on the semiconductor interfaces and would form larger EDLs, which bring about more effective carrier injections. The difference between the two groups, (OTf, TFSI) and (BF_4, PF_6), can be rationalized by polarizability. Another possible factor is the size of the anions; TFSI is the largest, followed by OTf, PF_6, and BF_4 in this order. The electrostatic and

electrochemical processes need a close contact between anions and semiconductor and an anion penetration into the semiconductor, respectively (see Figure 3-1). The difference between OTf and TFSI, or between BF_4 and PF_6, could be explained by this size effect.

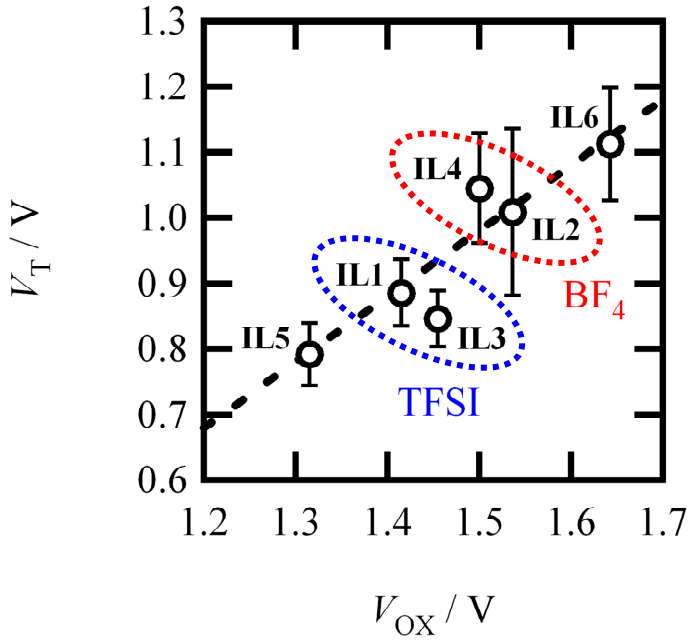

Figure 3-15. Threshold voltage V_T *vs.* oxidation peak voltage V_{OX} of EDL-OTFTs of **1**, calculated from the forward scan, for various ionic liquids, **IL1**–**IL6**.

3-3-4. Dual-Gate Transistors

The EDL-OTFTs of **1** exhibited a stable transistor performance with a rather high mobility, and a very low-power operation. In this section, dual-gate OTFTs of **1** are fabricated with **IL1** and SiO_2 as top- and bottom-gate dielectric-materials, respectively.

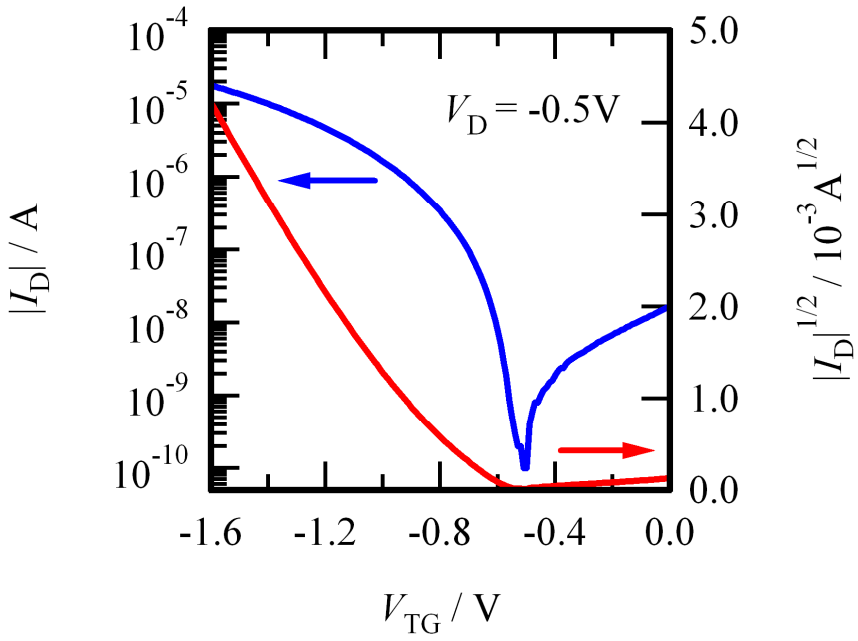

Figure 3-16. Transfer characteristics of the EDL-OTFT of **1** when the bottom-gate circuit is open. The blue and red curves represent the $|I_D|$ *vs.* V_{TG} and $|I_D|^{1/2}$ *vs.* V_{TG} plots, respectively.

Figure 3-16 shows the EDL-OTFT performance, namely, the source-drain current $|I_D|$ versus top-gate voltage V_{TG} plots, when the bottom-gate circuit is open. Note that the gate leakage current through the electrolytes is smaller than 0.2 μA. The values of I_D drastically increase below a threshold gate voltage of V_{TG}^{th}* = −0.5 V, where *

indicates that the SiO_2 bottom-gate is open. This behavior indicates that effective carrier doping takes place through the EDLs, when V_{TG} <−0.5 V. The obtained performance is nearly the same as that of the single-gate EDL-OTFTs of **1** with **IL1**, as reported in the sections 3-3-2 and 3-3-3, except for on/off current ratio. The on/off ration of this device is above 10^5, which value is observed from direct current (DC) measurement, while previous EDL-OTFTs have small value of about 1 with alternate current (AC) method.

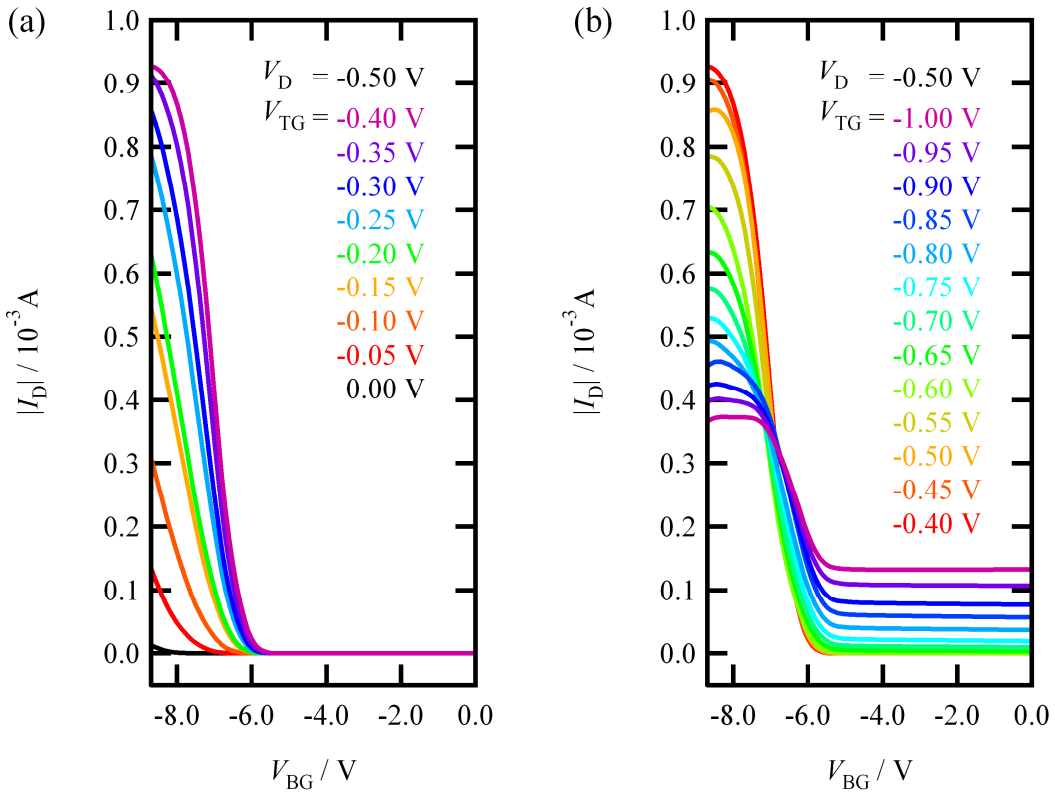

Figure 3-17. V_{TG} dependence of the transfer characteristics of the dual-gate OTFT, operated by the bottom-gate voltage V_{BG}, in the range of (a) V_{TG} = 0.0 ~ −0.4 V and (b) −0.4 ~ −1.0 V.

Figure 3-17(a) shows the transfer characteristic, operated by the bottom-gate voltage V_{BG}, namely, $|I_D|$ versus V_{BG} plots, under a constant V_{TG} in the range from 0.0 to −0.4 V at a source-drain voltage of V_D = −0.5 V. At V_{TG} = 0.0 V, the curve exhibits OTFT performance with a threshold voltage of V_{BG}^{th} = −7.8 V. When a negative V_{TG} is loaded, a significant improvement in the OTFT performance is observed, even when V_{TG} > V_{TG}^{th*} (= −0.5 V); the values of V_{BG}^{th} exhibit a significant increase with a decrease in V_{TG}. These results indicate that V_{TG} produces an effective field at the interface of the SiO_2 bottom gate-dielectrics and assists with carrier doping from this gate. Figure 3-17(b) shows the I_D versus V_{BG} plots in the range of −0.4 V> V_{TG} >−1.0 V at V_D = −0.5 V. When V_{TG} < V_{TG}^{th*}, the OTFT performance is observed, but V_{TG} gradually increases the off current while it remains negligibly small in the range of V_{TG} > V_{TG}^{th*}.

Figure 3-18(a) shows the V_{TG} dependence of the on-off current ratio. It can be seen that high ratios of more than 10^4 are maintained in the range of 0.0> V_{TG} >−0.5 V, while below −0.5 V, they show a quick decrease to approximately one at V_{TG} = −1.0 V. Figure 3-18(b) shows the V_{TG} dependencies of the subthreshold slope $\partial V_{BG}/\partial \log I_D$. In the range of 0.0> V_{TG} >−0.5 V, the values of $\partial V_{BG}/\partial \log I_D$ are constantly low (<−0.3 V decade^{-1}), while below −0.5 V, they show a gradual increase to approximately 3 V decade^{-1} at V_{TG} = −1.0 V. It is notable that the V_{TG}^{th*} value in Figure 3-16 roughly agrees with the critical V_{TG} value (−0.5 V) in the dependencies shown in Figures 3-18(a) and 3-18(b). The surface condition of the thin film of **1** is considered to be significantly changed when V_{TG} = −0.5 V. This phenomenon is probably caused by penetration or/and adsorption of the counter ions to the thin film surface, which brings about a significant increase in the off-current, thus spoiling the transistor performance.

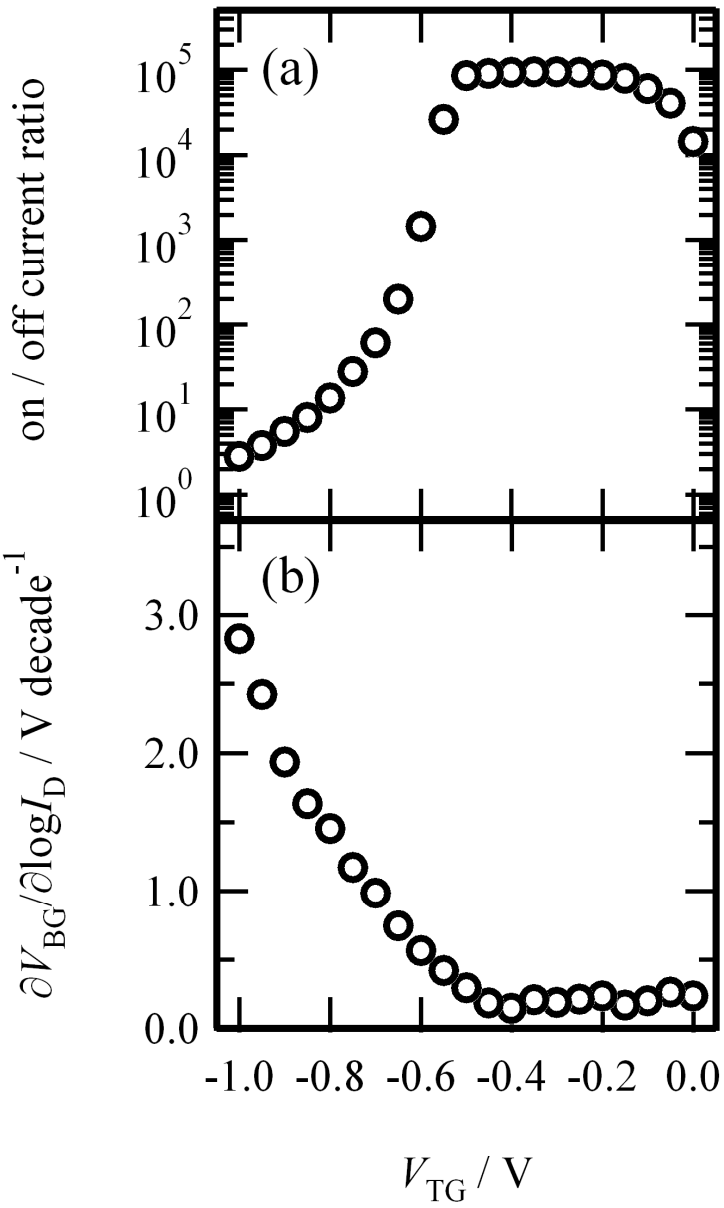

Figure 3-18. (a) V_{TG} dependence of the on-off current ratio and (b) the subthreshold slope.

Figure 3-19 shows the dependence of V_{BG}^{th} on V_{TG}, which is extracted from Figure 3-17. There is a linear relation between them with a slope of −3.2. In general, the

dual-gate transistors show a relation between V_{BG}^{th} and V_{TG}, which is expressed by

$$\frac{\partial V_{BG}^{th}}{\partial V_{TG}} = -\frac{CC_{TG}}{C_{BG}(C + C_{TG})}, \tag{3-5}$$

where C_{TG}, C_{BG}, and C are the capacitances of the top and bottom-gate dielectrics and the semiconductor, respectively.[158] Therefore, the symmetric dual-gate OTFTs, composed of the same gate-dielectrics, should exhibit a $\partial V_{BG}^{th}/\partial V_{TG}$ value of approximately −0.5.[143] In contrast, the values of C_{BG} and C_{TG} in the present dual-gate OTFT are 1.1×10^{-8} F cm^{-2} and 2.7×10^{-6} F cm^{-2}, respectively. Since C of the organic layer is estimated at 10^{-7} F cm^{-2}, the $\partial V_{BG}^{th}/\partial V_{TG}$ value would be on the order of tens, which can semiquantitatively explain the observed value.

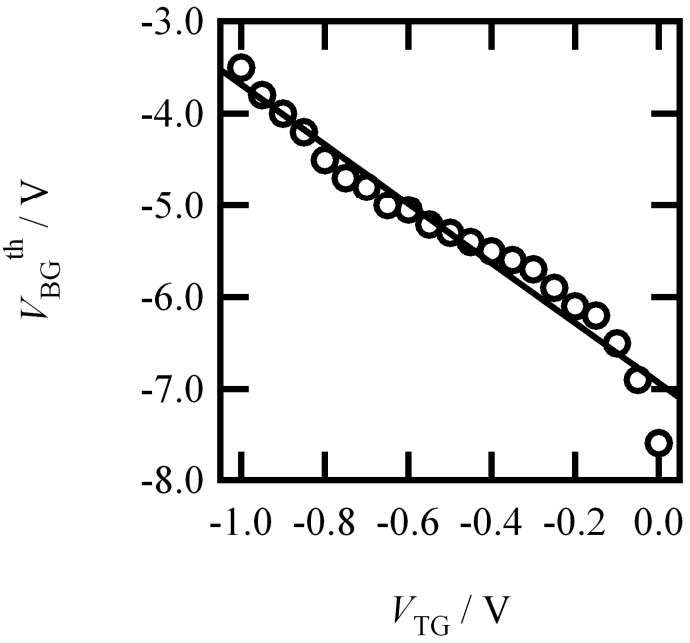

Figure 3-19. V_{TG} dependence of the threshold bottom-gate voltage V_{BG}.

3-3-5. Ambipolar Operation

The OTFTs of the thin film of **1** in the previous sections showed *p*-type operation, except in the case of double-layer OTFTs with **1** and a TCNQ molecule. The *n*-type behavior of double-layer OTFTs should arise from the TCNQ layer. These results indicated that the hole injection is easier than that of electron injection, and the hole transport is dominant for the thin film of **1**, which might be due to its donor nature. The relatively high hole transport characteristic of **1** is suitable for practical application, but to clear the electron transport characteristic is also important for revealing the nature of the electronic properties of **1**.

In this section, the ambipolar operations, including the hole and electron injection to the thin film, were achieved by EDL-OTFT configurations using ionic liquid BMIM-BF_4 (**IL4**) gate-dielectrics, despite the large HOMO-LUMO band gap (~5 eV, see section 2-3-2) of compound **1**. Figures 3-20(a) and 3-20(c) show the transfer characteristics of the *p*- and *n*-type operation of EDL-OTFTs with the ionic liquid **IL4**, respectively. These curves clearly indicate the ambipolar transport of compound **1** under low gate voltages less than 3 V. The hole and electron mobilities were 5.0×10^{-4} and 1.5×10^{-6} cm^2 V^{-1} s^{-1}, respectively. The *p*-type carrier injection requires only a small gate voltage of −0.9 V, but the *n*-type injection requires more than 2.0 V. This indicates that the EDL formation between anion/semiconductor is easier than that between cation/semiconductor.

The EDL-OTFTs of **1** with **IL1** shows *p*-type behavior, but never exhibits *n*-type operation, as shown in Figure 3-16. This significant dependence on the ionic liquids can be explained by the electrochemical potential, as discussed in the next chapter.

Table 3-2. Mobility in the linear region, threshold voltage, subthreshold slope, and on/off current ratio for the EDL-OTFTs of **1** with the ionic-liquid **IL4**.

	p-type	*n*-type
mobility / $cm^2\ V^{-1}\ s^{-1}$	5.0×10^{-4}	1.5×10^{-6}
threshold voltage / V	−0.9	2.0
on/off current ratio	10^6	10^3

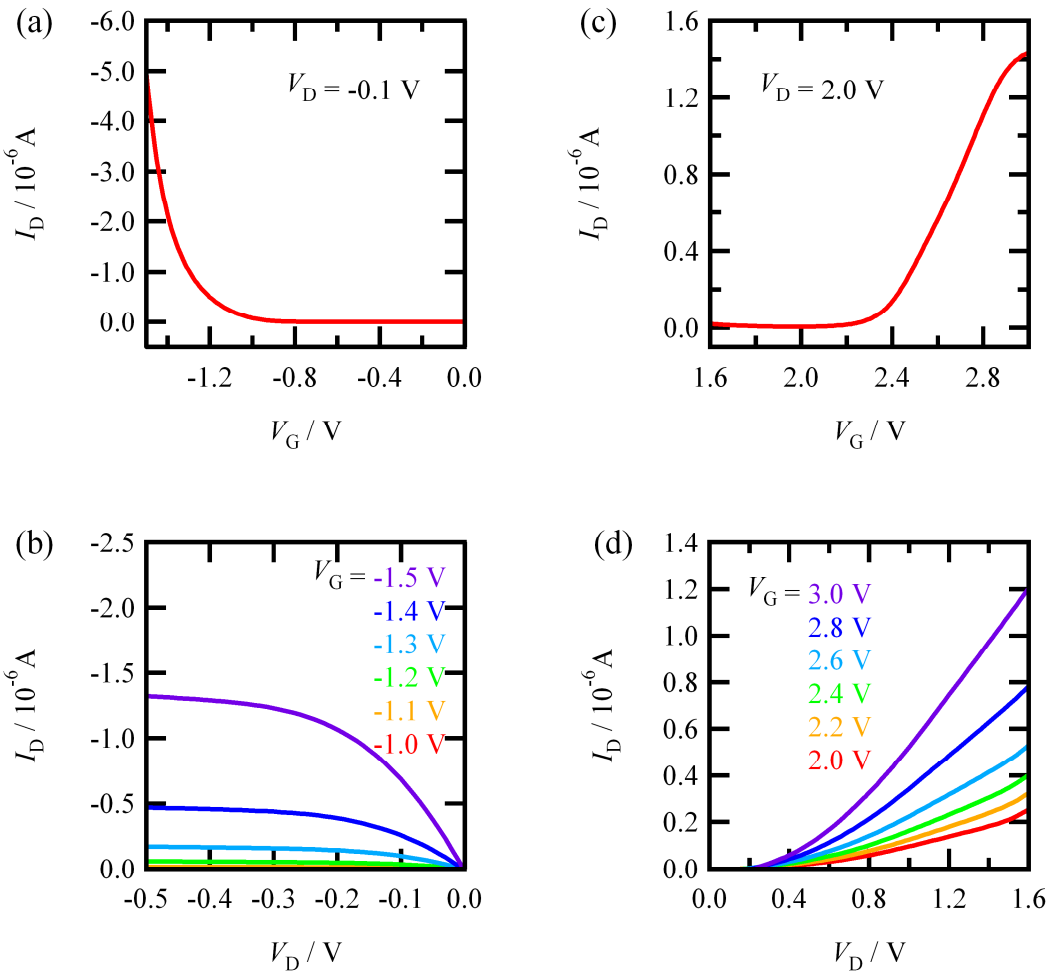

Figure 3-20. Transfer (panels (a) and (c)) and output (panels (b) and (d)) characteristics of the *p*- and *n*-type regions for the EDL-OTFTs of **1**, respectively.

3-4. Conclusion

Robust thin films of **1** have been found to be promising materials for EDL-OTFTs with ionic liquids; the thin films of **1** on Pt interdigitated electrodes in an ionic-liquid operated as *p*-type EDL-OFET with high performance. The performance, measured by the alternating current method, has indicated high mobility, high carrier density, and a threshold gate voltage which is much lower than the electrochemical oxidation potential of **1**. Using six kinds of ionic-liquid as a gate-dielectric material, or a solvent, the mobilities of the EDL-OTFTs showed a linear relationship between the capacitance of the ionic liquids. In contrast, it was experimentally demonstrated that the threshold voltage of EDL-OTFTs and the electrochemical ionization potential were governed by the anion component of the ionic liquids.

Dual-gate operation with ionic liquid and SiO_2 gate-dielectrics led to very good transistor performance with a high on/off ratio, a low threshold voltage, a low subthreshold slope, and low power operation, all of which surpassed those of the single-gate OTFTs of **1**. The dual-gate operation using ionic liquid is a promising method for improving the carrier concentrations in OTFTs and for realizing high-performance OTFTs.

Ambipolar operations have been achieved by choosing the appropriate ionic liquids **IL4**. The electron mobility of compound **1** is revealed to be 1.5×10^{-6} cm^2 V^{-1} s^{-1}, which is lower by two or three orders of magnitude than the hole mobility. The EDL-OTFT technique is useful to reveal the ambipolar transport properties of a compound with large HOMO-LUMO gap, such as **1**.

Chapter 4

Electric-Double-Layer Transistors with Robust Organic Materials

4-1. Introduction

In the development of organic transistors, various applications of these transistors to inverters and other logic devices have been proposed.[159–162] The inverter function is fundamental in advanced integrated circuits, and organic inverters are advantageous for circuit design and large area fabrication.[163–165] Among the several types of inverter circuits, a complementary technology that is achieved by cooperation between *p*- and *n*-type transistors leads to lower power dissipation than that occurring with inverters based on a single transistor. To create high-performance complementary inverters, a match between the mobility and threshold voltage between *p*- and *n*-type semiconductors is important,[166–168] as well as the individual performance of the component transistors.

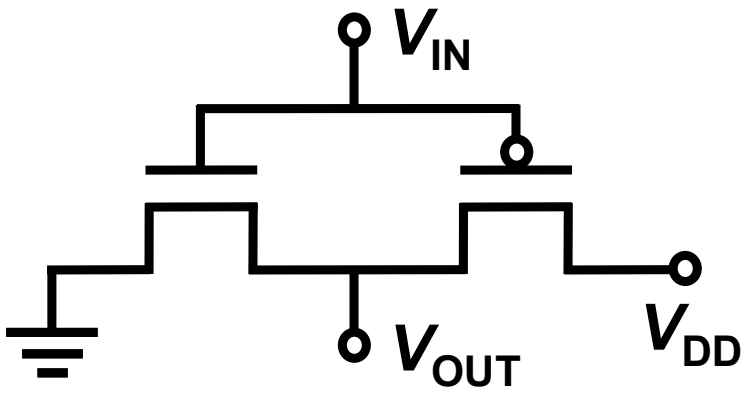

Figure 4-1. Circuit configuration of a complementary inverter.

Phthalocyanine (Pc) derivatives are well known as dyes, and have been utilized in organic/molecular electronic devices as *p*-type semiconductors.[103,169–171] The hole mobility of the organic thin-film transistors (OTFTs) of metal-free phthalocyanine (H_2Pc, see Figure 4-2) using SiO_2 gate-dielectrics is 1.3×10^{-3} or 2.6×10^{-3} cm^2 V^{-1} s^{-1} deposited at 30°C or 125°C, respectively.[172] In contrast, tetrakis(thiadiazole) porphyrazine (TTDPz, see Figure 4-2), synthesized by Ercolani *et al.*, is known to exhibit *n*-type semiconductor behavior.[173–176] Suzuki *et al.* carried out the crystal growth, structural analysis, thin film fabrication by vacuum thermal evaporation, and electrochemistry of H_2TTDPz.[177–179]

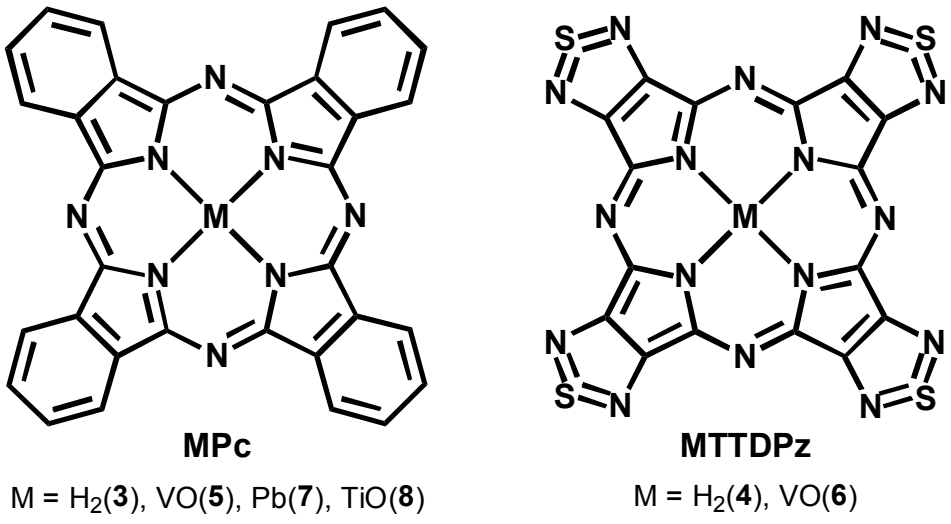

Figure 4-2. Molecular structures of MPc and MTTDPz.

While MPc and MTTDPz (M = H_2 and VO) were found to operate as unipolar transistors, the lead- and titanyl-phthalocyanines (MPcs with M = Pb and TiO (see Figure 4-2) are known to exhibit an ambipolar transport due to their low band gaps.[180,181]

In Chapter 3, EDL-OTFTs with ionic-liquid gate-dielectrics were demonstrated with octathio[8]circulene (**1**) thin film, and revealed high performance with low applied voltage. In this chapter, stable porphyrazine materials were adopted as semiconductors for EDL-OTFTs. The EDL-OTFT technique can be easily adopted for robust thin films, and is convenient for analyzing the electric properties of semiconductors and for application to practical logic devices. The subsequent logic devices, i.e., complementary organic inverters, were also developed by combination with *p*- and *n*-type porphyrazines. An ionic liquid was utilized as the gate-dielectric for the present organic inverters. It should be noted that thin films of MPc and MTTDPz are stable even in ionic liquids, though most of the molecule-based organic semiconductors dissolve into them. The operation behavior was evaluated by using these robust *p*- and *n*-type organic thin films.

The ambipolar EDL-OTFTs of PbPc and TiOPc were also prepared by testing various ionic liquids. Based on the electrochemical analysis and DFT calculation, the controlling factors of the EDL-OTFTs were discussed.

4-2. Experimental

The compounds **3**, **7** and **8** were purchased from Tokyo Chemical Industry and purified by sublimation. Other compounds **4**, **5**, **6**, were prepared by the method described in refs. [173], [182] and [183], respectively. Thin films of these organic compounds with the thickness of 50 nm were fabricated by vacuum thermal evaporation in a vacuum of 10^{-4} Pa at a rate of 0.5 nm min^{-1} on interdigitated array electrodes (Metal on SiO_2). The evaporation temperatures were 350°C, 565°C, 400°C, 450°C, 480°C and 410°C for **3**–**8**, respectively.

The ionic liquids **IL1**–**IL10** were purchased from Kanto Reagent and were used without further purification. The top-gate was prepared with a droplet (~20 mm^3) of ionic liquid that covered the whole area (~20 mm^2) of the thin films, and a Pt wire (for EDL-OTFTs of **3**–**6**) or coil (for EDL-OTFTs of **7** and **8**) that was inserted into the ionic liquid. The transistor performances were examined by using Keithley 2636 system at room temperature under dark and vacuum conditions.

The circuit of the complementary OTFTs inverter is shown in Figure 4-1. The ionic-liquid gate-dielectrics with a Pt gate electrode is common for the two OTFTs. The inverter performance was examined at room temperature under dark and vacuum conditions. The dynamic response characteristics were measured by using a function generator and an oscilloscope.

The electrochemical analyses of ionic liquid were performed on Hokuto HZ-5000 electrochemical analyzer. A platinum wire and an Ag/Ag^+ electrode were used as working and reference electrodes, respectively.

4-3. Results and Discussion

4-3-1. Unipolar Transistors

4-3-1-1. Metal-Free Porphyrazines

The EDL-OTFT performances of **3** and **4**, on interdigitated array electrodes (Pt) in which the channel dimensions were w = 100 cm in width and L = 2 μm in length, using **IL1** as gate-dielectrics with a Pt gate-electrode, were examined. Figures 4-3(a) and 4-3(c) show the transfer characteristic of **3** and **4**, namely, the $|I_D|^{1/2}$ versus V_G plots, with a source-drain voltage of V_D = ±0.5 V. These OTFTs show normally off states below threshold voltages, and with an increase in $|V_G|$ values, the values of $|I_D|$ show a quick increase. This behavior clearly indicates that **3** and **4** operates as *p*- and *n*-type semiconductors, respectively. Extrapolation of the $|I_D|^{1/2}$ versus V_G curve from the large V_G range indicates a very low threshold voltage of V_T = −0.2 V for **3**, and −0.1 V for **4**, respectively. Such low power operation is an advantage of EDL-OTFTs. The threshold voltage for **4** is very low (<0 V), indicating that this compound is useful for large carrier injection from Pt electrodes. It is notable that the curves in Figure 4-3(c) are associated with small hysteresis loops with a width of ~0.2 V for **4** and of ~0.1 V for **3**, in the forward and reverse scans of V_G. The difference in the loop width between the OTFTs of **4** and **3** could be explained by the difference in the counter ions, which form an electric bilayer on the semiconductor surfaces.

Figures 4-3(b) and 4-3(d) show the output characteristic. There is little deviation from zero current with an increase in V_G, indicating that the current leakage through the dielectric is negligibly small.

Table 4-1. Mobility in the linear region, threshold voltage, subthreshold slope, and on/off current ratio for the EDL-OTFTs of **3** and **4** with the ionic-liquid **IL1**.

	H_2Pc (**3**)	H_2TTDPz (**4**)
	p-type	*n*-type
mobility / $cm^2\ V^{-1}\ s^{-1}$	0.004	0.001
threshold voltage / V	−0.2	−0.1
subthreshold slope / V $decade^{-1}$	0.55	0.36
on/off current ratio	10^3	10^4

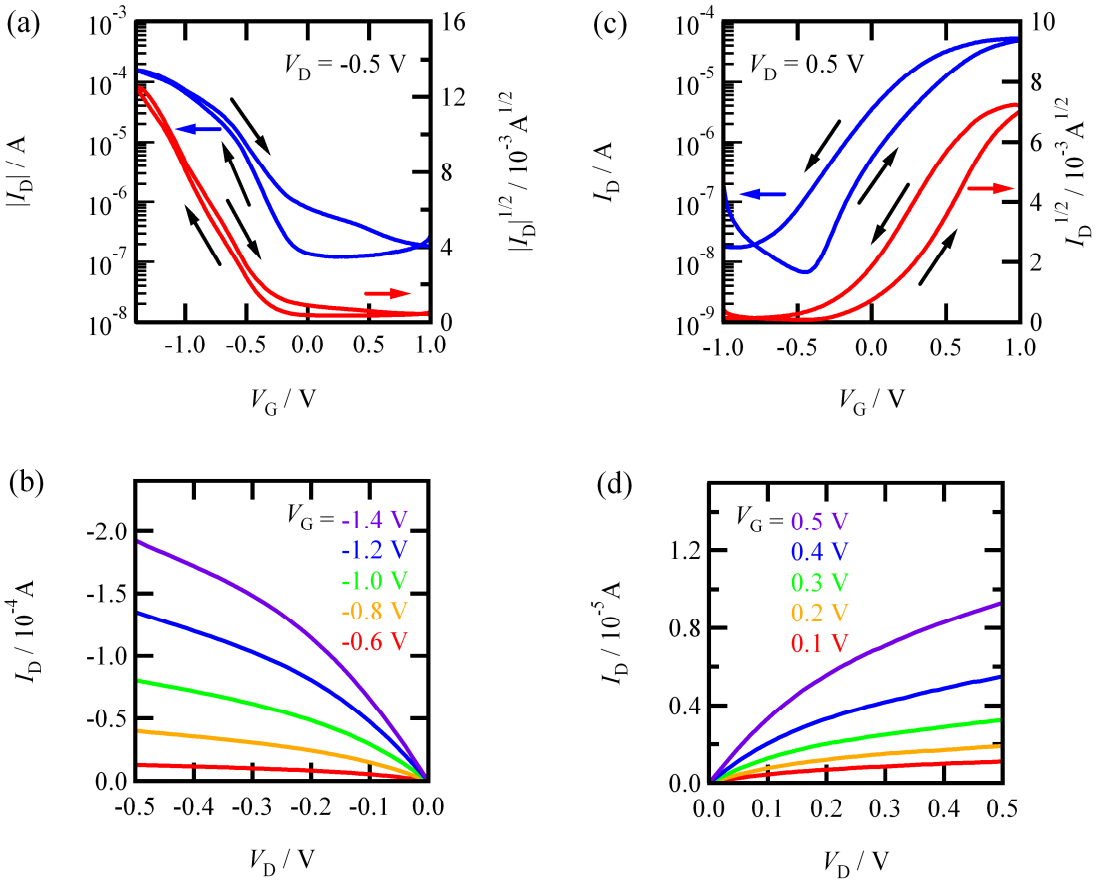

Figure 4-3. Transfer (a), (c) and output (b), (d) characteristics of EDL-OTFTs of **3** and **4**, respectively. The black solid arrows in (a) and (c) represent the sweep directions.

4-3-1-2. Vanadyl Oxide Porphyrazines

The EDL-TFTs technique were adopted for the paramagnetic thin films of **5** and **6**, on interdigitated array electrodes (Au) in which the channel dimensions were w = 10 cm in width and L = 20 μm in length. The results are shown in Figure 4-4. From these data, the mobility in the linear region, as well as the threshold voltage, subthreshold slope, and on/off current ratio are obtained, as listed in Table 4-2. The OTFT performance clearly indicates that **5** and **6** operate as *p*- and *n*-type semiconductors, respectively, with nearly the same transport properties. They exhibit a large source-drain current $|I_D|$ in the range of μA, generated with small-gate voltages V_G and source-drain voltages V_D (<1 V), while the gate leakage current $|I_G|$ is negligibly small (<0.1 μA). The I_D value at off state is less than 10 nA, indicating that the normally off EDL-OTFT.

Despite the thin films of **6** being amorphous,[183] the mobility value is two orders of magnitude higher than those of the closed-shell derivatives, H_2TTDPz (**4**) and is one of the highest values for organic *n*-type TFTs.[184] It is worth noting here that the mobilities of VOPc and TiOPc are higher than those of H_2Pc and the divalent metal Pc's. This suggests that axially coordinated porphyrazines possess higher mobilities than the planar metal-free and divalent derivatives. Nonetheless, it is hard to rationalize these facts because the mobilities of organic thin films are governed by various factors, such as the intramolecular electronic state, molecular packing, lattice defects, and chemical impurities. As is discussed by Inabe *et al.*, however, the partial overlaps that are commonly observed in these materials due to the presence of the axial ligands can bring about multidimensional structures.[169] This is probably advantageous for carrier transport, which is not significantly affected by lattice defects and distortion.

Table 4-2. Mobility in the linear region, threshold voltage, subthreshold slope, and on/off current ratio for the EDL-OTFTs of **5** and **6** with the ionic-liquid **IL1**.

	VOPc (**5**)	VOTTDPz (**6**)
	p-type	*n*-type
mobility / $cm^2\ V^{-1}\ s^{-1}$	0.012	0.028
threshold voltage / V	−0.48	0.13
subthreshold slope / V $decade^{-1}$	0.14	0.25
on/off current ratio	10^5	10^4

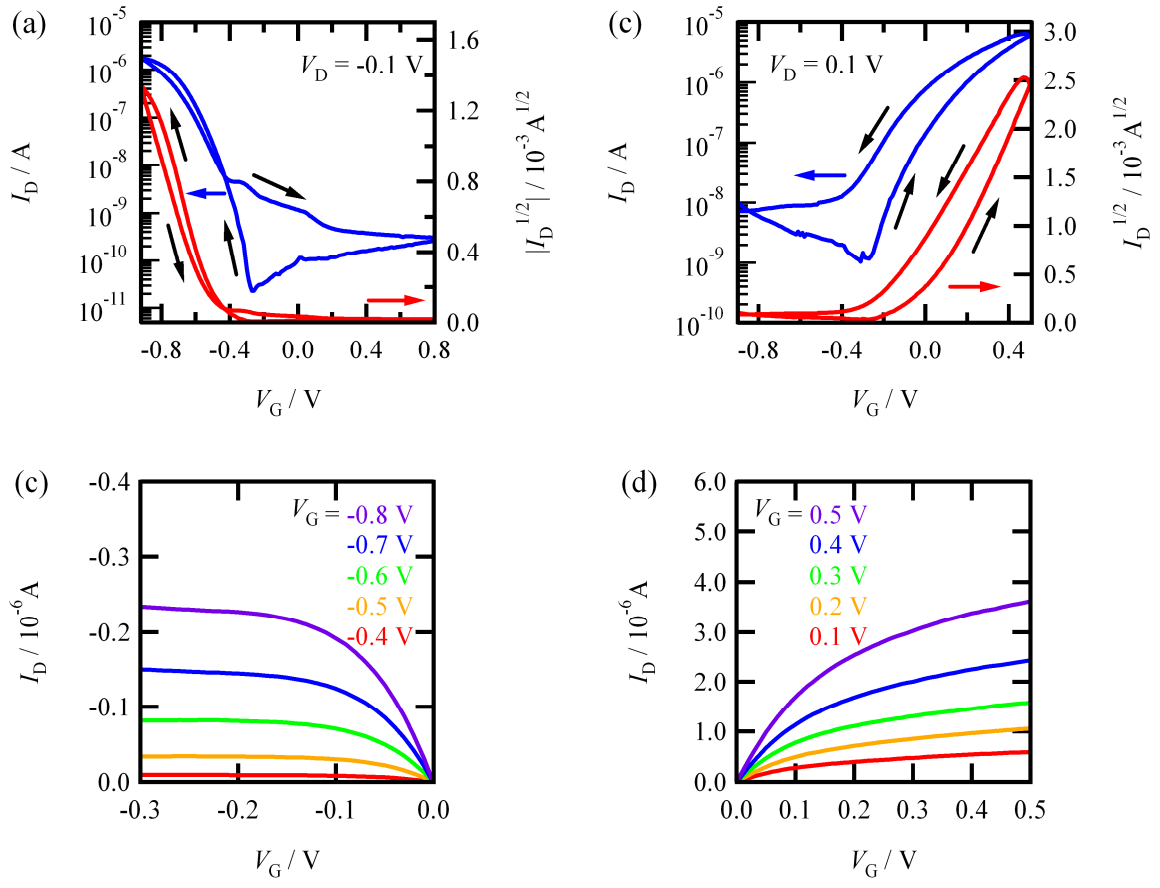

Figure 4-4. Transfer (a), (c) and output (b), (d) characteristics of EDL-OTFTs of **5** and **6**, respectively. The black solid arrows in (a) and (c) represent the sweep directions.

4-3-2. Complementary Inverters

In the section 4-3-1, it can be concluded that the porphyrazine-based EDL-OTFTs exhibit relatively high mobilities, low threshold voltages, low subthreshold slopes, and a high on/off ratio using ionic-liquid gate-dielectrics, with nearly the same performance in the pair of **3** and **4**, and **5** and **6**, respectively. They are applicable to complementary organic inverters. In this section, the complementary inverters were performed using ionic-liquid gate-dielectrics as shown in Figure 4-5.

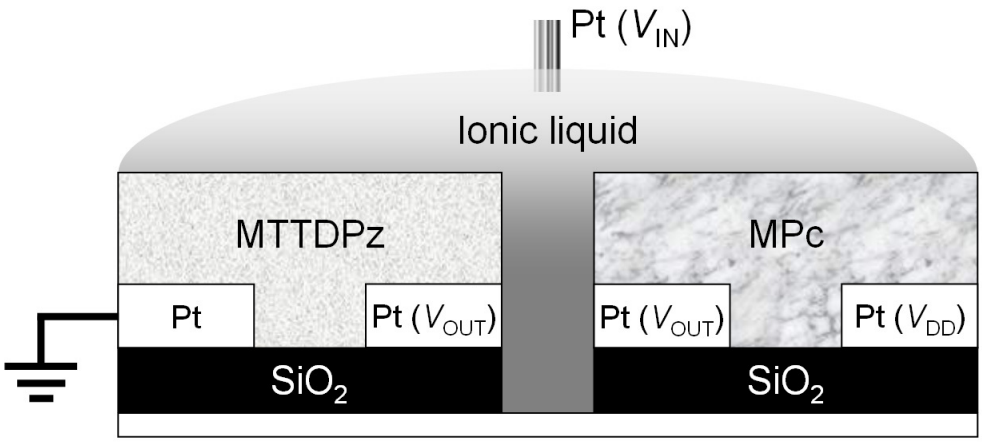

Figure 4-5. Circuit configuration of a complementary OTFT inverter using unipolar MPc and MTTDPz (M = H_2, VO), and an ionic-liquid gate-dielectrics.

4-3-2-1. Metal-Free Porphyrazines

The transfer characteristics of the inverter composed of **3** and **4** are shown in Figure 4-6(a), where the voltages V_{IN}, V_{OUT}, and V_{DD} are defined in Figure 4-5. The solid and broken curves show the results with a decrease and an increase in V_{IN}, respectively, between V_{IN} = −1.0–1.0 V. The inverter switching characteristics can be clearly seen, and, as expected from the low threshold voltages of the component transistors (see Table 4-1), this inverter works at very low supply voltages. The hysteresis loops formed by the solid and broken curves are probably caused by the hysteresis behavior of the OTFTs of **4**.

The values of the signal-gain $\partial V_{OUT}/\partial V_{IN}$ are calculated from Figure 4-6(a), and are plotted *vs.* V_{IN} in Figure 4-6(b). The solid and broken curves correspond to those in Figure 4-6(a). Although the supply voltage V_{IN} is low, the gain values are rather high, reaching −3 when V_{DD} = 0.5 V. The leakage current I_{DD} is very small and the static power dissipations are also small; namely 1 nW and 50 nW for V_{DD} = 0.1 V and 0.5 V, respectively. These characteristics indicate low power dissipation in the standby state.

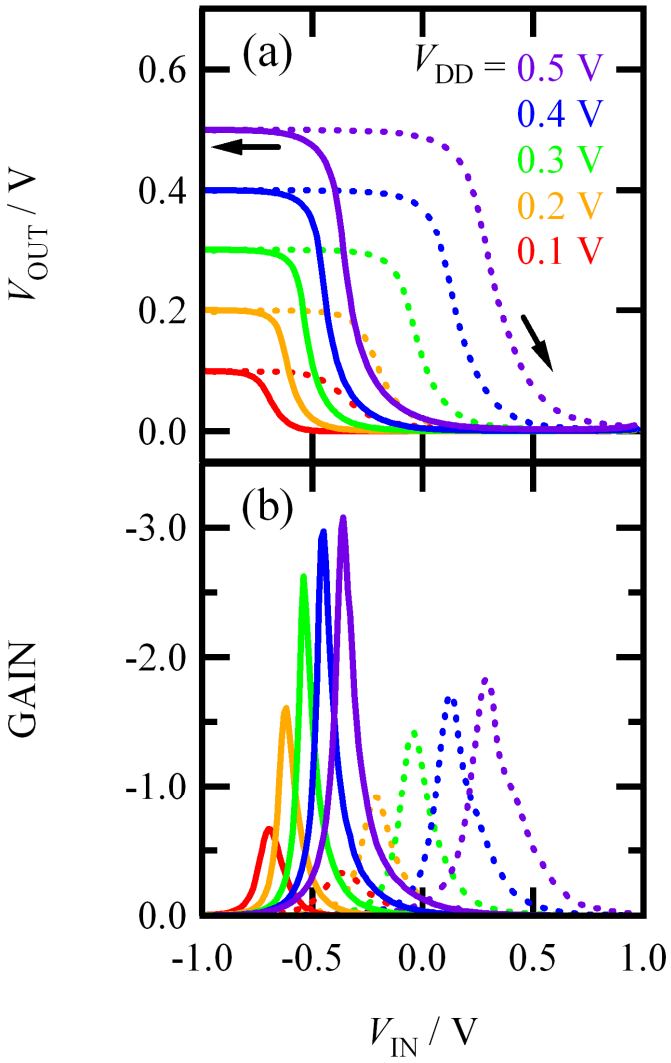

Figure 4-6. (a) Transfer characteristics of a complementary OTFT inverter of **3** and **4** in the ionic-liquid gate-dielectrics **IL1**. The arrows represent the sweep directions. (b) The signal gains of the complementary OTFT inverter.

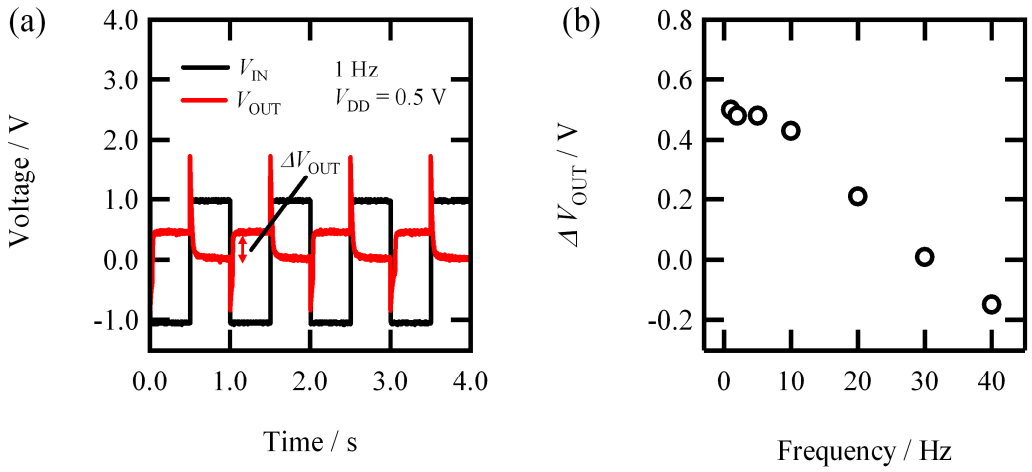

Figure 4-7. (a) Dynamic response characteristics of complementary OTFTs inverter measured under 1.0 V peak-to-peak square input signal at 1 Hz frequency with V_{DD} = 0.5 V. (b) Frequency dependences of ΔV_{OUT} under 1.0 V peak-to-peak square input signal at 1–40 Hz frequencies with V_{DD} = 0.5 V.

The dynamic response characteristics of the present inverter were measured at 1 Hz frequency with V_{DD} = 0.5 V. The results are shown in Figure 4-7(a), where the black and red curves indicate the input voltage V_{IN} and output voltage V_{OUT}, respectively. V_{IN} is a square wave between −1 and 1 V, and V_{OUT} exhibits an inverter response to V_{IN} with a transient behavior just after the changes in V_{IN}. The rising (t_r) and falling (t_f) times of V_{OUT} are obtained as 45 and 60 ms, respectively, which are defined as a time from 10 to 90% of the change between the two steady-state values. It is confirmed that the inverter performance can be maintained up to 20 Hz (See Figure 4-7(b)), though the transient output voltage decreases with an increase in frequency. The upper limit of the fast response (20 Hz) could be governed by the diffusion limit of the ionic molecules in the gate-dielectric liquid.

4-3-2-2.Vanadyl Porphyrazines

The transfer characteristics of the inverter composed of **5** and **6** are shown in Figure 4-8(a). The inverter switching characteristics can be clearly seen with same as that of **3** and **4**. The degree of hysteresis loops of this inverter were decreased compared to the devices descried in 4-3-2-1.

The values of the signal-gain $\partial V_{OUT}/\partial V_{IN}$ are calculated from Figure 4-8(a), and are plotted *vs.* V_{IN} in Figure 4-8(b). The gain values are higher than that of **3** and **4**, reaching −6 when V_{DD} = 0.5 V. The leakage current I_{DD} is very small and the static power dissipations are also small; namely 3 nW and 40 nW for V_{DD} = 0.1 V and 0.5 V, respectively. The obtained performance of the present organic complementary inverter is high enough to be applied to the subsequent stage logic devices such as a ring oscillator.

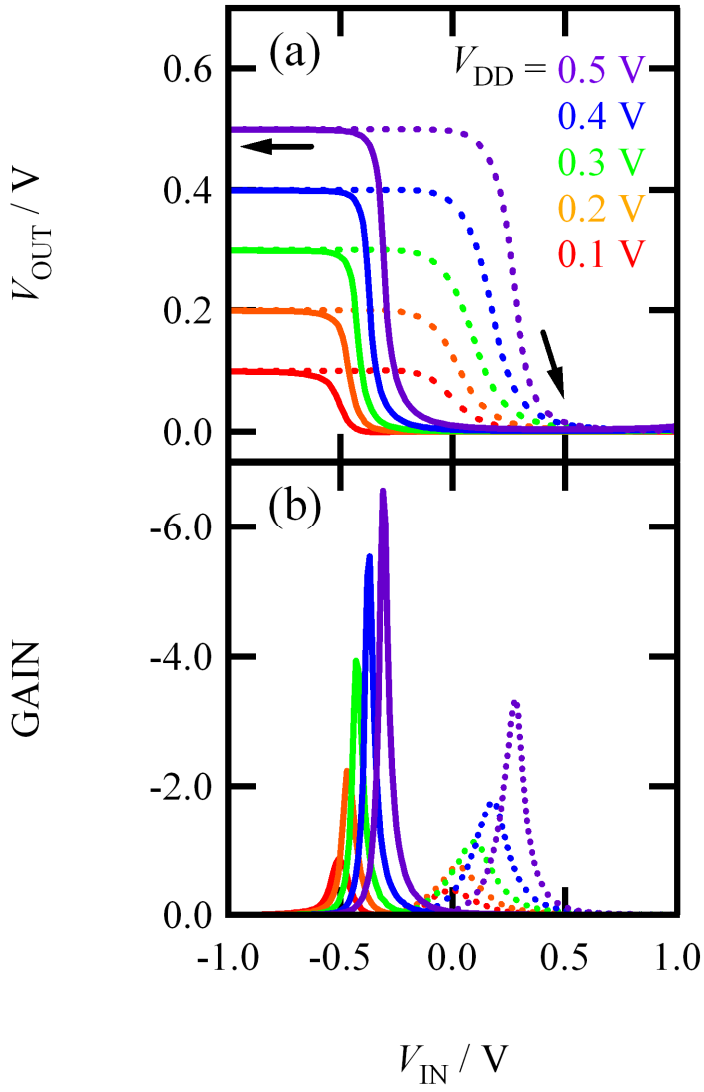

Figure 4-8. (a) Transfer characteristics of a complementary OTFT inverter of **5** and **6** in the ionic-liquid gate-dielectrics **IL1**. The arrows represent the sweep directions. (b) Signal gains of the complementary OTFT inverter.

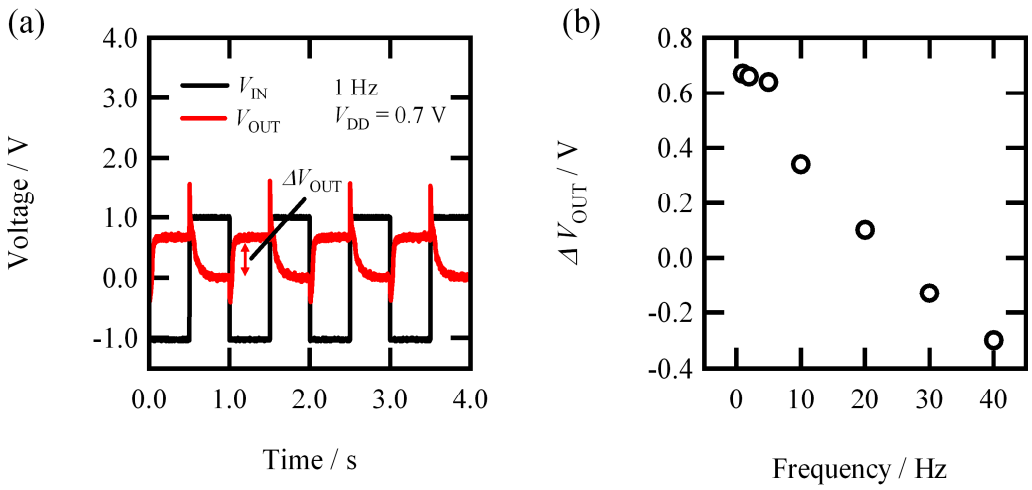

Figure 4-9. (a) Dynamic response characteristics of complementary OTFTs inverter measured under 1.0 V peak-to-peak square input signal at 1 Hz frequency with V_{DD} = 0.5 V. (b) Frequency dependences of ΔV_{OUT} under 1.0 V peak-to-peak square input signal at 1–40 Hz frequencies with V_{DD} = 0.7 V.

The dynamic response characteristics were measured at 1 Hz frequency with V_{DD} = 0.5 V. The results are shown in Figure 4-9(a), where the black and red curves indicate the input voltage V_{IN} and output voltage V_{OUT}, respectively. V_{IN} is a square wave between −1 and 1 V, and V_{OUT} exhibits an inverter response to V_{IN} with a transient behavior just after the changes in V_{IN}. The t_r and t_f of V_{OUT} are obtained as 45 and 60 ms, respectively. They suggest the practical utility of the present inverter. It is confirmed that the inverter performance can be maintained up to 20 Hz (See Figure 4-9(b)), though the transient output voltage decreases with an increase in frequency. The upper limit of the fast response (20 Hz) could be governed by the diffusion limit of the ionic molecules in the gate-dielectric liquid.

4-3-3. Ambipolar Devices

4-3-3-1. Ambipolar EDL-OTFT Operation

The red and blue curves in Figure 4-10(a) show the transfer characteristics of the PbPc and TiOPc EDL-OTFTs with the ionic liquid **IL1**, respectively. These curves clearly indicate the ambipolar transport of these materials under low gate voltages less than 2 V. It is characteristic that a large source-drain current $|I_D|$ on the order of 0.1 mA can be generated by a combination of small gate $|V_G|$ and source-drain $|V_D|$ voltages less than 2.0 V, while the gate leakage current $|I_G|$ is negligibly small (<0.5 μA). Note that small hysteresis loops with a width of <0.2 V were always observed for the present MPcs EDL-OTFTs in the forward and reverse scans of V_G, which would be caused by an interaction between the counter ions and the semiconductor surface, as discussed in previous chapters. Since the reverse scan is considered to better reflect this effect, the results of the forward scans will be discussed.

The performance of the other EDL-OTFTs with the ionic liquids **IL2**–**IL10**, are shown in Figures 4-10(b)–4-10(j). The EDL-OTFTs of MPcs with **IL2** and **IL6** did not show the *n*-type behavior, but they still operated as *p*-type OTFTs. The mobilities are about 10^{-2} (hole) and 10^{-3} cm^2 V^{-1} s^{-1} (electron) for PbPc EDL-OTFTs, and about 10^{-3} cm^2 V^{-1} s^{-1} (both hole and electron) for TiOPc EDL-OTFTs. Table 4-3 shows the electrochemical potentials, the threshold voltages of the EDL-OTFTs, and the viscosities for the ionic liquids **IL1**–**IL10**. For the EDL-OTFTs of these MPcs, the *p*-type carrier injection requires only a small gate voltage of <0.5 V, but the *n*-type injection requires more than 1.0 V. This indicates that the EDL formation between anion/semiconductor is easier than that between cation/semiconductor. It is considered

that the surface of the organic semiconductors would be covered by the anions under the zero gate bias conduction. The two ionic liquids **IL2** and **IL6** exhibit unusually high viscosities, 1200 mPas for **IL2** and 382 mPas for **IL6**,[185,187] in contrast to those of the other ionic liquids, which are less than ~150 mPas. The absence of the *n*-type transistor performance in the EDL-OTFTs of **IL2** and **IL6** is presumably caused by their high viscosities, which would decrease the ionic mobilities, and prevent the replacements of the anions at the interfaces. The other possible cause is the limited width of the electrochemical window for **IL2** and **IL6**, which brings about a high carrier-injection barrier from the gate-dielectrics to the semiconductor and an unstable electron injection.

Table 4-3. Electrochemical potentials E_{WR}, threshold voltages of hole V_T^p and electron V_T^n dopings in the PbPc and TiOPc EDL-OTFTs for the ionic liquids **IL1**–**IL10**, and viscosities at 293.15 K for **IL1**–**IL7** and at 298.15 K for **IL8**–**IL10**.

Ionic liquid	E_{WR} / V	PbPc		TiOPc		Viscosity / mPas
		V_T^p / V	V_T^n / V	V_T^p / V	V_T^n / V	
IL1	0.15	0.18	1.57	−0.054	1.28	120[a]
IL2	0.26	0.21	–	0.025	–	1200[a]
IL3	0.082	0.25	1.52	−0.25	1.10	64[b]
IL4	−0.13	−0.21	0.97	−0.62	0.55	132[c]
IL5	−0.082	−0.22	0.84	−0.33	0.78	92[d]
IL6	0.028	0.055	–	−0.22	–	382[c]
IL7	−0.043	−0.19	0.98	−0.31	0.84	44[e]
IL8	0.13	0.021	1.42	−0.17	0.96	72[f]
IL9	0.070	−0.099	1.09	−0.19	1.04	117[g]
IL10	0.0095	0.029	1.42	−0.11	1.00	63[h]

a: ref. 185; *b*: ref. 186; *c*: ref. 187; *d*: ref. 188; *e*: ref. 189; *f*: ref. 190; *g*: ref. 191; *h*: ref. 192.

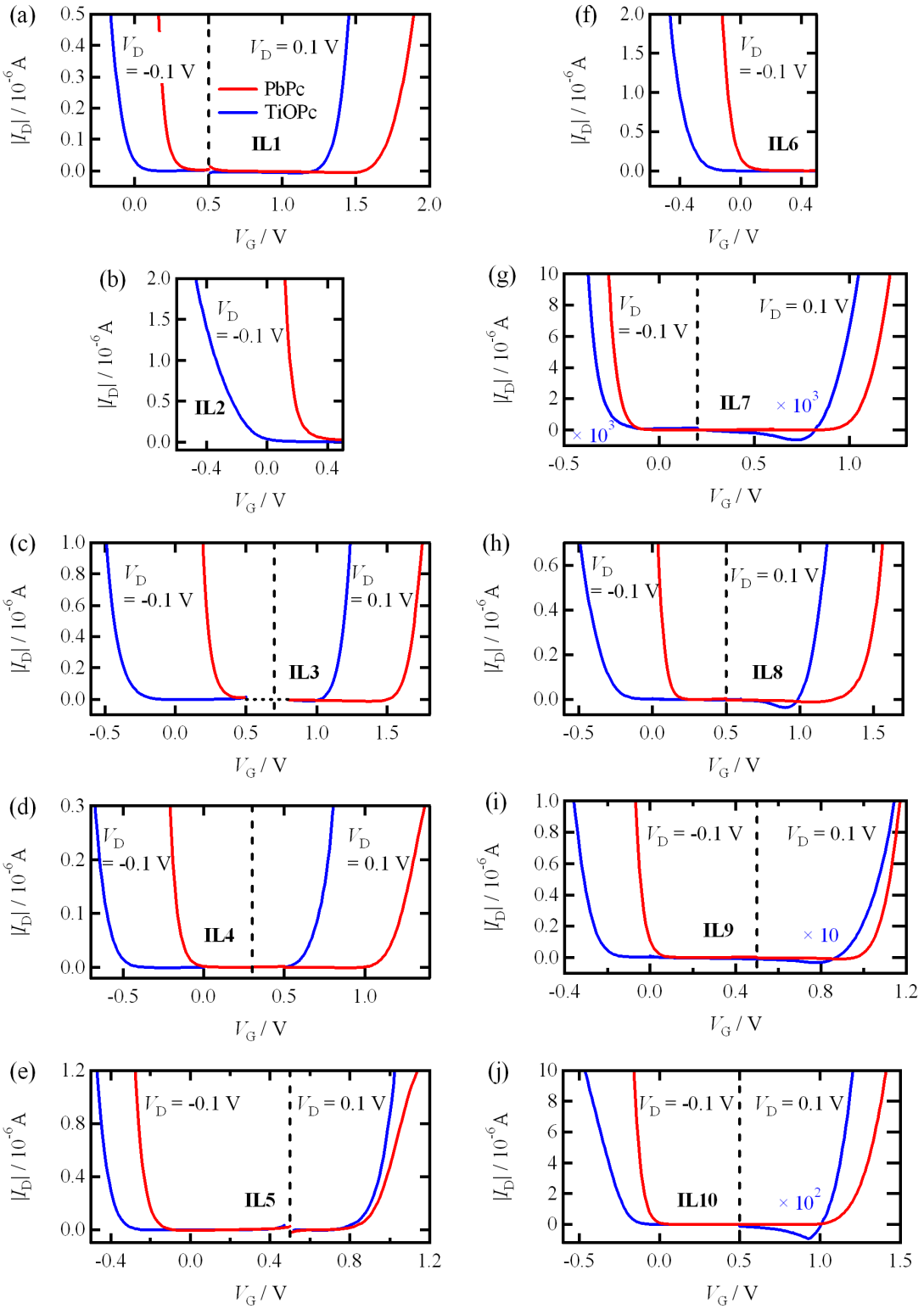

Figure 4-10. Transfer characteristics of the ambipolar PbPc and TiOPc EDL-OTFTs with the ionic liquid **IL1-IL10**.

4-3-3-2. Threshold Voltages of Electron and Hole Injection

Figure 4-11(a) depicts the relation between the *p*- and *n*-type threshold voltages, V_T^p and V_T^n, for the PbPc EDL-OTFTs with the various ionic liquids except **IL2** and **IL6**. It is found that the values of V_T^p and V_T^n significantly depend on the gate-dielectric ionic liquids; the ionic liquids can modulate the threshold voltages by 0.6 V for both hole and electron injections. In addition, there is a linear relation between V_T^p and V_T^n. Figure 4-11(b) shows the results for the TiOPc OTFTs, which show a similar relation between V_T^p and V_T^n. Since the energy gap between the highest occupied molecular orbital (HOMO) and the lowest unoccupied molecular orbital (LUMO) of the semiconductors is not strongly affected by the ionic liquids, the difference between V_T^p and V_T^n is probably maintained.

The broken lines in Figures 4-11(a) and 4-11(b) exhibit the slopes of 1.53 and 1.14 for the PbPc and TiOPc EDL-OTFTs, respectively. These values mean that the electron injection suffers a higher potential barrier than that for the hole injection in the two devices. One possible cause is a large electron injection barrier from the platinum electrode due to its large work function (~6 eV).[193,194] The others are *iR* drops between the source and gate electrodes and/or polarization effects at solid/liquid interfaces. The *iR* drop becomes significant when there is a large current flow between them. In the present experiments, a platinum coil was used as a gate electrode for effective carrier injections, and as a consequence, the large surface area of the gate might have induced a significant *iR* drop. In addition, the polarization effects may also have been responsible for reducing the source-gate potential difference, due to the formation of the EDLs at the interfaces. It is possible that this polarization effect is more significant for electrons rather than holes.

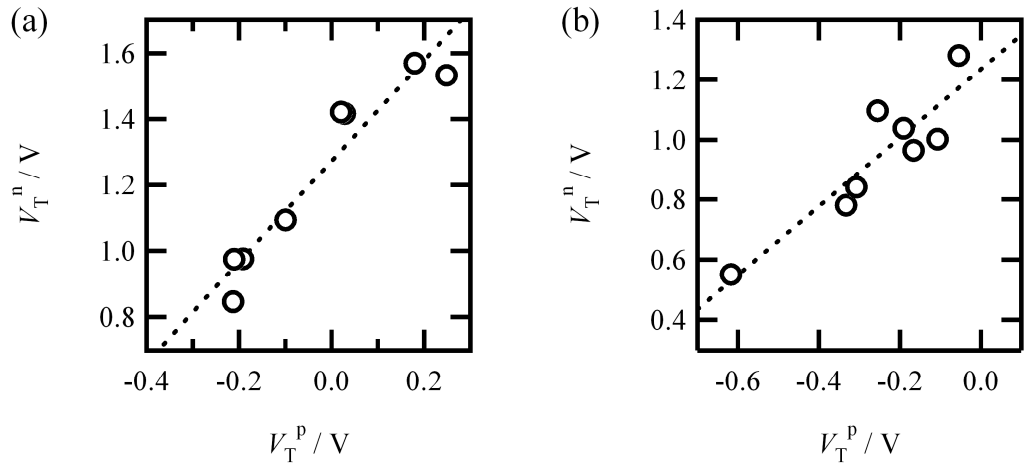

Figure 4-11. Threshold voltage relationships between electron V_T^n and hole V_T^p for PbPc (a) and TiOPc (b) EDL-OTFTs.

4-3-3-3. Electrochemical Potential

The threshold voltages of the EDL-OTFTs were significantly dependent on the ionic liquids. To reveal what controls the electron and hole injections in the present EDL-OTFTs, the electrochemical potentials, E_{WR}, of the ionic liquids, **IL1**–**IL10**, were measured, which were determined as

$$E_{WR} = E_W - E_R , \tag{4-1}$$

where E_W and E_R are the potentials of the working and reference electrodes, respectively. E_W is expressed by[195–198]

$$eE_W = \Phi_W + e(\psi_W - \psi_S) , \tag{4-2}$$

where Φ_W is the work function of the working electrode and $e(\psi_W - \psi_S)$ is the potential difference between the working electrode and the solution at the interface. E_R is a standard value in electrochemical analysis. Therefore, E_{WR} indicates the electrochemical potential of the solution, which includes the difference in contact potential between the working electrode and the solution, and the polarization effects.

Figure 4-12 shows the plots of the threshold voltages V_T^p and V_T^n *vs.* E_{WR} for the PbPc and TiOPc transistors. It is clear that V_T^p or V_T^n exhibits a linear relation against E_{WR}, for the two OTFTs; it is likely that the EDL-OTFT threshold voltages are regulated by the E_{WR} of the ionic liquids. This indicates that both the electrochemical potential of the ionic liquid and the polarization at the interface would affect the carrier injection to the semiconductor. The red broken lines in Figure 4-12 exhibit the slopes of 1.29 and 2.58 for V_T^p and V_T^n in the PbPc EDL-OTFTs. The blue lines for the TiOPc EDL-OTFTs exhibit the slopes of 1.38 and 1.96 for V_T^p and V_T^n, respectively. These values are larger than 1, and the slope of V_T^n is larger than that of V_T^p. These results are consistent with the discussion on the relation between V_T^p and V_T^n in Figure 4-11.

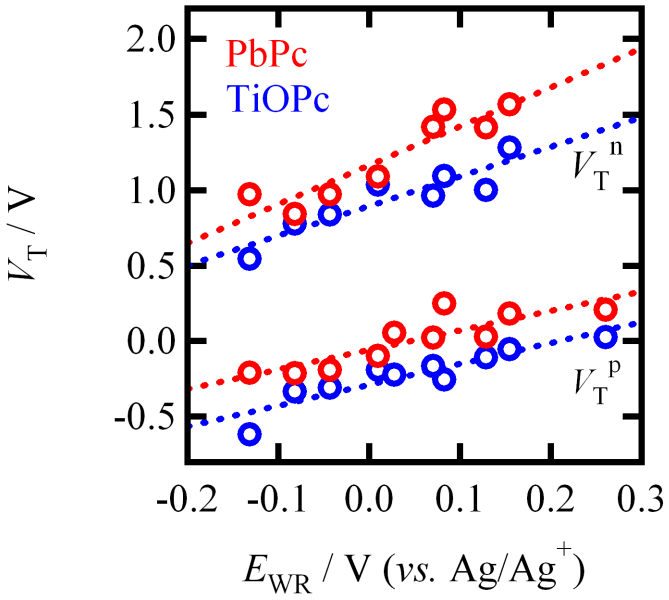

Figure 4-12. Threshold voltages V_T *vs.* electrochemical potentials between working and reference electrodes E_{WR} for ambipolar PbPc and TiOPc EDL-OTFTs with 10 kinds of ionic-liquid gate-dielectrics.

Figure 4-13 shows an energy level diagram for the frontier orbitals of PbPcs and TiOPc, and the electrochemical potential of an ionic liquid. The orbital energies of the MPcs were calculated by the DFT method. The HOMO-LUMO gaps of these two MPcs are nearly the same (~2.15 eV), and are lower than those of the other MPcs, such as CuPc and ZnPc (>2.2 eV). The LUMO and HOMO levels of PbPc are higher by 0.2 eV than the corresponding levels for TiOPc, respectively. The ambipolar behaviors of the TiOPc and PbPc transistors indicate that the electrochemical potentials of the ionic liquids, ψ_S, are located in the HOMO-LUMO energy gap of these MPcs. Since the hole injections are easier than the electron injections in the PbPc and TiOPc EDL-OTFTs, and the hole injection for PbPc is easier than that for TiOPc, the energy level of ψ_S is

thought to be closer to the HOMO of PbPc and the LUMO of TiOPc, as shown in Figure 4-13. It is easily concluded that the gate threshold voltages for the hole and electron injections are governed by the mutual relations among the HOMO and LUMO levels and the electrochemical potentials of the ionic liquids.

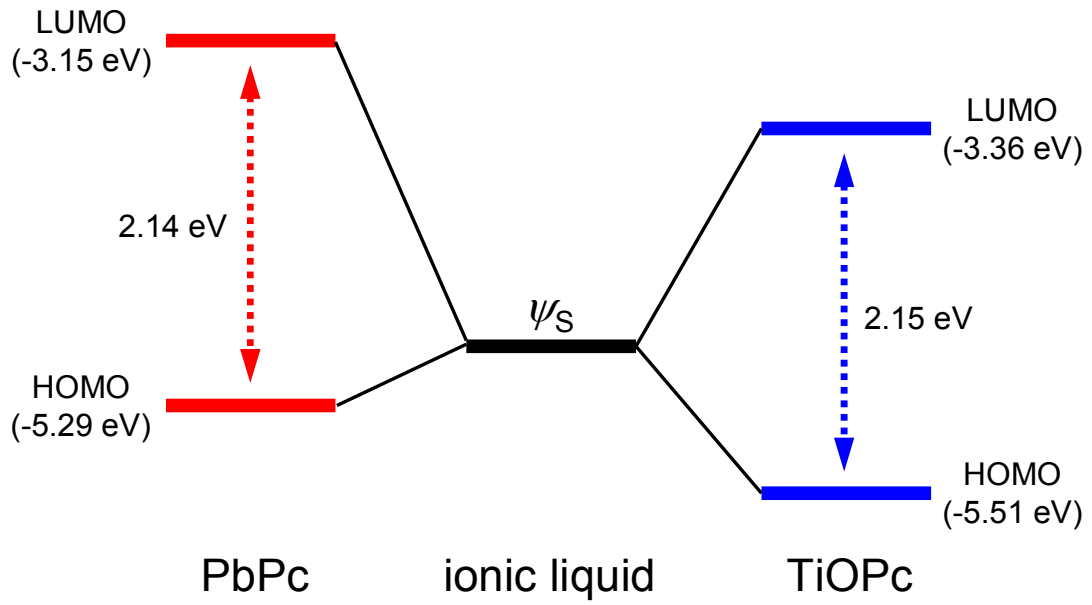

Figure 4-13. Energy level diagram between MPcs and electrochemical potential of ionic liquid. The HOMO and LUMO energies of MPcs are calculated by the DFT B3LYP method with a LanL2DZ basis set.

4-4. Conclusion

Porphyrazine-based EDL-OTFTs and complementary OTFT inverters have been demonstrated, taking advantage of the fact that MPc (M = H_2 and VO) and MTTDP (M = H_2 and VO) are *p*- and *n*-type semiconductors, respectively, with similar transport properties, and that their thin films are stable, even in ionic liquids. By using ionic-liquid gate-dielectrics, a low voltage operation of the organic inverter was demonstrated, which was maintained up to a relatively high frequency of 20 Hz.

Ambipolar EDL-OTFTs of ionic-liquid gate-dielectrics using MPcs (M = Pb and TiO) as active semiconductors have been also demonstrated. These OTFTs have shown ambipolar transport with low threshold voltages. The difference between the threshold gate voltages of the hole and electron injections depends little on the ionic liquids, but the voltages are proportional to the electrochemical potentials of the ionic liquids. This dependence can be understood in terms of the mutual relations among the HOMO and LUMO levels of PbPc and TiOPc, and the electrochemical potentials of the ionic liquids.

Chapter 5
Conclusion

A number of important unanswered questions with respect to octathio[8]circulene (**1**) were investigated during the course of this thesis. The high symmetry and released anti-aromaticity characteristics of compound **1** were revealed by single-crystal X-ray analysis. The thin film of **1** fabricated by vacuum deposition, which had a highly oriented structure with a relatively smooth surface, was characterized. The thin-film electrochemistry in ionic liquid revealed the highly degenerated state of compound **1**. The semiconductive behavior of **1** was analyzed with temperature-dependent conductivity and OTFT measurements, and chemical doping with iodine or TCNQ molecules yielded a conductivity enhancement on the order of $10^3 \sim 10^5$, which is comparable to the results of a charge injection from OTFTs.

The strong intermolecular sulfur-sulfur interactions allowed us to apply **1** to the active layer of EDL-OTFTs. By using ionic liquids for gate-dielectrics, the thin film of **1** shows stable EDL-OTFTs performance with high mobility and low threshold voltage. The gate material-dependences for the oxidation potential, threshold voltage and mobility of the thin film of **1** were demonstrated by using six kinds of ionic liquid, and their potential controlling factors were investigated.

In addition to compound **1**, the study of EDL-OTFT was extended for other robust, structured organic compounds, such as the porphyrazine derivatives Pc and TTDPz, which allowed us to perform the EDL-OTFTs operation in ionic-liquid. The MTTDPzs (M = H_2 and VO) have shown *n*-type behavior, while MPcs (M = H_2 and VO) exhibit *p*-type behavior. The combination of these *p*- and *n*-type materials can be used to

fabricate the complementary inverter circuit. The demonstration of these inverters indicated that they have great potential for practical use with high gain and a low applied voltage below 2.0 V. The low band-gap MPcs (M = Pb and TiO) have shown ambipolar EDL-OTFTs performances. The threshold voltages of these ambipolar materials have shown ionic-liquid dependences. The electrochemical potentials of ionic liquids are governed by their anion component.

In summary, the robust structured organic compound including heteroatoms have shown interesting electronic and physical properties. A combination of robust organic thin films and ionic liquids allowed easy fabrication of an organic logic device with low power operation.

Appendix

Theoretical Calculation of Molecular Orbitals[199]

Table A-1. Optimized coordinates of compound **1** in neutral state $\mathbf{1}^0$.

label	element	x	y	z
1	C	-1.492580	-1.110078	0.000109
2	C	-1.840388	0.270470	-0.000075
3	C	-1.110078	1.492580	0.000097
4	C	0.270470	1.840388	-0.000084
5	C	1.492580	1.110078	0.000117
6	C	1.840388	-0.270470	-0.000078
7	C	1.110078	-1.492580	0.000081
8	C	-0.270470	-1.840388	-0.000103
9	C	-2.599077	-1.933104	0.000159
10	C	-3.204774	0.470968	-0.000106
11	C	-1.933104	2.599077	0.000082
12	C	0.470968	3.204773	-0.000088
13	C	2.599077	1.933104	0.000178
14	C	3.204774	-0.470968	-0.000120
15	C	1.933104	-2.599077	0.000051
16	C	-0.470968	-3.204773	-0.000161
17	S	-4.119413	-1.037843	0.000069
18	S	-3.646732	2.179096	-0.000071
19	S	-1.037843	4.119413	-0.000076
20	S	2.179096	3.646732	0.000175
21	S	4.119413	1.037843	-0.000025
22	S	3.646732	-2.179096	-0.000025
23	S	1.037843	-4.119413	-0.000134
24	S	-2.179097	-3.646732	0.000064

Table A-2. Optimized coordinates of compound **1** in one electron oxidation state $\mathbf{1}^+$.

label	element	x	y	z
1	C	1.831743	-0.261120	0.000055
2	C	1.112006	-1.474684	-0.000071
3	C	-0.263931	-1.826254	0.000118
4	C	-1.483170	-1.103135	-0.000051
5	C	-1.831743	0.261120	0.000071
6	C	-1.112006	1.474684	-0.000077
7	C	0.263931	1.826254	0.000093
8	C	1.483170	1.103135	-0.000071
9	C	3.215772	-0.460394	-0.000024
10	C	1.940159	-2.584340	-0.000053
11	C	-0.458934	-3.190256	0.000118
12	C	-2.594759	-1.938700	-0.000013
13	C	-3.215772	0.460394	0.000013
14	C	-1.940159	2.584340	-0.000063
15	C	0.458934	3.190256	0.000072
16	C	2.594759	1.938700	-0.000036
17	S	3.665507	-2.153912	-0.000074
18	S	1.054556	-4.090106	0.000048
19	S	-2.173099	-3.631414	0.000112
20	S	-4.129299	-1.045456	-0.000065
21	S	-3.665507	2.153912	0.000017
22	S	-1.054556	4.090106	-0.000076
23	S	2.173099	3.631414	0.000099
24	S	4.129299	1.045456	-0.000090

Table A-3. Optimized coordinates of compound **1** in two electron oxidation state $\mathbf{1}^{2+}$.

label	element	x	y	z
1	C	-1.837325	0.000661	0.000603
2	C	-1.298905	1.299830	0.000359
3	C	0.000666	1.837893	0.000539
4	C	1.299844	1.298882	0.000412
5	C	1.837324	-0.000677	0.000549
6	C	1.298913	-1.299818	0.000383
7	C	-0.000666	-1.837889	0.000591
8	C	-1.299854	-1.298869	0.000355
9	C	-3.234126	0.001152	0.000135
10	C	-2.286371	2.287026	0.000062
11	C	0.001154	3.233935	0.000064
12	C	2.288007	2.285381	0.000096
13	C	3.234124	-0.001171	0.000104
14	C	2.286404	-2.287035	0.000094
15	C	-0.001155	-3.233891	0.000117
16	C	-2.288040	-2.285387	0.000073
17	S	-3.915880	1.623810	-0.000184
18	S	-1.621106	3.917129	-0.000253
19	S	1.623915	3.915964	-0.000246
20	S	3.917030	1.621015	-0.000196
21	S	3.915914	-1.623844	-0.000195
22	S	1.621127	-3.917101	-0.000197
23	S	-1.623932	-3.915933	-0.000237
24	S	-3.917066	-1.621049	-0.000193

Table A-4. Optimized coordinates of compound **2**.

label	element	x	y	z
1	C	-1.574048	0.722731	-0.426941
2	C	-1.574589	-0.721559	-0.426936
3	C	-0.722739	-1.574054	0.426902
4	C	0.721551	-1.574596	0.426920
5	C	1.574061	-0.722731	-0.426888
6	C	1.574603	0.721559	-0.426883
7	C	0.722723	1.574055	0.426925
8	C	-0.721567	1.574595	0.426897
9	C	-2.514031	1.236069	-1.282057
10	C	-2.514948	-1.234198	-1.282058
11	C	-1.236091	-2.514052	1.281994
12	C	1.234176	-2.514971	1.282033
13	C	2.514076	-1.236069	-1.281970
14	C	2.514993	1.234198	-1.281971
15	C	1.236047	2.514055	1.282031
16	C	-1.234220	2.514968	1.281995
17	H	-2.717516	2.276768	-1.482450
18	H	-2.719201	-2.274746	-1.482457
19	H	-2.276793	-2.717539	1.482368
20	H	2.274721	-2.719228	1.482444
21	H	2.717566	-2.276769	-1.482357
22	H	2.719251	2.274746	-1.482364
23	H	2.276743	2.717544	1.482437
24	H	-2.274771	2.719224	1.482375
25	S	-3.408242	0.001267	-2.097283
26	S	-0.001303	-3.408275	2.097226
27	S	3.408313	-0.001267	-2.097166
28	S	0.001232	3.408275	2.097226

Table A-5. Optimized coordinates of PbPc.

label	element	x	y	z
1	Pb	0.000035	0.000000	1.251170
2	N	-0.001782	2.034185	0.106315
3	N	2.034105	0.001731	0.106386
4	N	0.001680	-2.034185	0.106314
5	N	-2.034179	-0.001731	0.106172
6	N	2.411089	2.415212	-0.118333
7	N	2.415191	-2.411111	-0.118333
8	N	-2.411092	-2.415182	-0.118688
9	N	-2.415193	2.411081	-0.118689
10	C	-1.136204	2.819689	-0.086678
11	C	1.131344	2.821549	-0.086524
12	C	2.819642	1.136165	-0.086306
13	C	2.821564	-1.131371	-0.086300
14	C	1.136139	-2.819627	-0.086529
15	C	-1.131410	-2.821611	-0.086672
16	C	-2.819644	-1.136168	-0.086758
17	C	-2.821566	1.131375	-0.086754
18	C	-0.714066	4.201361	-0.345070
19	C	0.706962	4.202544	-0.344972
20	C	1.432561	5.377711	-0.595802
21	C	0.704340	6.558612	-0.832116
22	C	-0.715246	6.557433	-0.832239
23	C	-1.441560	5.375332	-0.596040
24	C	4.201298	0.714085	-0.344796
25	C	4.202501	-0.706947	-0.344793
26	C	5.377694	-1.432502	-0.595762
27	C	6.558553	-0.704251	-0.832047
28	C	6.557353	0.715360	-0.832056
29	C	5.375265	1.441619	-0.595775
30	C	0.714099	-4.201341	-0.344977
31	C	-0.706929	-4.202563	-0.345065
32	C	-1.432442	-5.377761	-0.596022
33	C	-0.704139	-6.558633	-0.832229
34	C	0.715447	-6.557411	-0.832127
35	C	1.441678	-5.375281	-0.595819
36	C	-4.201395	-0.714084	-0.344928
37	C	-4.202598	0.706947	-0.344922
38	C	-5.377822	1.432499	-0.595596
39	C	-6.558751	0.704237	-0.831661
40	C	-6.557550	-0.715345	-0.831674
41	C	-5.375392	-1.441616	-0.595617
42	H	2.518124	5.365340	-0.604185
43	H	1.233414	7.489470	-1.021570
44	H	-1.245830	7.487410	-1.021800
45	H	-2.527099	5.361173	-0.604622
46	H	5.365335	-2.518064	-0.604220
47	H	7.489423	-1.233275	-1.021584
48	H	7.487326	1.245954	-1.021609
49	H	5.361058	2.527159	-0.604254
50	H	-2.518004	-5.365451	-0.604582
51	H	-1.233152	-7.489508	-1.021772
52	H	1.246092	-7.487372	-1.021596
53	H	2.527218	-5.361062	-0.604224
54	H	-5.365483	2.518062	-0.604071
55	H	-7.489649	1.233280	-1.021003
56	H	-7.487551	-1.245959	-1.021034
57	H	-5.361204	-2.527156	-0.604116

Table A-6. Optimized coordinates of TiOPc.

label	element	x	y	z
1	Ti	-0.000009	0.000000	0.638213
2	O	-0.000034	-0.000002	2.276361
3	N	-0.074446	1.998074	0.075824
4	N	1.998072	0.074444	0.075852
5	N	0.074443	-1.998074	0.075822
6	N	-1.998075	-0.074444	0.075792
7	N	2.320088	2.499668	-0.02412
8	N	2.499668	-2.320088	-0.024123
9	N	-2.320088	-2.499668	-0.024197
10	N	-2.499668	2.320088	-0.024193
11	C	-1.238981	2.768252	-0.003665
12	C	1.029551	2.852766	-0.003631
13	C	2.768252	1.238981	-0.003602
14	C	2.852766	-1.029552	-0.003604
15	C	1.238982	-2.768252	-0.003635
16	C	-1.029552	-2.852766	-0.003669
17	C	-2.768252	-1.238982	-0.003688
18	C	-2.852766	1.029552	-0.003687
19	C	-0.865758	4.178881	-0.106321
20	C	0.552418	4.231714	-0.106249
21	C	1.235406	5.454704	-0.202759
22	C	0.463743	6.627115	-0.294308
23	C	-0.955443	6.574243	-0.294416
24	C	-1.637792	5.347688	-0.202952
25	C	4.178883	0.865759	-0.106232
26	C	4.231717	-0.552417	-0.106184
27	C	5.454709	-1.235403	-0.202677
28	C	6.627122	-0.463739	-0.294186
29	C	6.574250	0.955448	-0.294271
30	C	5.347693	1.637795	-0.202822
31	C	0.865760	-4.178880	-0.106304
32	C	-0.552415	-4.231714	-0.106277
33	C	-1.235400	-5.454704	-0.202812
34	C	-0.463734	-6.627115	-0.294340
35	C	0.955452	-6.574243	-0.294402
36	C	1.637798	-5.347688	-0.202913
37	C	-4.178880	-0.865759	-0.106362
38	C	-4.231713	0.552417	-0.106313
39	C	-5.454703	1.235403	-0.202845
40	C	-6.627113	0.463739	-0.294395
41	C	-6.574241	-0.955448	-0.294481
42	C	-5.347686	-1.637795	-0.202994
43	H	2.320544	5.484200	-0.203172
44	H	0.957577	7.592992	-0.366107
45	H	-1.519748	7.500709	-0.366299
46	H	-2.722118	5.296390	-0.203509
47	H	5.484205	-2.320541	-0.203108
48	H	7.593000	-0.957571	-0.365971
49	H	7.500716	1.519755	-0.366123
50	H	5.296394	2.722123	-0.203363
51	H	-2.320538	-5.484200	-0.203259
52	H	-0.957566	-7.592991	-0.366156
53	H	1.519760	-7.500707	-0.366271
54	H	2.722124	-5.296389	-0.203437
55	H	-5.484198	2.320541	-0.203274
56	H	-7.592988	0.957572	-0.366210
57	H	-7.500704	-1.519754	-0.366366
58	H	-5.296388	-2.722121	-0.203535

References

[1] H. Akamatsu, H. Inokuchi, Y. Matsunaga, *Nature* **1954**, *173*, 168–169.

[2] J. Ferraris, D. O. Cowan, V. Walatka, J. H. Perlstein, *J. Am.Chem. Soc.* **1973**, *95*, 948–949.

[3] M. J. Cohen, L. B. Coleman, A. F. Garito, A. J. Heeger, *Phys. Rev. B* **1974**, *10*, 1298–1307.

[4] A. F. Garito, A. J. Heeger, *Acc. Chem. Res.* **1974**, *7*, 232–249.

[5] J. B. Torrance, *Acc. Chem. Res.* **1979**, *12*, 79–86.

[6] G. Saito, Y. Yoshida, *Bull. Chem. Soc. Jpn.* **2007**, *80*, 1–137.

[7] J. P. Ferraris, T. F. Finnegan, *Solid State Commun.* **1976**, *18*, 1169–1172.

[8] S. Kagoshima, H. Anzai, K. Kajimura, T. Ishiguro, *J. Phys. Soc. Jpn.* **39**, *1975*, 1143–1144.

[9] D. Jerome, A. Mazaud, M. Ribault, K. Bechgaard, *J. Phys. Lett.* **1980**, *41*, L95–L98.

[10] G. Saito, T. Enoki, K. Toriumi, H. Inokuchi, *Solid State Commun.* **1982**, *42*, 557–560.

[11] J. Roncali, *Chem. Rev.* **1992**, *92*, 711–738.

[12] H. S. O. Chan, S. C. Ng, *Prog. Polym. Sci.***1998**, *23*, 1167–1231.

[13] T. Torroba, M. Garcia–Valverde, *Angew. Chem. Int. Ed.* **2006**, *45*, 8092–8096.

[14] K. Takimiya, Y. Kunugi, T. Otsubo, *Chem. Lett.* **2007**, *36*, 578–583.

[15] A. Patra, Y. H. Wijsboom, L. J. W. Shimon, M. Bendikov, *Angew. Chem. Int. Ed.* **2007**, *46*, 8814–8818.

[16] H. Hart , M. Sasaoka, *J. Am. Chem. Soc.* **1978**, *100*, 4326–4327.

[17] M. K. Shepherd, *J. Chem. Soc., Perkin Trans.* **1988**, *1*, 961–969.

[18] Y. Kono, H. Miyamoto, Y. Aso, T. Otsubo, F. Ogura, T. Tanaka, M. Sawada, *Angew. Chem. Int. Ed.* **1989**, *28*, 1222–1224.

[19] T. Otsubo, Y. Kono, N. Hozo, H. Miyamoto, Y. Aso, F. Ogura, T. Tanaka, M. Sawada, *Bull. Chem. Soc. Jpn.* **1993**, *66*, 2033–2041.

[20] L. K. Hansen, A. Hordvik, *J. Chem. Soc., Chem. Commun.* **1974**, 800–801.

[21] J. P. Brown, T. B. Gay, *J. Chem. Soc., Perkin Trans.* **1974**, *1*, 866–868.

[22] K. Oyaizu, T. Iwasaki, Y. Tsukahara, E. Tsuchida, *Macromolecules* **2004**, *34*, 1257–1270.

[23] A. Rajca, M. Miyasaka, M. Pink, H. Wang, S. Rajca, *J. Am. Chem. Soc.* **2004**, *126*, 15211–15222.

[24] K. Y. Chernichenko, V. V. Sumerin, R. V. Shpanchenko, E. S. Balenkova, V. G. Nenajdenko, *Angew. Chem. Int. Ed.* **2006**, *45*, 7367–7370.

[25] A. Dadvand, F. Cicoira, K. Y. Chernichenko, E. S. Balenkova, R. M. Osuna, F. Rosei, V. G. Nenajdenko, D. F. Perepichka, *Chem. Commun.* **2008**, 5354–5356.

[26] G. Horowitz, *Adv. Mater.* **1998**, *10*, 365–377.

[27] J. Zaumseil, H. Sirringhaus, *Chem. Rev.* **2007**, *107*, 1296–1323.

[28] P. Abhishek, C. J. Kulkarni, A. B. Tonzola, A. J. Samson, *Chem. Mater.* **2004**, *16*, 4556–4573.

[29] H. Hoppe, N. S. Sariciftci, *J. Mater. Res.* **2004**, *19*, 1924–1945.

[30] J. E. Anthony, *Chem. Rev.* **2006**, *106*, 5028–5048.

[31] G. Horowitz, X. Z. Peng, D. Fichou, F. Garnier, *J. Mol. Electron.* **1991**, *7*, 85–89.

[32] V. Podzorov, V. M. Pudalov, M. E. Gershenson, *Appl. Phys. Lett.* **2003**, *82*, 1739.

[33] A. L. Briseno, R. J. Tseng, M. M. Ling, E. H. L. Falcao, Y. Yang , F. Wudl, Z. Bao, *Adv. Mater.* **2006**, *18*, 2320–2324.

[34] J. Takeya, M. Yamagishi, Y. Tominari, R. Hirahara, Y. Nakazawa, T. Nishikawa, T. Kawase, T. Shimoda, S. Ogawa, *Appl. Phys. Lett.* **2007**, *90*, 102120.

[35] A. L. Briseno, S. C. B. Mannsfeld, M. M. Ling, S. Liu, R. J. Tseng, C. Reese, M. E. Roberts, Y. Yang, F. Wudl, Z. Bao, *Nature* **2006**, *444*, 913–917.

[36] R. C. Haddon, A. S. Perel, R. C. Morris, T. T. M. Palstra, A. F. Hebard, R. M. Fleming, *Appl. Phys. Lett.* **1995**, *67*, 121.

[37] T. D. Anthopoulos, B. Singh, N. Marjanovic, N. S. Sariciftci, A. M. Ramil, H. Sitter, M. Cölle, D. M. Leeuw, *Appl. Phys. Lett.* **2006**, *89*, 213504.

[38] P. H. Wöbkenberg, D. D.C. Bradley, David Kronholm, J. C. Hummelen, D. M. de Leeuw, M. Cölle, T. D. Anthopoulos, *Synt. Met.* **2008**, *158*, 468–472.

[39] J. Veres, S. Ogier, G. Lloyd, D. Leeuw, *Chem. Mater.* **2004**, *16*, 4543–4555.

[40] A. Facchetti, M.H. Yoon, T. J. Marks, *Adv. Mater.* **2005**, *17*, 1705–1725.

[41] J. Robertson, *Rep. Prog. Phys.* **2006**, *69*, 327–396.

[42] J. Lee, M. J. Panzer, Y. He, T. P. Lodge, C. D. Frisbie, *J. Am. Chem. Soc.* **2007**, *129*, 4532–4533.

[43] K. Ueno, S. Nakamura, H. Shimotani, A. Ohtomo, N. Kimura, T. Nojima, H. Aoki, Y. Iwasa, M. Kawasaki, *Nature Mater.* **2008**, *7*, 855–858.

[44] A. S. Dhoot, J. D. Yuen, M. Heeney, I. McCulloch, D. Moses, A. J. Heeger, *Proc. Natl Acad. Sci.* **2006**, *103*, 11834–11837.

[45] H. Klauk, *Chem. Soc. Rev.* **2010**, *39*, 2643–2666.

[46] M. C. Buzzeo, R. G. Evans, R. G. Compton, *ChemPhysChem* **2004**, *5*, 1106–1120.

[47] C. Chiappe, D. Pieraccini, *J. Phys. Org. Chem.* **2005**, *18*, 275–297.

[48] F. Endres, S. Z. E. Abedin, *Phys. Chem. Chem. Phys.* **2006**, *8*, 2101–2116

[49] N. V. Plechkova, K. R. Seddon, *Chem. Soc. Rev.* **2008**, *37*, 123–150.

[50] R. Hagiwara, Y. Ito, *J. Fluorine Chem.* **2000**, *105*, 221–227

[51] M. Galiński1, A. Lewandowski, I. Stępniak, *Electrochimica Acta* **2006**, *51*, 5567–5580.

[52] L. A. Blanchard, D. Hancu, E. J. Beckman, J. F. Brennecke, *Nature* **1999**, *399*, 28–29.

[53] M. J. Earle, K. R. Seddon, *Pure Appl. Chem.* **2000**, *72*, 1391–1398.

[54] J. S. Wilkes, *Green Chem.* **2002**, *4*, 73–80.

[55] M. Ue, M. Takeda, A. Toriumi, A. Kominato, R. Hagiwara, Y. Ito, *J. Electrochem. Soc.* **2003**, *150*, A499–A502.

[56] T. Sato, G. Masuda, K. Takagi, *Electrochim. Acta* **2004**, *49*, 3603–3611.

[57] H. Matsumoto, H. Sakaebe, K. Tatsumi, *J. Power Sources* **2005**, *146*, 45–50.

[58] A. Lewandowski, A. Świderska–Mocek, *J. Power Sources* **2009**, *194*, 601–609.

[59] M. Armand, F. Eendres, D. R. MacFarlane, H. Ohno, B. Scrosati, *Nature Mater.* **2009**, *8*, 621–629.

[60] P. Wang, S. M. Zakeeruddin, P. Comte, I. Exnar, M. Grätzel, *J. Am. Chem. Soc.* **2003**, *125*, 1166–1167.

[61] R. Kawano, H. Matsui, C. Matsuyama, A. Sato, M. Susan, N. Tanabe, M. Watanabe, *J. Photochem. Photobiol. A: Chem.* **2004**, *164*, 87–92.

[62] S. M. Zakeeruddin, M. Grätzel, *Adv. Funct. Mater.* **2009**, *19*, 2187–2202.

[63] R. F. Souza, J. C. Padilha, R. S. Gonçalves, J. Dupont, *Electrochem. Commun.* **2003**, *5*, 728–731.

[64] H. Nakamoto, M. Watanabe, *Chem. Commun.* **2007**, 2539–2541.

[65] W. Lu, A. G. Fadeev, B. Qi, E. Smela, B. R. Mattes, J. Ding, G. M. Spinks, J. Mazurkiewicz, D. Zhou, G. G. Wallace, D. R. MacFarlane, S. A. Forsyth, M. Forsyth, *Science* **2002**, *297*, 983–987.

[66] T. Fukushima, K. Asaka, A. Kosaka, T. Aida, *Angew. Chem. Int. Ed.* **2005**, *44*, 2410–2413.

[67] R. Marcilla, F. Alcaide, H. Sardon, J. A. Pomposo, C. Pozo–Gonzalo, D. Mecerreyes, *Electrochem. Commun.* **2006**, *8*, 482–488.

[68] R. Misra, M. McCarthy, A. F. Hebard, *Appl. Phys. Lett.* **2007**, *90*, 052905.

[69] H. Yuan, H. Shimotani, A. Tsukazaki, A. Ohtomo, M. Kawasaki, Y. Iwasa, *Adv. Funct. Mater.* **2009**, *19*, 1046–1053.

[70] M. S. Kang, A. Sahu, D. J. Norris, C. D. Frisbie, *Nano Lett.* **2010**, *10*, 3727–3732.

[71] J. T. Ye, S. Inoue, K. Kobayashi, Y. Kasahara, H. T. Yuan, H. Shimotani, Y. Iwasa, *Nature Mater.* **2010**, *9*, 125–128.

[72] K. Ueno, S. Nakamura, H. Shimotani, H. T. Yuan, N. Kimura, T. Nojima, H. Aoki, Y. Iwasa, M. Kawasaki, *Nature Nanotech.* **2011**, *6*, 408–412.

[73] Y. Yamada, K. Ueno, T. Fukumura, H. T. Yuan, H. Shimotani, Y. Iwasa, L. Gu, S. Tsukimoto, Y. Ikuhara, M. Kawasaki, *Science* **2011**, *332*, 1065–1067.

[74] B. D. Paulsen, C. D. Frisbie, *J. Phys. Chem. C* **2012**, *116*, 3132–3141.

[75] F. Chen, Q. Qing, J. Xia, J. Li, N. Tao, *J. Am. Chem. Soc.* **2009**, *131*, 9908–9909.

[76] H. Okimoto, T. Takenobu, K. Yanagi, Y. Miyata, H. Shimotani, H. Kataura, Y. Iwasa, *Adv. Mater.* **2010**, *22*, 3981–3986.

[77] S. Ono, S. Seki, R. Hirahara, Y. Tominari, J. Takeya, *Appl. Phys. Lett.* **2008**, *92*, 103313.

[78] T. Uemura, M. Yamagishi, S. Ono, J. Takeya, *Jpn. J. Appl. Phys.* **2010**, *49*, 01AB13.

[79] W. Xie, C. D. Frisbie, *J. Phys. Chem. C* **2011**, *115*, 14360–14368.

[80] Y. Kaji, K. Ogawa, R. Eguchi, H. Goto, Y. Sugawara, T. Kambe, K. Akaike, S. Gohda, A. Fujiwara, Y. Kubozono, *Org. Electron.* **2011**, *12*, 2076–2083.

[81] C. Wakai, A. Oleinikova, M. Ott, H. Weingärtner, *J. Phys. Chem. B* **2005**, *109*, 17028–17030.

[82] C. Daguenet, P. J. Dyson, I. Krossing, A. Oleinikova, J. Slattery, C. Wakai, H. Weingärtner, *J. Phys. Chem. B* **2006**, *110*, 12682–12688.

[83] H. Weingärtner, P. Sasisanker, C. Daguenet, P. J. Dyson, I. Krossing, J. M. Slattery, T. Schubert, *J. Phys. Chem. B* **2007**, *111*, 4775–4780.

[84] J. Hunger, A. Stoppa, S. Schrödle, G. Hefter, R. Buchner, *ChemPhysChem* **2009**, *10*, 723–733.

[85] A. I. Kingon, J. Maria, S. K. Streiffer, *Nature* **2000**, *406*, 1032–1038.

[86] M. S. Kang, J. Lee, D. J. Norris, C. D. Frisbie, *Nano Lett.* **2009**, *9*, 3848–3852.

[87] H. T. Yuan, M. Toh, K. Morimoto, W. Tan, F. Wei, H. Shimotani, C. Kloc, Y. Iwasa, *Appl. Phys. Lett.* **2011**, *98*, 012102.

[88] Y. Onose, R. Yoshimi, A. Tsukazaki, H. Yuan, T. Hidaka, Y. Iwasa, M. Kawasaki, Y. Tokura, *Appl. Phys. Express* **2011**, *4*, 083001.

[89] H. Shimotani, H. Asanuma, J. Takeya, Y. Iwasa, *Appl. Phys. Lett.* **2006**, *89*, 203501.

[90] J. Takeya, K. Yamada, K. Hara, K. Shigeto, K. Tsukagoshi, S. Ikehata, Y. Aoyagi, *Appl. Phys. Lett.* **2006**, *88*, 112102.

[91] G. Cellere, A. Paccagnella, A. Mazzocchi, M. G. Valentini, *IEEE Trans. Electron Devices* **2005**, *52*, 211–217.

[92] S. Lombardo, J. H. Stathis, B. P. Linder, K. L. Pey, F. Pa–lumbo, C. H. Tung, *J. Appl. Phys.* **2005**, *98*, 121301.

[93] Z. Zhou, T. Yamamoto, *J. Organomet. Chem.* **1991**, *414*, 119–127.

[94] H. Irngartinger, U. Huber–Patz, H. Rodewald, *Acta Crystallogr. Sect. C* **1985**, *41*, 1088–1089.

[95] A. D. Becke, *J. Chem. Phys.* **1993**, *98*, 5648.

[96] P. R. Schleyer, C. Maerker, A. Dransfeld, H. Jiao, N. J. R. E. Hommes, *J. Am. Chem. Soc.* **1996**, *118*, 6317–6318.

[97] Z. Chen, C. S. Wannere, C. Corminboeuf, R. Puchta, P. R. Schleyer, *Chem. Rev.* **2005**, *105*, 3842–3888.

[98] P. R. Schleyer, H. Jiao, N. J. R. E. Hommes, V. G. Malkin, O. L. Malkina, *J. Am. Chem. Soc.* **1997**, *119*, 12669–12670.

[99] P. R. Schleyer, M. Manoharan, Z. X. Wang, B. Kiran, H. Jiao, R. Puchta, N. J. R. E. Hommes, *Org. Lett.* **2001**, *3*, 2465–2468.

[100] H. Fallah–Bagher–Shaidaei, C. S. Wannere, C. Corminboeuf, R. Puchta, P. R. Schleyer, *Org. Lett.* **2006**, *8*, 863–866.

[101] J. Kruszewski, T. M. Krygowski, *Tetrahedron Lett.* **1972**, *36*, 3839–3842.

[102] T. M. Krygowski, *J. Chem. Inf. Comput. Sci.* **1993**, *33,* 70–78.

[103] R. D. Gould, *Coord. Chem. Rev.* **1996**, *156*, 237–274.

[104] S. E. Fritz, S. M. Martin, C. D. Frisbie, M. D. Ward, M. F. Toney, *J. Am. Chem. Soc.* **2004**, *126*, 4084–4085.

[105] T. J. Marks, J. G. Gaudiello, G. E. Kellogg, S. M. Tetrick, *ACS Symp. Ser.* **1988**, *360*, 224–237.

[106] R. J. Mortimer, *Chem. Soc. Rev.* **1997**, *26*, 147–156.

[107] N. Toshima, S. Kawamura, T. Tominaga, *Chem. Lett.* **1993**, *22*, 1299–1302.

[108] N. Toshima, T. Tominaga, S. Kawamura, *Bull. Chem. Soc. Jpn.* **1996**, *69*, 245–253.

[109] N. Toshima, T. Tominaga, *Bull. Chem. Soc. Jpn.* **1996**, *69*, 2111–2122.

[110] J. L. Kahl, L. R. Faulkner, K. Dwarakanath, H. Tachikawa, *J. Am. Chem. Soc.* **1986**, *108*, 5434–5440.

[111] J. M. Green, L. R. Faulknaer, *J. Am. Chem. Soc.* **1983**, *105*, 2950–2955.

[112] K. L. Brown, H. A. Mottola, *Langmuir* **1998**, *14*, 3411–3417.

[113] J. Silver, P. Lukes, A. Houlton, S. Howe, P. Hey, M. T. Ahmet, T. Mustafa, *J. Mater. Chem.* **1992**, *2*, 849–855.

[114] J. Silver, P. Lukes, P. Hey, M. T. Ahmet, *J. Mater. Chem.* **1992**, *2*, 841–847.

[115] Y. Miyoshi, M. Kubo, T. Fujinawa, Y. Suzuki, H. Yoshikawa, K. Awaga, *Angew. Chem. Int. Ed.* **2007**, *46*, 5532–5536.

[116] S. Seki, Y. Ohno, H. Miyashiro, Y. Kobayashi, A. Usami, Y. Mita, N. Terada, K. Hayamizu, S. Tsuzuki, M. Watanabe, *J. Electrochem. Soc.* **2008**, *155*, A421–A427.

[117] M. Kalaji, L. M. Peter, L. M. Abrantes, J. S.Mesquita, *J. Electroanal. Chem.* **1989**, *274*, 289–295.

[118] C. Odin, M. Nechtschein, *Synth. Met.* **1991**, *43*, 2943–2946.

[119] C. Barbero, R. Kötz, M. Kalaji, L. Nyholm, L. M. Peter, *Synth. Met.* **1993**, *55*, 1545–1551.

[120] K. Takahashi, *Pure Appl. Chem.* **1993**, *65*, 127–134.

[121] C. Kvarnström, H. Neugebauer, H. Kuzmany, H. Sitter, N. S. Sariciftci, *J. Electroanal. Chem.* **2001**, *511*, 13–19.

[122] H. Inokuchi, H. Kuroda, H. Akamatu, *Bull. Chem. Soc. Jpn.* **1961**, *34*, 749–753.

[123] M. A. Lampert, *Rep. Prog. Phys.* **1964**, *27*, 329–367.

[124] N. Amar, R. D. Gould, A. M. Saleh, *Vacuum* **1998**, *50*, 53–56.

[125] M. M. El–Nahass, A. M. Farid, A.A. Attia, H.A.M. Ali, *Appl. Surf. Sci.*, **2006**, *252*, 7553–7561.

[126] A. M. Saleh, A. K. Hassan, R. D. Gould, *J. Phys. Chem. Solids*, **2003**, *64*, 1297–1303.

[127] A. M. Saleh, A.O. Abu–Hilal, R.D. Gould, *Curr. Appl. Phys.* **2003**, *3*, 345–350.

[128] S. Senthilarasu, R. Sathyamoorthy, S. Lalitha, A. Subbarayan, *Solid–State Electron*, **2005**, *49*, 813–817.

[129] H. M. Zeyada, M. M. El–Nahass, *Appl. Surf. Sci.*, **2008**, *254*, 1852–1858.

[130] J. M. Marshall, *Rep. Prog. Phys.* **1983**, *46*, 1235–1282.

[131] G. Horowitz, P. Delannoy, *J. Appl. Phys.* **1991**, *70*, 469.

[132] R. J. Chesterfield, J. C. McKeen, C. R. Newman, P. C. Ewbank, D. A. S. Filho, J. L. Brédas, L. L. Miller, K. R. Mann, C. D. Frisbie, *J. Phys. Chem. B* **2004**, *108*, 19281–19292.

[133] D. Braga, G. Horowitz, *Adv. Mater.* **2009**, *21,* 1473–1486.

[134] V. Y. Butko, X. Chi, D. V. Lang, A. P. Ramirez, *Appl. Phys. Lett.* **2003**, *83*, 4773.

[135] K. Yamada, J. Takeya, K. Shigeto, K. Tsukagoshi, Y. Aoyagi, Y. Iwasa, *Appl. Phys. Lett.* **2006**, *88*, 122110.

[136] R. J. Chesterfield, J. C. McKeen, C. R. Newman, P. C. Ewbank, D. A. S. Filho, J. L. Brédas, L. L. Miller, K. R. Mann, C. D. Frisbie, *J. Phys. Chem. B* **2004**, *108*, 19281–19292

[137] H. Nakayama, J. Ye, T. Ohtani, Y. Fujikawa, K. Ando, Y. Iwasa, E. Saitoh, *Appl. Phys. Express* **2012**, *5*, 023002.

[138] K. Shimamura, D. Chiba, S. Ono, S. Fukami, N. Ishiwata, M. Kawaguchi, K. Kobayashi, T. Ono, *Appl. Phys. Lett.* **2012**, *100*, 122402.

[139] J. Lee, M. J. Panzer, Y. He, T. P. Lodge, C. D. Frisbie, *J. Am. Chem. Soc.* **2007**, *129*, 4532–4533.

[140] J. H. Cho, J. Lee, Y. He, B. S. Kim, T. P. Lodge, C. D. Frisbie, *Adv. Mater.* **2008**, *20*, 686–690.

[141] J. H. Cho, J. Lee, Y. Xia, B. Kim, Y. He, M. J. Renn, T. P. Lodge, C. D. Frisbie, *Nature Mater.* **2008**, *7*, 900–906.

[142] Y. Kaneko, K. Tsutsui, T. Tsukada, *J. Non–Cryst. Solids* **1992**, *149*, 264–268.

[143] J. B. Koo, K. S. Suh, I. K. You, S. H. Kim, *Jpn. J. Appl. Phys.* **2007**, *46*, 5062–5066.

[144] F. Maddalena, M. Spijkman, J. J. Brondijk, P. Fonteijn, F. Brouwer, J. C. Hummelen, D. M. Leeuw, P. W. M. Blom, B. Boer, *Org. Electron.* **2008**, *9*, 839–846.

[145] H. E. Katz, X. M. Hong, A. Dodabalapur, *J. Appl. Phys.* **2002**, *91*, 1572.

[146] G. Gu, M. G. Kane, J. E. Doty, A. H. Firester, *Appl. Phys. Lett.* **2005**, *87*, 243512.

[147] M. Kimura, T. Nakanishi, K. Nomura, T. Kamiya, H. Hosono, *Appl. Phys. Lett.* **2008**, *92*, 133512.

[148] M. Radosavljević, M. Freitag, K. V. Thadani, A. T. Johnson, *Nano Lett.* **2002**, *2*, 761–764.

[149] J. B. Cui, R. Sordan, M. Burghard, K. Kern, *Appl. Phys. Lett.* **2002**, *81*, 3260.

[150] M. Kalaji, L. M. Peter, L. M. Abrantes, J. S. Mesquita, *J. Electroanal. Chem.* **1989**, *274*, 289–295.

[151] C. Odin, M. Nechtschein, *Synth. Met.* **1991**, *41*, 2943–2946.

[152] C. Barbero, R. Kotz, M. Kalaji, L. Nyholm, L. M. Peter, *Synth. Met.* **1993**, *55*, 1545–1551.

[153] Y. Miyoshi, M. Kubo, T. Fujinawa, Y. Suzuki, H. Yoshikawa, K. Awaga, *Angew. Chem. Int. Ed.* **2007**, *46*, 5532–5536.

[154] M. Inagawa, H. Yoshikawa, T. Yokoyama, K. Awaga, *Chem. Commun.* **2009**, 3389–3391.

[155] J. Veres, S. D. Ogier, S. W. Leeming, D. C. Cupertino, S. M. Khaffaf, *Adv. Funct. Mater.* **2003**, *13*, 199–204.

[156] A. F. Stassen, R. W. I. Boer, N. N. Iosad, A. F. Morpurgo, *Appl. Phys. Lett.* **2004**, *85*, 3899.

[157] S. Ono, K. Miwa, S. Seki, J. Takeya, *Appl. Phys. Lett.* **2009**, *94*, 063301.

[158] T. Ernst, S. Cristoloveanu, G. Ghibaudo, T. Ouisse, S. Horiguchi, Y. Ono, Y. Takahashi, K. Murase, *IEEE Trans. Electron Devices* **2003**, *50*, 830–838.

[159] A. C. Arias, J. D. MacKenzie, I. McCulloch, J. Rivnay, A. Salleo, *Chem. Rev.* **2010**, *110*, 3–24.

[160] A. R. Brown, C. P. Jarrett, D. M. Leeuw, M. Matters, *Synth. Met.* **1997**, *88*, 37–55.

[161] H. Klauk, D. J. Gundlach, T. N. Jackson, *IEEE Electron Device Letters*, **1999**, *20*, 289–291.

[162] H. Klauk, M. Halik, U. Zschieschang, F. Eder, G. Schmid, C. Dehm, *Appl. Phys. Lett.* **2003**, *82*, 4175.

[163] B. Crone, A. Dodabalapur, Y. Y. Lin, R. W. Filas, Z. Bao, A. LaDuca, R. Sarpeshkar, H. E. Katz, W. Li, *Nature* **2000**, *403*, 521–523.

[164] E. J. Meijer, D. M. Leeuw, S. Setayesh, E. Veenendaal, B. H. Huisman, P. W. M. Blom, J. C. Hummelen, U. Scherf, T. M. Klapwijk, *Nature Mater.* **2003**, *2*, 678–682.

[165] M. H. Yoon, H. Yan, A. Facchetti, T. J. Marks, *J. Am. Chem. Soc.* **2005**, *127*, 10388–10395.

[166] M. Kitamura, Y. Arakawa, *Appl. Phys. Lett.* **2007**, *91*, 053505.

[167] H. Klauk, U. Zschieschang, J. Pflaum, M. Halik, *Nature*, **2007**, *445*, 745–748.

[168] H. Yan, Z. Chen, Y. Zheng, C. Newman, J. R. Quinn, F. Dötz, M. Kastler, A. Facchetti, *Nature*, **2009**, *457*, 679–686.

[169] T. Inabe, H. Tajima, *Chem. Rev.* **2004**, *104*, 5503–5534.

[170] M. V. Martínez–Díaz, G. Torre, T. Torres, *Chem. Commun.* **2010**, *46*, 7090–7108.

[171] G. Bottari, G. Torre, D. M. Guldi, T. Torresm, *Chem. Rev.* **2010**, *110*, 6768–6816.

[172] Z. Bao, A. J. Lovinger, A. Dodabalapur, *Adv. Mater.* **1997**, *9*, 42–44.

[173] P. A. Stuzhin, E. M. Bauer, C. Ercolani, *Inorg. Chem.* **1998**, *37*, 1533–1539.

[174] E. M. Bauer, D. Cardarrilli, C. Ercolani, P. A. Stuzhin, U. Russo, *Inorg. Chem.* **1999**, *38*, 6114–6120.

[175] M. P. Donzello, C. Ercolani, A. A. Gaberkorn, E. V. Kudrik, M. Meneghetti, G. Marcolongo, C. Rizzoli, P. A. Stuzhin, *Chem.–Eur. J.* **2003**, *9*, 4009–4024.

[176] E. V. Kudrik, E. M. Bauer, C. Ercolani, A. Chiesi–Villa, C. Rizzoli, A. Gaberkorn, P. A. Stuzhin, *Mendeleev Commun.* **2001**, *11*, 45–47.

[177] M. Fujimori, Y. Suzuki, H. Yoshikawa, K. Awaga, *Angew. Chem. Int. Ed.* **2003**, *42*, 5863–5868.

[178] Y. Suzuki, M. Fujimori, H. Yoshikawa, K. Awaga, *Chem. –Eur. J.* **2004**, *10*, 5158–5164.

[179] Y. Miyoshi, M. Kubo, T. Fujinawa, Y. Suzuki, H. Yoshikawa, K. Awaga, *Angew. Chem. Int. Ed.* **2007**, *46*, 5532–5536.

[180] H. Tada, H. Touda, M. Takada, K. Matsushige, *Appl. Phys. Lett.* **2000**, *76*, 873.

[181] T. Yasuda, T. Tsutsui, *Jpn. J. Appl. Phys.* **2006**, *45*, L595–L597.

[182] J. M. Assour, J. Goldmacher, S. E. Harrison, *J. Chem. Phys.* **1965**, *43*, 159–165.

[183] Y. Miyoshi, K. Takahashi, T. Fujimoto, H. Yoshikawa, M. M. Matsushita, Y. Ouchi, M. Kepenekian, V. Robert, M. P. Donzello, C. Ercolani, K. Awaga, *Inorg. Chem.* **2012**, *51*, 456–462.

[184] Z. Bao, A. J. Lovinger, J. Brown, *J. Am. Chem. Soc.* **1998**, *120*, 207–208.

[185] T. Sato, G. Masuda, K. Takagi, *Electrochimica Acta* **2004**, *49*, 3603–3611.

[186] K. R. Harris, M. Kanakubo, L. A.Woolf, *J. Chem. Eng. Data* **2007**, *52*, 1080–1085.

[187] D. Tomida, A. Kumagai, K. Qiao, C. Yokoyama, *Int. J. Thermophys.* **2006**, *27*, 39–47.

[188] M. L. Ge, R. S. Zhao, Y. F. Yi, Q. Zhang, L. S. Wang, *J. Chem. Eng. Data* **2008**, *53*, 2408–2411.

[189] C. Schreiner, S. Zugmann, R. Hartl, H. J. Gores, *J. Chem. Eng. Data* **2010**, *55*, 1784–1788.

[190] H. Matsumoto, M. Yanagida, K. Tanimoto, M. Nomura, Y. Kitagawa, Y. Miyazaki, *Chem. Lett.* **2000**, *29*, 922–923.

[191] H. Sakaebe, H. Matsumoto, *Electrochem. Commun.* **2003**, *5*, 594–598.

[192] D. R. MacFarlane, P. Meakin, J. Sun, N. Amini, M. Forsyth, *J. Phys. Chem. B* **1999**, *103*, 4164–4170.

[193] S. Trasatti, *J. Electroanal. Chem.* **1971**, *33*, 351–378.

[194] H. B. Michaelson, *J. Appl. Phys.* **1977**, *48*, 4729.

[195] S. Trasatti, *Pure & Appl. Chem.* **1986**, *58*, 955–966.

[196] W. N. Hansen, G. Hansen, *J. Phys. Rev. A* **1987**, *36*, 1396–1402.

[197] S.Trasatti, *Electrochim. Acta* **1990**, *35*, 269–271.

[198] S. Trasatti, *Electrochim. Acta* **1991**, *36*, 1657–1658.

[199] Gaussian 03, Revision D.01, M. J. Frisch, G. W. Trucks, H. B. Schlegel, G. E. Scuseria, M. A. Robb, J. R. Cheeseman, J. A. Montgomery, Jr., T. Vreven, K. N. Kudin, J. C. Burant, J. M. Millam, S. S. Iyengar, J. Tomasi, V. Barone, B. Mennucci, M. Cossi, G. Scalmani, N. Rega, G. A. Petersson, H. Nakatsuji, M. Hada, M. Ehara, K. Toyota, R. Fukuda, J. Hasegawa, M. Ishida, T. Nakajima, Y. Honda, O. Kitao, H. Nakai, M. Klene, X. Li, J. E. Knox, H. P. Hratchian, J. B. Cross, V. Bakken, C. Adamo, J. Jaramillo, R. Gomperts, R. E. Stratmann, O. Yazyev, A. J. Austin, R. Cammi, C. Pomelli, J. W. Ochterski, P. Y. Ayala, K. Morokuma, G. A. Voth, P. Salvador, J. J. Dannenberg, V. G. Zakrzewski, S. Dapprich, A. D. Daniels, M. C. Strain, O. Farkas, D. K. Malick, A. D. Rabuck, K. Raghavachari, J. B. Foresman, J. V. Ortiz, Q. Cui, A. G. Baboul, S. Clifford, J. Cioslowski, B. B. Stefanov, G. Liu, A. Liashenko, P. Piskorz, I. Komaromi, R. L. Martin, D. J. Fox, T. Keith, M. A. Al–Laham, C. Y. Peng, A. Nanayakkara, M. Challacombe, P. M. W. Gill, B. Johnson, W. Chen, M. W. Wong, C. Gonzalez, J. A. Pople, Gaussian, Inc., Wallingford CT, 2004.

Acknowledgements

First, I would like to gratefully thank Professor Kunio Awaga for his guidance and support throughout the course of this research. He introduced me to a very attractive scientific field: surface and solid state physics related to organic electronics. I am also indebted to Professors Hisanori Shinohara and Kazuhiko Seki for their support and comments.

I am extremely grateful to Professor Michio M. Matsushita for kindly instructing me in various experimental techniques, including device fabrications and measurements. I also appreciate the support and encouragement of Professor Yukio Ouchi, and his many valuable comments about ionic liquid and surface science.

Thanks also go to my friends, colleagues, and the department faculty and staff for making my time at Nagoya University such a great experience. I'd especially like to thank to Ms. Sayuri Handa, the secretary at Awaga Laboratory for supporting my research lives.

Finally, I offer my sincere thanks to all the members of Awaga Lab and my family.

Takuya Fujimoto

List of Publications

Supplemental Publications

[1] "Molecular, Crystal, and Thin-Film Structures of Octathio[8]circulene: Release of Anti-Aromatic Molecular Distortion and Lamellar Structure of Self-Assembling Thin Films"
T. Fujimoto, R. Suizu, H. Yoshikawa, K. Awaga
Chem. –Eur. J. **2008**, *14*, 6053–6056.

[2] "Electrochemical and Electrochromic Properties of Octathio[8]circulene Thin Films in Ionic Liquids"
T. Fujimoto, M. M. Matsushita, H. Yoshikawa, K. Awaga
J. Am. Chem. Soc. **2008**, *130*, 15790–15791.

[3] "Electrochemical field-effect transistors of octathio[8]circulene robust thin films with ionic liquids"
T. Fujimoto, M. M. Matsushita, K. Awaga
Chem. Phys. Lett. **2009**, *483*, 81–83.

[4] "Dual-gate field-effect transistors of octathio[8]circulene thin-films with ionic liquid and SiO_2 gate dielectrics"
T. Fujimoto, M. M. Matsushita, K. Awaga
Appl. Phys. Lett. **2010**, *97*, 123303.

[5] "A Complementary Organic Inverter of Porphyrazine Thin Films: Low-Voltage Operation Using Ionic Liquid Gate Dielectrics"
T. Fujimoto, Y. Miyoshi, M. M. Matsushita, K. Awaga
Chem. Commun. **2011**, *47*, 5837–5839.

[6] "Ionic-Liquid Component Dependence of Carrier Injection and Mobility for Electric-Double-Layer Organic Thin-Film Transistors"
T. Fujimoto, M. M. Matsushita, K. Awaga
J. Phys. Chem. C **2012**, *116*, 5240–5245.

References Publications

[1] “Photoconductivity and FET performance of an n-type porphyrazine semiconductor, tetrakis(thiadiazole)porphyrazine”
Y. Miyoshi, T. Fujimoto, H. Yoshikawa, M. M. Matsushita, K. Awaga, T. Yamada, H. Ito
Org. Electron. **2011**, *12*, 239–243.

[2] “Crystal Structure, Spin Polarization, Solid-State Electrochemistry, and High n-Type Carrier Mobility of a Paramagnetic Semiconductor: Vanadyl Tetrakis(thiadiazole) porphyrazine”
Y. Miyoshi, K. Takahashi, T. Fujimoto, H. Yoshikawa, M. M. Matsushita, Y. Ouchi, M. Kepenekian, V. Robert, M. P. Donzello, C. Ercolani, K. Awaga
Inorg. Chem. **2012**, *51*, 456–462.